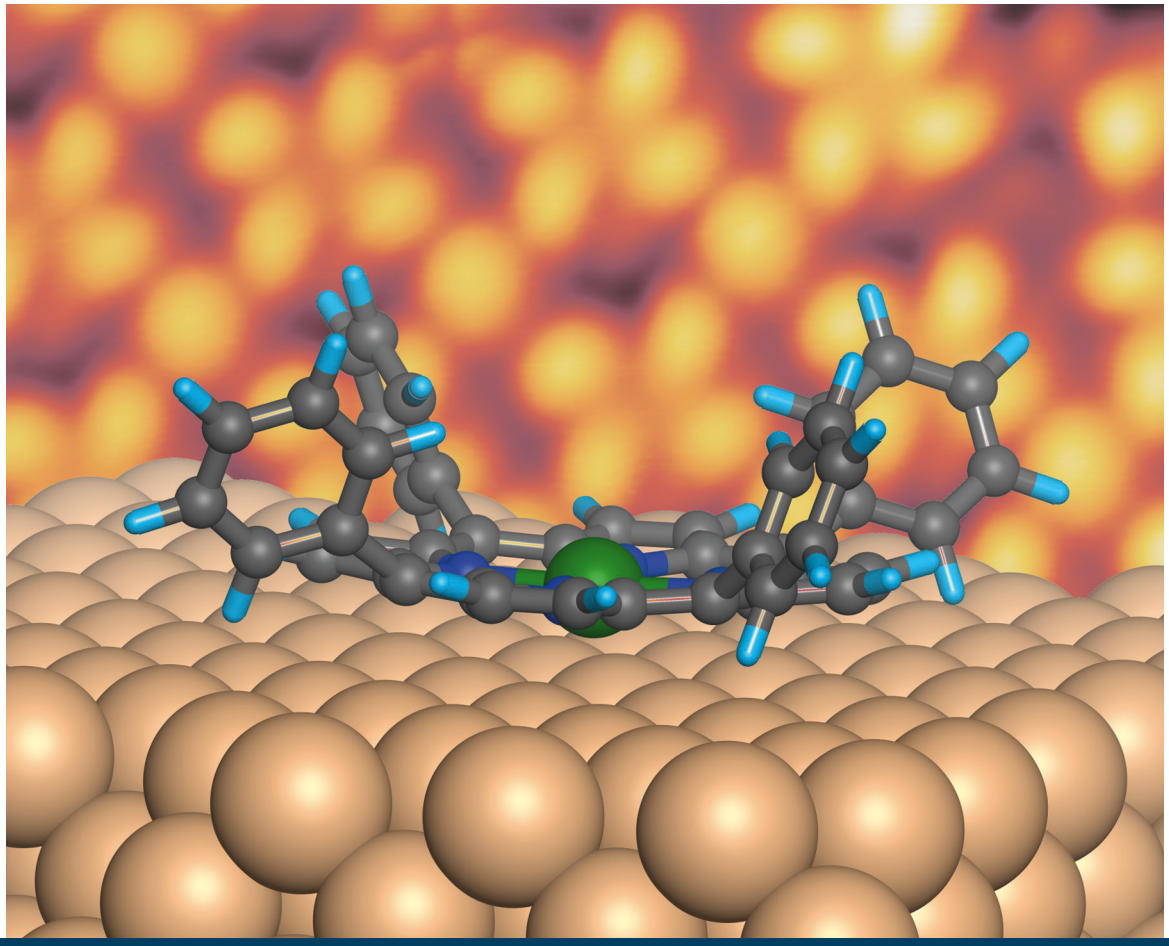

Organic-Metal Hybrid Interfaces at the Mesoscopic Scale

Giovanni Zamborlini

Information
Band / Volume 55
ISBN 978-3-95806-328-0

Mitglied der Helmholtz-Gemeinschaft

JÜLICH
Forschungszentrum

Schriften des Forschungszentrums Jülich
Reihe Information / Information Band / Volume 55

Forschungszentrum Jülich GmbH
Peter Grünberg Institut (PGI)
Elektronische Eigenschaften (PGI-6)

Organic-Metal Hybrid Interfaces at the Mesoscopic Scale

Giovanni Zamborlini

Schriften des Forschungszentrums Jülich
Reihe Information / Information Band / Volume 55

ISSN 1866-1777 ISBN 978-3-95806-328-0

Bibliografische Information der Deutschen Nationalbibliothek.
Die Deutsche Nationalbibliothek verzeichnet diese Publikation in der
Deutschen Nationalbibliografie; detaillierte Bibliografische Daten
sind im Internet über http://dnb.d-nb.de abrufbar.

Herausgeber und Vertrieb:	Forschungszentrum Jülich GmbH Zentralbibliothek, Verlag 52425 Jülich Tel.: +49 2461 61-5368 Fax: +49 2461 61-6103 zb-publikation@fz-juelich.de www.fz-juelich.de/zb
Umschlaggestaltung:	Grafische Medien, Forschungszentrum Jülich GmbH
Druck:	Grafische Medien, Forschungszentrum Jülich GmbH
Copyright:	Forschungszentrum Jülich 2018

Schriften des Forschungszentrums Jülich
Reihe Information / Information, Band / Volume 55

D 464 (Diss., Duisburg, Univ., 2018)

ISSN 1866-1777
ISBN 978-3-95806-328-0

Vollständig frei verfügbar über das Publikationsportal des Forschungszentrums Jülich (JuSER)
unter www.fz-juelich.de/zb/openaccess.

Contents

Zusammenfassung

In organisch basierten Bauelementen spielt die Molekül-Substrat Wechselwirkung eine Schlüsselrolle bei der kontrollierten Ladungsinjektion. Insbesondere der Ladungstransfer an der Molekül-Metall Grenzfläche bestimmt dabei die magnetischen und physikalischen Eigenschaften des Systems, welche letztendlich die Leistung und Effizienz des Bauteils bestimmen.

In der vorliegenden Arbeit werden theoretische und experimentelle Nachweise für eine unerwartet hohe Ladungstransferrate bei der Adsorption von Nickel-Tetraphenylporphyrin (NiTPP) Molekülen auf einer Cu(100) Oberfläche erbracht. Dieser Ladungsaustausch führt zur Auffüllung der unbesetzten Molekülorbitale bis zum LUMO+3. Als Konsequenz dieser starken Wechselwirkung mit dem Substrat kommt es zu einer starken Verzerrung der Adsorptionsgeometrie, welche eine Untersuchung des Makrorings mittels Rastertunnelmikroskopie erschwert und eine zuverlässige Untersuchung der Zustände mit diesem Ansatz unmöglich macht. Hier stellt die Molecular Orbital Tomography eine Alternative dar, da sie Zugriff auf die elektronischen Zustände des NiTPP Makrozykluses ermöglicht und somit die Bestimmung der Umordnung und des Füllzustands der LUMO im adsorbierten Zustand erlaubt. Die Arbeit zeigt, dass die Anpassung der energetischen Niveaus der molekularen Orbitale unter Adsorption nur schwach mit dem Metallatom des Porphyrin korreliert und auch nur in geringem Maß von der Symmetrie des verwendeten Substrats abhängt. Gleichzeitig wird eine schwächere Molekül-Substrat Wechselwirkung beobachtet, wenn CoTPP und NiTPP auf Ag(110) statt auf Cu(100) adsorbiert werden. In diesem Fall kommt es lediglich zu einer Füllung der degenerierten Zustände LUMO und LUMO+1.

Zusätzlich zur Wahl des verwendeten Substrats kann die Molekül-Substrat Wechselwirkung durch gezielte Funktionalisierung der organischen Schicht mittels eines axialen Liganden kontrolliert werden. Wir zeigen in der vorliegenden Arbeit, dass die Bindung zwischen NiTPP und dem Cu(100) Substrat unter Stickoxidatmosphäre signifikant reduziert ist: Während sich der Ladungstranfer zwischen den NiTPP Molekülen und den Kupferatomen der Oberfläche reduziert, kann ein neuer elektronischer Zustand, welcher im Zusammenhang mit dem NO-NiTPP Komplex steht, im Valenzband beobachtet werden. Erstmalig schlagen wir hier einen *cis*-dinitosyl Ligationmechanismus zwischen den NO-Molekülen und der Porphyrinlage vor, welcher zu einer Bildung eines $(NO)_2-$NiTPP Komplexes bereits bei Raumtemperatur führt.

Synopsis

The molecule-substrate interaction plays a key role in controlling charge injection in organic-based devices. Charge transfer at the molecule-metal interface strongly affects the overall physical and magnetic properties of the system, and ultimately the device performance.

This thesis reports theoretical and experimental evidence of an unexpectedly high charge transfer rate to nickel tetraphenyl porphyrin (NiTPP) molecules adsorbed on Cu(100). The exceptional charge transfer leads to the filling of the unoccupied orbitals up to LUMO+3. As a consequence of this strong interaction with the substrate, the resulting adsorption geometry is highly distorted. For this reason, scanning tunneling spectroscopy cannot reliably probe the states related to the macrocycle. Molecular orbital tomography, instead, provides access to the NiTPP macrocycle electronic states and determine the reordering and filling of the LUMO*s* upon adsorption.

The overall energy level alignment of the molecular states, upon adsorption on the metal surface, is shown to be only weakly dependent on the metal ion within the porphyrin, as well as on the symmetry of the crystalline substrate. On the other hand, the molecule-substrate interaction is weaker when CoTPP and NiTPP are deposited on the Ag(110) surface in comparison to Cu substrate, resulting in the filling of only the degenerate LUMO and LUMO+1.

The control over the molecule-substrate interaction can also be achieved by functionalization of the organic layer with a proper axial ligand. We show in this work that exposure of the NiTPP/Cu(100) to nitric oxide weakens this interaction: while the charge transfer rate between the Ni porphyrin and the copper surface is reduced, a new electronic state, related to the NO-NiTPP complex, appear in the valence band. Notably, for the first time, we propose here a *cis*-dinitrosyl ligation mechanism between the NO molecules and the porphyrin layer, leading to the formation of $(NO)_2-$NiTPP complex already at room temperature.

Introduction

Organic-based device performances have been rapidly improving in the last years, making them suitable for large-scale industrial applications, involving photo-voltaic cells [1], light emission systems [2, 3] and building of larger flexible electronics [4]. In parallel, the basic research has intensively focused on the chemical and physical properties of semiconducting π-conjugated organic molecules, because they appear to be promising for organic-based device construction. The strength of these molecules lies in the flexibility to tailor their electronic, optical and magnetic properties at the molecular level. The control and fine tuning can be achieved in several manners: by substituting part of the molecule with a desired moiety [5, 6], functionalization with different ligands [7, 8], or by stacking [9] and/or combining different molecular species [10].

Some organic-based devices, like solar cells, cell phone displays, field effect transistors, *etc.* are already available on the market and, very likely, the number of technological applications will increase in the next years. The organic film-substrate interaction plays a key role in charge injection organic-based devices, ultimately limiting their performance. Chemical reactions, hybridization, charge transfer may take place at the interface. From this perspective, detailed information about the changes in the electronic structure and the adsorption behavior of the organic film at the organic-metal contact becomes crucial to design and prototype new devices [11]. A main obstacle in trying to exploit the full-potential of organic molecules is caused by the difficulty to *a priori* predict, model and measure the electronic and structural properties of the interfaces [12]. In contrast to inorganic semiconductors, where well-established models can be used to easily describe electronic and optical processes [13], no simple picture is available for the excitation and transport processes in organic materials. In these systems, the weak Van-der-Waals interactions along with the absence of an overlap between the wavefunctions of neighboring molecules lead to charge carrier localization and slow inter-molecular transport. As a result, the molecular levels are energetically narrowed and the rigid band model for inorganic complexes cannot be applied. Electrons and holes are now described in term of polarons: in this framework physical and transport properties of these quasi-particles are relatively complex and not well understood.

On this perspective, in order to fully exploit the full potential of the organic compounds, new models and strategies must be developed to provide an adequate description and characterization of the organic-metal system, paying particular attention to the interfaces. More specifically, in the context of surface science, powerful area-averaging spectroscopic techniques, such as ultraviolet

and x-ray photoemission spectroscopy (UPS and XPS) or near-edge x-ray absorption fine structure (NEXAFS) have been employed to obtain information on the adsorption sites [14] and bonding geometries [15], as well as the electronic structure [16] and magnetic properties [17] of adsorbed molecular layers. However, these spectroscopic techniques have difficulties to unambiguously identify, and properly describe, the features related to the molecule-metal interaction. For example, interpretation of UPS spectra, based on the comparison between sub-monolayer and thick molecular films, might be misleading. The observed structures in the photoemission spectra may arise from purely kinematic factors, such as umklapp scattering [18], rather than molecule-metal hybridization. Even the calculated density of states can be inaccurate, because of the inherent approximations of the theoretical frameworks [19]. For this reason, an experimental technique providing direct access to the electronic structure of adsorbed molecules would be desirable to experimentally shed light on the charge redistribution at the molecule-metal interface.

Angle-resolved photoelectron spectroscopy (ARPES) is a well-established method to study the band structure of solids and recently it has been shown that it can also provide an alternative route to obtain information regarding the charge distribution of individual molecular orbitals [20, 21]. Under specific assumptions about the final state of the photoemitted electron, molecular orbital structures can be investigated using data from the angle-resolved photoemission. This approach, based on the comparison between ARPES measurements and theoretical calculations, forms the basis of molecular orbital tomography (MOT). MOT has been proven to be extremely useful also for identifying molecular states of adsorbed molecules on metallic surfaces beyond a simple comparison of energy-distribution curves measured in photoemission experiment with the calculated orbital energies [20, 22, 23, 24].

The aim of this thesis is to apply MOT to π-conjugated molecules deposited on metal substrates in order to unravel the electronic structure of the molecule-metal interface, even in the presence of strong hybridization. Hereby, it is presented a comprehensive characterization of electronic properties and geometric structure of nickel tetraphenyl porphyrin (NiTPP) deposited on the Cu(100) surface. The occupancy and the energetic rearrangement of the frontier molecular orbitals, upon adsorption of the NiTPP on the copper surface, is unequivocally determined by means of MOT. Notably, it also demonstrated that these states, which are spatially located on the NiTPP's macrocycle, cannot be reliably probed by scanning tunneling microscopy, because of the strong molecule-metal interaction. The conclusions drawn from MOT are also supported by experimental data obtained by using other surface science techniques, such as XPS and NEXAFS, combined with density functional theory calculations.

Moreover, while the overall energy level alignment of the molecular states is proven to be only weakly dependent on the metal ion within the porphyrin molecule, as well as on the symmetry of the crystalline substrate, the choice of the metal support influences the occupation of the frontier orbitals. It is also shown that the control over the molecule-substrate interaction can also be tailored by functionalization of the organic layer with a proper axial ligand.

Chapter 1 provides a brief overview of the basic quantities and the physical properties of the organic-metal interfaces and the phenomena, which ultimately affect the energy level alignment of the molecular electronic states.The energy position of the highest occupied and lowest unoccupied molecular orbitals (HOMO and LUMO, respectively) depends on the charge transfer between the molecular layer and the substrate, and the subsequent dipole formation at the interface.

A short review of the porphyrin-metal interfaces, which have been studied in the present thesis, is presented in **chapter 2**. The attention will be mainly focused on the adsorption geometry and electronic structure of porphyrin films deposited on noble metal substrates, such as copper, silver and gold. A few examples regarding the magnetic coupling between porphyrins and different ferromagnetic substrates will be also give. The functionalization of the metal ion in the center of the porphyrin macrocycle by other ligands (NO, NH_3, CO) will be discussed as well.

A description of the experimental techniques used is presented in **chapter 3**. In particular, the first two sections are dedicated to photoemission spectroscopy (PES) and X-ray absorption spectroscopy (XAS). These two techniques can be implemented in a laterally-resolved manner in a photoemission electron microscope (PEEM), which will be described in section 3.3. The molecular orbital tomography (MOT), which is a combination of angle-resolved photoemission spectroscopy (ARPES) and density functional theory calculations (DFT), will be introduced as well. A brief introduction on low energy electron microscopy (LEEM) and scanning tunneling microscopy (STM) will be also given.

Chapter 4 illustrates the experimental details. Information about the sample preparation and characterization are also provided.

In **chapter 5** a consistent picture of the adsorption geometry and electronic properties of the nickel tetraphenyl porphyrin (NiTPP), adsorbed on the Cu(100) surface, will be developed combining different state-of-the-art experimental techniques supported by density functional theory calculations. By means of MOT, the occupancy of the molecular frontier orbitals, *i.e.* HOMO*s* and LUMO*s*, will be unequivocally determined. It will be shown also that the strong molecule-substrate interaction leads to an highly distorted molecular adsorption geometry, which allows to maximize the contact area between the nickel porphyrin and the copper surface, while preventing the frontier orbitals to be probed by STM. Finally, an estimate of the induced damage to the molecular film by electron beam irradiation will presented at the end of the chapter.

In **chapter 6**, the MOT approach will be used to study the molecular energy level alignment of nickel and cobalt tetraphenyl porphyrins deposited on Cu(110) and Ag(110), particularly discussing the influence of the substrate on the electronic structure of the adsorbed molecules.

Finally, in **chapter 7** it will be shown that functionalizing the NiTPP/Cu(100) system with nitric oxide (NO) may lead to an unexpected axial coordination of the NO molecules to the Ni ion at the porphyrin center. The photoemission spectroscopy evidences of the *cis*-dinitrosyl adsorption configuration and the subsequent formation of the $(NO)_2-$NiTPP/Cu(100) complex are further supported by STM and NEXAFS data.

Chapter 1

Molecule-metal interactions

This section aims to briefly overview the basic quantities used to describe the physical properties of organic systems and organic-metal interfaces. We will then focus on the models which have been developed over the years to explain the rearrangement of the electronic structure at the interface between an organic semi-conducting film and a metal substrate. The focus will be in particular on the energy level alignment of the molecular electronic states, *i.e.* molecular orbitals (MO), once the contact has been established.

The "Schottky-Mott" regime, borrowed from the inorganic semi-conductor field, holds in the simplest situation, where the organic film does not interact with the metal substrate. However, many systems cannot be properly described in this framework. For this reason, the mechanism of Fermi level pinning was subsequently introduced. This description of the organic-metal interface, albeit representing an improvement with respect to the Schottky-Mott picture, is still not always able to provide a comprehensive and satisfactory picture of the energy level alignment.

1.1 Basic properties of organic-metal interfaces

π-conjugated molecules (or polymers), employed in the fabrication of organic based devices, are mainly composed of carbon atoms in addition to other "light" atomic species, such as nitrogen, hydrogen and oxygen. In these compounds single and double carbon bonds alternate in a recurrent scheme, called conjugation. The sp^2 hybridized carbon atoms form three covalent sigma bonds within the molecular plane, the overlap of remaining p_z orbitals results in the formation of the π-bonds. The highest occupied molecular orbital (HOMO) and the lowest unoccupied molecular orbital (LUMO) are generally delocalized over the occupied π-bonding and unoccupied π^*-antibonding states, respectively. Usually σ-bonds are stronger than π-bonds, so molecules do not break apart when the π^* or π states are populated or depopulated, respectively. These phenomena, for example, are observed in optical excitations or during charge carrier injection [25].

In a poly-atomic molecule, the effective potential felt by one electron is given by the atomic nuclei and the other electrons. The inner energy shells, having their electrons strongly bounded

and localized onto the nuclei, maintain an atomic orbital character. In the upper part of the potential, instead, the potential wells are merged, forming a broad well. In this region the atomic orbitals interact forming the delocalized molecular orbitals (MO). The outermost flat part of this broad well represents the vacuum level (VL). The energy separation between HOMO (LUMO) and VL is called the ionization energy (IE) (electron affinity (EA)). IE/EA values for an organic solid are lower/higher with respect to those of the isolated molecule in the gas-phase. The Fermi level E_F is placed in the middle of the gap between HOMO and LUMO. A simplified scheme of the potential well is sketched in figure 1.1. IE can be measured by photoemission electron spectroscopy (PES), while EA is usually determined indirectly from IE and the HOMO-LUMO gap, the latter is deduced from optical measurements [26].

Regarding the overall molecule-metal interface, we need first to distinguish between the vacuum level at infinite distance VL(∞) and close to the surface VL(s). The first is taken as an invariant energy reference, the second is affected by the surface potential [27]. Thus, the most relevant quantities introduced previously (EA, IE and WKF) are referred to VL(s). A well-know example is the dependence of WFK on different crystal surface orientations. This is well illustrated for the (100), (110) and (111) tungsten surfaces, which have the same E_F but different values of WKF. This is because the work function is mostly related to the surface dipole resulting by the tailing of the electron cloud at the surface, producing a different value for each considered crystallographic orientation. In short, VL(∞) $\neq$ VL(s). When molecules and the metal surface are at an infinite distance, $VL^{METAL} = VL^{MOL} = VL(\infty)$ (see figure 1.2a). When they are in direct contact, instead, *i.e.* after deposition/adsorption (Figure 1.2b), they are sharing a common VL(s).

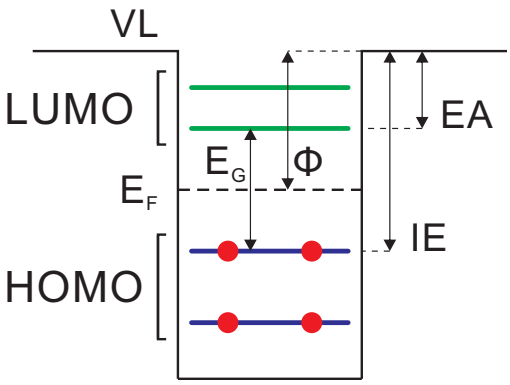

Figure 1.1: Simplified sketch of the electronic structure of an isolated molecule. Red dots represent electrons filling HOMO levels (blue lines). E_F (dashed line) is in the middle of the gap (E_G) between HOMO and LUMO (green line). IE and EA are also indicated in the scheme.

Depending on the molecule-substrate interaction, charge transfer, chemical reactions or redistribution of the electronic density may occur at the interface. A significant amount of charge may be transferred or withdrawn to/from the molecular layer, populating/depopulating frontier molecular orbitals, *i.e.* the orbitals closer to the gap between occupied and unoccupied states (LUMOs and HOMOs). Their energy positions, as well as the final adsorption geometry of the molecule may be drastically affected by this charge rearrangement [28]. Furthermore, this redistribution of the electronic cloud leads to the formation of an extra dipole. This dipole produces a shift of the potential (Δ) at the interface proportional to its strength, changing the measured work function of the overall system [26].

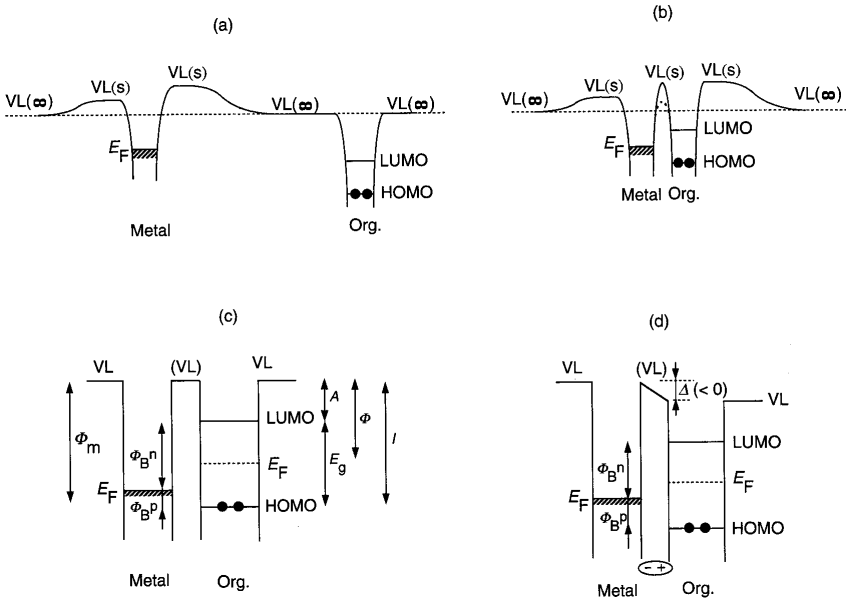

Figure 1.2: a) Electronic structure of a metal and a molecule at infinite distance. b) Electronic structure of a molecule-metal contact. The organic layer is within the electric field of the surface dipole layer of the metal, they share the common VL. c) Schematic representation of (a) assuming common VL(s) at the interface. Φ_B^n and Φ_B^p are the injection barriers for electrons and holes respectively. d) Schematic representation of (b). Reproduced from [26].

1.2 What determines the orbital binding energies?

Only knowing the values of IE, EA and WKF of the material, we can pose the question whether it is possible to predict how the electronic structure of an organic molecule will change upon adsorption on a metal surface. In the simplest case, there is no interaction between the molecular film and the metal substrate underneath. The extra dipole introduced previously (Δ) vanishes, therefore $VL_{MOL}(s)$ aligns to $VL_{METAL}(s)$ (see fig. 1.3). This is called Schottky-Mott regime or *Vacuum Level Pinning*. Under these circumstances we derive a simple analytic expression for LUMO ($E_B^{\mathbf{LUMO}}$) and HOMO ($E_B^{\mathbf{HOMO}}$) binding energies:

$$E_B^{\mathbf{LUMO}} = \Phi_M^0 - EA \qquad E_B^{\mathbf{HOMO}} = IE - \Phi_M^0 \tag{1.1}$$

where Φ_M^0 is the metal work function. This approximation is justified only when the molecule-metal interaction is rather weak and no surface induced dipole is formed at the interface. The equation 1.1 predicts a linear dependence between orbital binding energies and Φ_M^0.

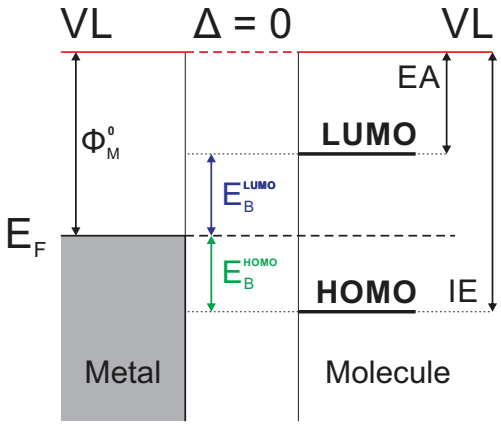

Figure 1.3: Simplified sketch, in the Schottky-Mott regime, of the electronic structure of an organic/metal interface. In this case $\Delta = 0$, so the organic VL aligns with the VL of the metal. E_B^{HOMO} and E_B^{LUMO} are the binding energies of HOMO and LUMO referred to the metal E_F.

There are several experiments on H_2TPP [29] or PTCDA [30], adsorbed on metal substrates, which cannot be described within the vacuum level pinning framework. In particular, often the overall energy level alignment results from competing phenomena. One of these is the *pillow effect* (or *push-back effect*): due to the Pauli repulsion, the adsorbed organic film pushes-back the tail of the metal electronic cloud, which spills out from the surface in the absence of the organic film. The effect on the electron cloud leads to the formation of an interface dipole which lowers the WKF [31]. In addition, the molecular adsorption can be accompanied by charge transfer from the substrate to the organic layer. These two competing phenomena ultimately determine the energy level alignment of the organic film.

In order to include the charge transfer and the pillow effect in the description of the organic-metal interface, we must introduce two new concepts: the induced density of interface states (IDIS) and the molecular charge neutrality level (CNL) [28]. In the proximity of the metal surface the discrete molecular levels are broadened into the continuum IDIS because of the molecule-substrate interaction, *e.g.* hybridization or chemical bonding. The CNL is determined by integrating the IDIS and imposing that the total number of electrons up to the CNL must be equal to the number of electrons in the neutral molecule [28]. In other words: if the CNL is aligned precisely with the metal E_F, the total charge in the IDIS is zero; whereas it is positive or negative if the CNL is below or above E_F, respectively.

In this model the energy level alignment is driven by the adjustment of the chemical potential across the organic-metal interface. When the neutral molecule approaches the surface, the push-back induces the formation of a potential step between $VL_{MOL}(s)$ and $VL_{METAL}(s)$, misaligning E_F and CNL. This imbalance produces a charge flow, which stops when the chemical potential is realigned. The charge flowing tries to move the CNL close to E_F. How far the CNL can move depends on how large is the IDIS, *i.e.* on the amount of charge that the molecular layer can accept

or donate. In this case we are in the so called *Fermi level pinning* regime (sketched in Figure 1.4, the molecular energy levels are pinned to E_F and totally independent from Φ_M^0.

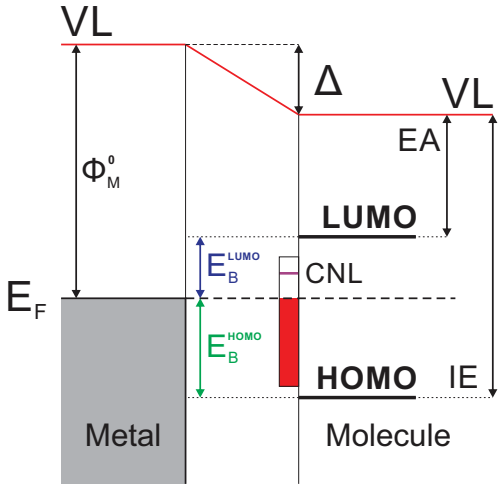

Figure 1.4: Simplified sketch of the electronic structure of a typical organic–metal interface, showing the relevant energy levels on both sides. All the quantities are described extensively in the main text.

In reality, most of the systems can be found somewhere in between the Fermi and vacuum level pinning [32]. In this respect, the system can be described by the screening, or slope parameter (S):

$$S = \frac{dE_B^{M.O.}}{d\Phi_M} \tag{1.2}$$

where $dE_B^{M.O.}$ is the binding energy of either HOMO or LUMO. The vacuum level pinning corresponds to $|S| = 1$, *i.e.* the specific energy level follows the metal WKF. When the pinning is at the Fermi level instead, $|S| = 0$.

Chapter 2

Porphyrin molecules

2.1 Introduction

2.1.1 Structure

The common ancestor of all porphyrins is porphin ($C_{20}H_{14}N_4$), shown in figure 2.1, a planar hetero-macrocycle with D_{2h} symmetry. It is composed of four pyrrole moieties linked by methin groups (=CH−) at their α position [33]. According to Hünkel's aromaticity rule, the porphin conjugated π-system has 18 electrons ($4n + 2$, $n = 4$) along the shortest cycling path. Two of the peripheral double bonds, located at the opposite pyrrolic rings, are cross-conjugated and thus they are not necessary for aromaticity. Reduction of one, or both of these cross-conjugated double bonds, still preserves the aromaticity.

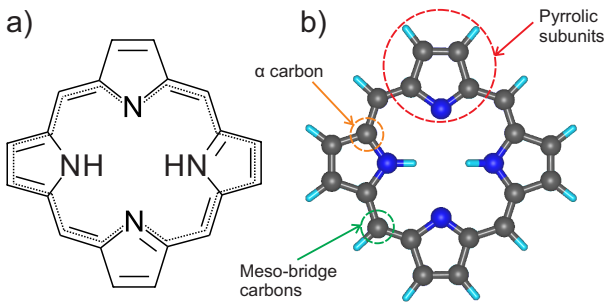

Figure 2.1: Porphin (H_2P), the parent macrocycle of porphyrins. (a) Chemical structure. (b) Ball-and-stick model.

Free-base porphyrins (from greek *porphura* = purple) are a porphins with peripheral substituents (fig. 2.2a). In particular, the porphyrins used in the present thesis belong to the family of the *meso*-tetraphenyl porphyrins (fig. 2.2b), in the following called also H_2TPP or simply TPP. These molecules have four phenyl substituents bonded to the methin bridges at the *meso*-position. H_2TPP has a non-planar geometry because of the sterical repulsion between the hydrogen atoms

of the substituents and the porphin core. This repulsion leads to a rotation of the phenyl groups along the C−C bond connecting them to the *meso*-bridge (see fig. 2.1b), followed by a bending of the TPP macrocycle, which deforms in a saddle-shape [34]. There are also other porphyrin classes like the octaalkalyporphyrins, for example, very common in biological systems. In this case the substituents are attached at the pyrrole in β-position, *e.g.* octaethylporphyrin or etioporphyrin.

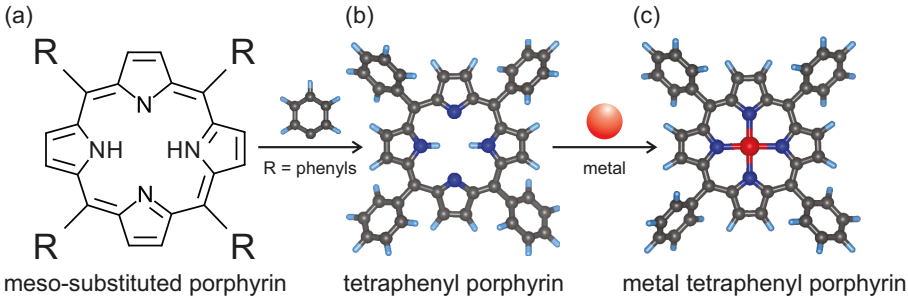

Figure 2.2: (a) Chemical structure of a *meso*-substituted porphyrin. (b) *Meso*-tetraphenyl porphyrin H_2TPP. At the *meso* position four phenyl group are attached to the H_2P macrocycle. (c) Metal tetraphenyl porphyrin MTPP. The two hydrogens, attached to the nitrogens, leave the macrocycle, allowing a metal ion to be incorporated in the middle. Depending on the ionic radius, the metal can lie outside or within the macrocycle plane.

Porphyrins form complexes with almost all elements in the periodic table with stable isotopes, except for nitrogen, rare gases and halogens. The macrocycle size, *i.e.* the space between the coordinating nitrogen atoms, match perfectly with the 3*d* metal ion radii and indeed a high number of metals (*e.g.* Fe, Zn, Cu, Ni, and Co) can be accommodated in the center of the macrocycle (see fig. 2.2c), forming metalloporphyrins (MTPP). Sn, Pb or Ce, instead, because of their larger size, lie outside the porphyrin plane [35]. Usually the metal ion, incorporated at the porphyrin center, is in a formal +2 oxidation state unless additional ligands are bound in the axial position. Free-base porphyrins, deposited on metal surfaces, may pick up substrate adatoms, incorporating them into the macrocycle. This process is called "metalation" and it can occur already at room temperature [36], or by thermally annealing the deposited molecule [37]. Metalloporphyrins are thus often synthesized by metalation of free-base porphyrin with the desired metal ion.

The porphyrin square-planar configuration favors the binding of additional ligands in the free axial sites. When the metal ion lies on the macrocycle plane, ligands usually assume a *trans*-position relative to each other, *i.e.* they are attached to the metal center at the opposite sides of the molecule. In this configuration, they compete for the stronger bond to the metal ion. This phenomenon can be exploited for fine tuning of electronic and magnetic properties in metalloporphyrins-metal interfaces. In particular, functionalization with specific ligands, such as NO or NH_3, may modify the overall metalloporphyrins spin state allowing one to control the magnetic coupling between the organic film and the supporting ferromagnetic substrate [38, 8]. With larger metal ions, being placed above the macrocycle plane, the *trans* ligand can be also another porphyrin molecule, leading to the formation of a double-decker complex.

2.1.2 Importance and applications

Metalloporphyrins can be found in many fundamental processes in life: from photosynthesis to transport of respiratory gases. Chlorophyll, which provides the necessary energy amount to produce glucose from CO_2 and H_2O, is a magnesium porphyrinoid-based biomolecule. The hemoproteins are involved in many biological processes, including catalysis, electron transfer and oxygen transport (hemoglobin): the active centers of such molecules are Fe(II) porphyrin complexes.

In the past decade, the attention on porphyrins has been renewed because of possible applications in several fields:

- **Catalysis**
  - **Fuel cells** Porphyrins can act as a catalyst in the fuel cell to improve the oxidation reaction. The efficiency is comparable to the one obtained using more expensive catalyst like platinum [39].
  - **Heterogenous catalysis** The use of cobalt tetraphenyl porphyrin CoTPP supported on TiO_2 could have important environmental applications as a catalyzer in the NO reduction with CO and H_2 [40].
- **Gas sensors** The availability of an axial coordination site on the metal center favors the porphyrin interaction with many types of gases. The analyte, adsorbed into a thick porphyrin film, produces changes in several measurable physical quantities (WKF, mass and optical adsorption). Contacting the porphyrin layer with a suitable transducer, these variations are then transformed into an electrical signal, allowing the construction of gas sensors [41].
- **Solar cells** The strong absorption coefficient in the near-IR and visible ranges, where the solar photon flux is maximum, makes porphyrins perfectly suited to be integrated in light/energy conversion process inside photovoltaics devices [42].

2.2 Porphyrins on metals: surface interactions

A comprehensive understanding of the nature and strength of porphyrin-substrate interactions is mandatory in the interface engineering for organic-based devices. Especially, the changes in the molecular conformation, charge transfer and spin state, in case of reactive surfaces, are crucial in predicting the device performances. To unravel the structural and electronic properties of such interfaces, a comprehensive analysis, involving state of the art experimental techniques and advanced theoretical calculations, is often needed. In the following we will briefly review the most important aspects in the porphyrins-substrate interaction focusing on the adsorption geometry, changes in the electronic structure, magnetic coupling with ferromagnetic surfaces and metal center functionalization. The reported examples will cover mainly porphyrins and porphins on noble metal single crystal surfaces or ferromagnetic substrates.

2.2.1 Adsorption geometry

The wide range of applications of porphyrins is based on their mutability as they can adapt their structural conformation to the local environment, deforming the macrocycle and/or reorienting the substituents. The final adsorption results from the competition between molecule/surface interactions and the molecule-molecule repulsion/attraction, as it can be directly observed in free-base porphin (H_2P) deposited on Ag(111) system [14]. In small concentration, H_2P*s* repel each other, preventing the formation of compact islands. Increasing the coverage, the inter-molecular distance decreases continuously, while multiple phase transformations occur: the system evolves from an isotropic gas-like configuration to a crystalline structure that, approaching the maximum coverage possible without forming a second layer, becomes disordered. The evolution of the system can be followed in figure 2.3. Density functional theory (DFT) calculations show how the substrate molecule-interaction favors an exclusive adsorption on bridge positions of Ag(111). The adsorption site along with the repulsive character of the molecule-molecule interaction, ultimately lead to this specific assembly mechanism [14].

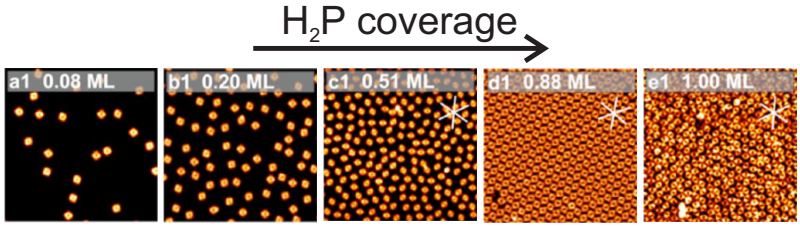

Figure 2.3: STM images taken at different H_2P coverages on Ag(111): (a1) 0.08ML, (b1) 0.20ML, (c1) 0.51 ML, (d1) 0.88 ML, (e1) 1 ML. Single molecules appear as bright square-like dots in the STM images. Porphin assemblies undergo three phase transformations from a lattice gas to a liquid-like phase (b→c), from a liquid-like phase to a regular 2D lattice (c→d), and finally from a regular lattice to a disordered layer (d→e). Reproduced from [14].

By attaching four phenyl substituents to the porphin, we introduce extra degrees of complexity, increasing the total number of possible molecular configurations. Beside the saddling motion of the macrocycle, the phenyl ligands can now twist or/and tilt. Following the notation of Wolfle *et al.* [43], these movements can be quantified by two angles: ϕ and θ. The tilt is described by ϕ, namely the angle between the plane of the macrocycle and the single C-C bond connecting the substituent to the *meso*-carbon bridge. θ, instead, is the twist angle, *i.e.* the azimuthal rotation of the substituent around the same C-C bond. At a twist angle of $\theta = 90°$ the phenyl groups are perpendicular to the plane defined by the porphyrin core. Both angles are indicated in figure 2.4. Tetraphenyl porphyrins are quite flexible because the macrocycle can be distorted in a saddle configuration, while θ may vary between 90° and very "small" angles, even less than 30° [34].

When porphyrins are adsorbed on metal substrates, because of attractive van-der-Waals interactions, they would like to maximize the molecule-surface contact area, becoming planar. This mechanism is balanced by the strain generated from the unfavorable co-planarity between

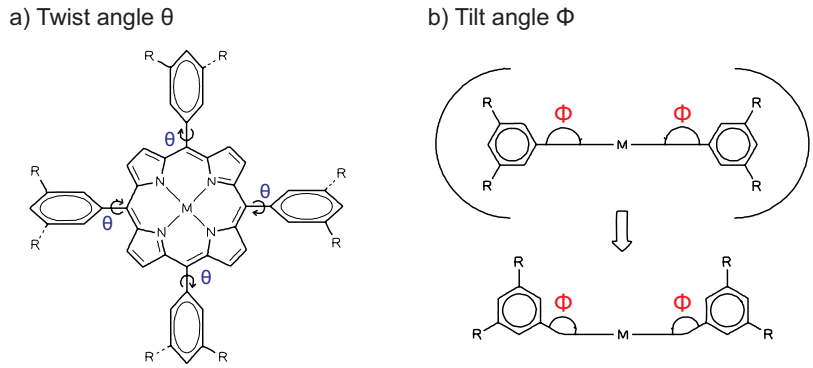

Figure 2.4: Sketch of the possible substituent rotations. (a) θ is the twist (dihedral) angle, *i.e.* the angle between the substituent plane and the surface plane around the same bond. (b) ϕ is the angle between the plane of the macrocycle and the single C-C bond connecting the substituent to the core. Reproduced from [43].

the phenyl rings and the porphyrin core. As a response to the strain, the macrocycle assumes a saddle-shape. This configuration reduces the phenyl ring rotational barrier, making possible to reach smaller θ [44]. The energy cost associated with the saddling is partly compensated by the increased π-conjunction due to the entire molecule being in a more, on average, co-planar configuration [34].

Several experimental techniques are available for the structural characterization of molecule-metal systems. Geometrical deformations, which occur upon adsorption, can be studied in a quantitative manner by means of near edge x-ray absorption fine structure (NEXAFS). NEXAFS is able to distinguish between the contribution of the macrocycle and substituents as there are distinct features in the absorption spectrum corresponding to each unit. Angular-dependent NEXAFS measurements determine the orientation of the phenyl rings and quantify the saddle shape deformation of the macrocycle. Moreover, the determination of the unit cell of an ordered porphyrin film can be done by combining together low energy electron diffraction (LEED) and scanning tunneling microscopy (STM). Based on results from DFT calculations, including simulation of STM images, the structural properties of the adsorbed molecule can be rationalized.

Changing the metal substrate may result in a drastic change of the physical properties of the adsorbed porphyrin molecules. While they strongly bind to the copper surface, the overall molecule-metal interaction results weakened if porphyrins are deposited on silver or gold. In the following, we will shortly discuss some examples regarding the adsorption geometry of MTPP molecules deposited on noble metals (copper, silver and gold, in this order), also considering the effects due to metal ions at the porphyrin core.

On copper, the presence or absence of the ion metal at the macrocycle center strongly influences the porphyrin self-assembly. On Cu(111) for example, while the H_2TPP adsorption is very site-specific [45] and no ordering is observed until the surface is almost saturated [46], CoTPP forms a long range ordered square lattice, incommensurate with the substrate. The site-specificity of

the H_2TPP assembly is attributed to the strong interaction between the iminic nitrogens (-NH-) of the macrocycle [45]. In this case, the origin of the intermolecular forces driving the assembly must be ascribed to the periphery of adjacent molecules. As sketched in figure 2.5a, when the phenyl rings of neighboring molecules are oriented in the so-called "T-type" manner, *i.e.* with the H atom of one ring points toward the center of the adjacent ring, the molecular assembly is stabilized [45]. Both CoTPP*s* and H_2TPP saddle upon adsorption, allowing phenyl rings to reach smaller θ angles of 35° [47] and 10°, respectively. The former value is still sufficient to establish a T-type interaction between the phenyl rings, the latter instead does not allow this mechanism. The saddling, responsible for these small θ, has its origin in the strong substrate-molecule interaction: one pair of pyrrole rings tilts upwards, while the other pair bends down, with an estimate bending of $\pm 20°$ [47] (see figure 2.6a).

Relatively strong deformation results also for CoTPP deposited onto Cu(110). The reduced surface symmetry produces only two ordered CoTPP mirrored domains rotated $\pm 20°$ with respect to the [001] direction. These domains are commensurate to the substrate with the molecules adsorbed on the short bridge site. CoTPP, closely packed, form a structure with a propeller-like chiral conformation. In this geometry, the macrocycle plane sits only 2.1 Å above the copper surface. Phenyl rings are forced to tilt upwards ($\phi = 144°$), maintaining a θ value of almost 80° [48] (see figure 2.6b).

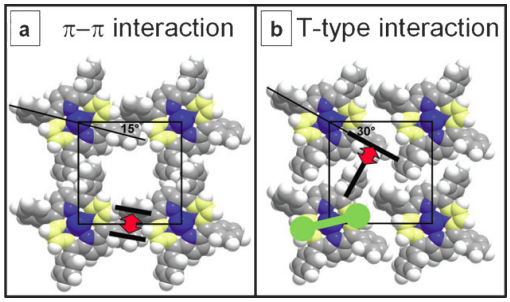

Figure 2.5: Space-filling models of two possible arrangements of TPP on Ag(111). (a) $\pi - \pi$ stacking: adjacent phenyl legs are aligned in parallel. (b) T-stacking, resulting in a perpendicular motif of neighbouring phenyl rings. Reproduced from [49].

CoTPP (see figure 2.6c) deposited on Ag(111), grows along the substrate high symmetry directions, forming three different rotational domains (rotated by 120° respect to each other). Even if the growth direction is registered to Ag(111), the molecule-substrate bond is not strong enough to form commensurate domains [50]. Therefore, the close-packed self-assembly must rather rely on intermolecular interactions. CoTPPs start packing together already at low coverages, forming a lattice with a square unit cell, which reflects the molecular symmetry. These intermolecular forces originate from the molecule periphery. In this case, another type of attractive interaction between phenyl rings of adjacent TPPs, which appears to be likely, is the so-called $\pi - \pi$ stacking (see figure 2.5b). By comparing the resulting DFT relaxed structures with high resolution STM images,

this mechanism is indeed excluded. The phenyl rings of neighboring molecules are oriented in a T-type manner [49]. On Ag(110), H_2TPPs organize in two equivalent domains, mirrored respect to [001] direction and rotated by 59° from each other. The two lattices form simply commensurate superstructures [51]. In atomic resolution STM images, CoTPP, FeTPP and H_2TPP appear only two-fold symmetric, indicating an adsorption-induced deformation. The resulting macrocycle saddle-shape is similar to the one observed in the CoTPP/Cu(111) case: here the pyrrole pair tilt is slightly more pronounced (±30°), and for CoTPP the Co−Ag distance becomes 2.5-3.0 Å [52].

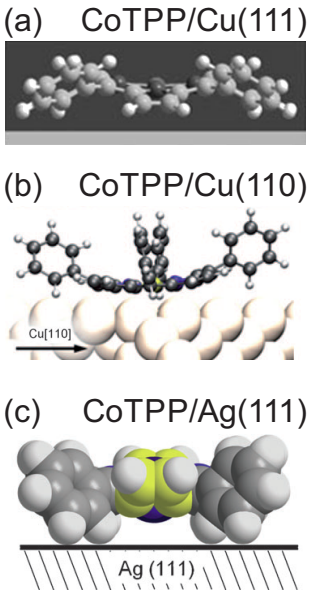

Figure 2.6: Adsorption structure of CoTPP on different substrates. (a) CoTPP/Cu(111). Reproduced from [47]. (b) CoTPP/Cu(110). Reproduced from [48]. (c) CoTPP/Ag(111). Reproduced from [49].

The MTTP adsorption behaviour does not drastically change on the gold surface. CoTPP and NiTPP form well-ordered and densely packed islands, but the resulting lattice is not commensurate with the substrate. Even a mixture of the two gives the same results, with a random distribution of molecular species, pointing out that the metal center plays only a minor role on the final structure [53]. The majority of the molecules remains undistorted upon adsorption. Only a small fraction, in the densely packed monolayer, shows the two-fold symmetry characteristic of the saddle deformation. The interaction with the substrate is too weak to compensate the saddling [54].

In conclusion, the conformation of prototypical MTPP (M = Fe, Co, Ni) slightly differs on different close-packed fcc(111) surfaces. The saddle-shape deformation is more accentuated on silver and copper than on gold, where the molecule-substrate interaction is weaker. On more "open" surfaces, like Cu(110), a stronger substrate interaction leads to a commensurate molecular

lattice. Moreover, the resulting adsorption structure is strongly deformed: phenyl rings tilt upwards, allowing the macrocycle to get very close to the surface.

2.2.2 Electronic structure

Extensive investigations on the electronic structure of adsorbed porphyrins, and their chemical bonding to metal substrates, have been carried out in the last years, motivated by the prospective of using these organic complexes in organic-based electronic devices. Some examples were also mentioned at the beginning of this chapter. A quantitative description of the chemical and physical properties is fundamental for improving the charge injection rate at the metal-organic contact.

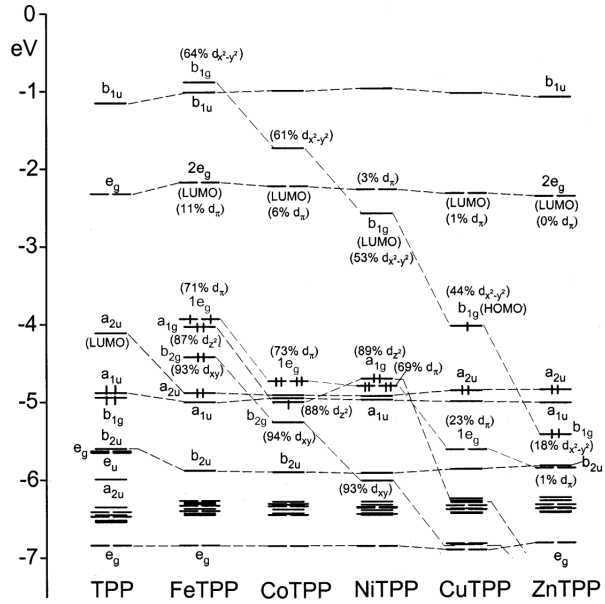

Figure 2.7: Orbital energy levels of single MTPP molecules. Metal 3*d* contributions of some MOs are listed in parentheses. Electron occupancies are indicated for frontier MOs. Reproduced from [55].

As shown in section 2.2.1, the almost planar adsorption of the porphyrin macrocycle promotes the formation of a direct covalent or coordinative bond between the metal ion and the metal surface [52]. Strong molecule-substrate interactions often lead to electron charge transfer from the metal to the molecule and to highly distorted adsorption geometries [48, 56]. Theoretical treatment of such interactions, within the DFT framework, is hampered by the large contribution of vdW dispersive interactions, which are not adequately described in the standard DFT approach. However, various corrections have been introduced and successfully employed in the numerical calculations, to overcome this issue [46, 56].

Many early studies classified the metal-tetraphenyl porphyrins under the D_{4h} point group,

with all the peripheral substituents parallel or perpendicular to the macrocycle plane. However, it should be noted that, very often, such highly symmetrical configuration does not correspond to the minimum energy for these systems. The macrocycle saddling and the phenyl ring twisting determine the final symmetry of the adsorbed molecule: the pyrrole saddling only, breaks down the symmetry to D_{2d}, the phenyl twisting, instead, results in a S_4 point group [52]. This has severe consequences for the electronic structure, as symmetry lowering lifts degeneracies in the electronic states. In MTPP, the symmetry reduction splits the *d*-orbitals in two degenerate and three non degenerate energy levels. The energy level alignment of the most common metal tetraphenyl porphyrins was systematically studied in ref [55], and the corresponding results are shown in figure 2.7. d_{xy} and $d_{x^2-y^2}$ are confined in the molecular plane, while d_{xz}, d_{yz} and d_{z^2} are projected out ($d_\perp$). Transition metal ions, with the partially or totally unoccupied $d_\perp$ component, have the tendency to form stronger covalent bonds with the metal substrates, *e.g.* Fe(II), Mg(II) and Co(II) [57].

UV photoelectron spectroscopy (UPS), scanning tunneling spectroscopy (STS), STM and NEXAFS are commonly employed to characterize the electronic structure of the adsorbed metallo-porphyrins. UPS valence band spectra can map the density of states (DOS) of the sample surface through the acquisition of energy distribution curves (EDC). The DOS of the molecule-metal system is determined by following changes in the EDC as a function of the molecular coverage, from sub-monolayer up to thick molecular films [58, 59]. The latter, where the signal due to the molecule-substrate interface is negligible, is commonly adopted as a good approximation for the intrinsic molecular DOS, due to the weak intermolecular interactions. In this way, the contribution of the molecular states in direct contact with the substrate can be recognized and separated. This approach sometimes may be problematic because the observed structures in the photoemission spectra may arise from other factors, such as umklapp scattering [18], rather than molecule-metal hybridization. In umklapp scattering, the photoemitted electron is rescattered from the molecular overlayer, thus, changing its emission direction. As a consequence an electron, which would be emitted off normal from the clean substrate, under these conditions can be found at normal emission (NE) in the ML spectrum. For this reason, some of the features, arising in the EDC*s* upon adsorption of large π-conjugated organic molecules, are reminiscent of the metal 3D-integrated DOS. At the monolayer coverage such features dominate the EDC curve, and might be misleading when assigning these features to molecule-substrate interface states [18].

Alternatively, the assignment of the observed spectral features in the valence band can be based on theoretical calculations of the DOS. However, the inherent approximations in the theoretical frameworks may lead to ambiguities, or inaccurate or wrong interpretation of experimental data. In DFT calculations, for example, standard general gradient approximation (GGA) functionals may result in an incorrect orbital ordering due to problems dealing with the self-interaction error [55, 19]. This problem is amplified when different orbitals have significantly different spatial character, *e.g.* localized *vs.* delocalized. In such cases, the occupied Kohn-Sham eigenvalue spectrum no longer reflects a physical electron binding scheme [19]. It is crucial to account for all

possible factors that might affect the interpretation of molecular features when the adsorption behaviour of organic films on metal substrate is studied in a systematic way.

STM provides another way to map the charge distribution over the molecule. If the molecular features can be resolved, STM is able to map both occupied and unoccupied molecular orbitals by tuning the bias voltage applied. The resulting images can be compared to DFT simulations, allowing the orbital identification [47]. In principle, this approach can be used to distinguish H_2TPP from MTPP, because the latter usually shows a protrusion at the porphyrin center, commonly associated to the d_z orbital of the metal ion. However, if the d_z orbital is fully occupied, *e.g.* as it happens for CuTPP, the protrusion becomes a dark hole, as in the case of H_2TPP.

In the following, we will present some examples of porphins, porphyrins and metalloporphyrins adsorbed on noble metals: copper, silver and gold, ordered by their reactivity, as we did in the section dedicated to the adsorption geometry.

The simplest case is the porphin. Since H_2P does not have any ligant group attached it is able to maximize the contact area with the substrate, usually leading to a strong molecule-substrate interaction. H_2P forms chemisorbed bonds with Cu(110) surface followed by a massive charge transfer from the substrate to the molecule resulting in the occupation of the gas-phase LUMO. This charge transfer is accompanied by a back-donation from π molecular orbitals to the substrate. The net charge transferred into H_2P can be estimated to 0.9 e^- [56]. Similarly, 1.3 e^- are transferred from the Cu(110) surface to the CoTPP molecule. The consequences of this strong interaction are reflected in a highly distorted adsorption geometry (see section 2.2.1): in order to maximize the molecule-substrate contact area, phenyl rings tilt upwards, allowing the CoTPP macrocycle to move close to the surface [48]. Similarly, also H_2P deposited on Cu(111), which is considered a "closed" surface, has the LUMO partially occupied. In this case, the induced metalation of the porphin by thermal annealing leaves the electronic structure unchanged [60]. The same mechanism does not hold for H_2TPP: upon metalation, the so-formed CuTPP has the LUMO unoccupied, but the reason for this change in the interaction strength is still unclear [37].

Going from Cu to Ag the molecule-metal interaction gets weaker: porphins adsorbed on Ag(111) show only a partial filling ($\sim$10%) of the LUMO [14]. Similarly to porphin, ZnTPP and H_2TPP do not interact strongly with Ag(111). Both porphyrins do not show any feature in the experimental DOS close to E_F, while CoTPP and FeTPP present a new state, which is attributed to the Co(Fe)-Ag interaction *via d* metal orbitals [52]. The reason of a so different interaction strength possibly lies in the larger H_2TPP(ZnTPP)-Ag distance than FeTPP(CoTPP)-Ag, resulting in a smaller overlap between the molecular and metal states [46, 52]. These differences are reflected also in the net charge transferred from the substrate to the molecule: while CoTPP and FeTPP gain 0.37 e^- and 0.22 e^-, respectively, the electron charge transferred to H_2TPP and ZnTPP is negligible [52].

Even though the porphyrin adsorption geometry remains almost unaffected upon deposition on gold surfaces (see section 2.2.1), the molecule-substrate interaction is driven, similarly to silver, by the metal ion at the macrocycle core. CoTPP/Au(111) shows a new state close to E_F, related to

the Co-Au interaction, which is not present in the H_2TPP/Au(111) DOS [47]. However, conversely to Ag, the Co-Au interaction is modulated by the adsorption sites within the Au(111) unit cell [61].

To summarize, the electronic structure of porphins and porphyrins is mediated not only by the different substrate, but also by the presence and/or type of the metal ion inside the macrocycle. The latter strongly influences the substrate-molecule distance, ultimately steering the overlap between the molecular and metal states. Thus, upon adsorption, the a molucular hybrid is form between the porphyrin molecules and the surface atoms.

On copper, molecules sits closer to the surface the formation of strong covalent bonds accompanied by charge transfer to the unoccupied LUMOs, which is followed by a charge back-donation from the HOMOs to the substrate. On Ag, less charge is transferred to the LUMO*s* and the overall interaction results weakened. In this case, the presence of the metal ion open a new interaction channel *via* its *d* orbitals to the Ag substrate, leading to a formation of a new state close to E_F. A similar situation is observed for MTPP*s* on gold.

2.2.3 Magnetic properties

The ability to control and manipulate the electron spin in organic materials offers a new exciting route towards spintronics. Organic molecules, because of their weak spin-orbit and hyperfine interactions, can preserve the spin-coherence over times and distances much longer than in metals or semi-conductors [62]. In this perspective, porphyrins become perfect candidates for spintronic applications. MTPP are paramagnetic molecules but, depending on the metal center, they can possess a nonzero magnetic moment. When placed on a ferromagnetic substrate, the unpaired electrons in the MTPP valence band, often couple to the substrate magnetization forming a molecular spin hybrid [63]. Different mechanisms can be responsible for this magnetic coupling:

- Direct exchange coupling between MOs and the ferromagnetic substrate (FM).
- Indirect superexchange coupling mediated by other atomic species, which binds the MOs to the substrate states.

The magnetic properties of the molecular layer can be tuned, for example, by adding an extra ligand to the adsorbed metal porphyrin. The organic film can be decoupled from the substrate, or the interaction can be weakened due to the surface *trans*-effect [52], and consequently an axial ligand carrying a non-zero spin moment may partly (or totally) compensate for the spin at the metal center [64]. Therefore, this type of functionalization can induce a transition between the low-spin and high-spin states.

The porphyrin-substrate magnetic coupling is often measured by means of X-ray magnetic circular dichroism (XMCD). DFT, instead, provides a theoretical background for the understanding of the underlying coupling mechanism [65]. STM can also probe the magnetic moment of a single molecule: a Kondo resonance at zero bias voltage, in the dI/dV STS curves, is the signature of a nonzero molecular spin moment [66].

The hybridization of MTPP with a nonmagnetic substrate may result in a complete quenching of its spin moment [67]. Instead, when metalloporphyrins are deposited on a ferromagnet, their magnetic moment may align ferromagnetically or antiferromagnetically with the one of the substrate. For example, MTPP*s* having a metal ion with an open shell (M = Co, Mn, Fe), if adsorbed directly on nickel or cobalt, couple ferromagnetically with the substrate underneath. The metal-substrate distance, ranging usually from 3.3-3.6 Å, prevents the overlap of the ferromagnet and the TPP metal center electronic states. The indirect exchange coupling is indeed mediated through the nitrogen atoms [65, 17, 68] (see figure 2.8a).

On the other hand, intercalation of an oxygen layer between the Fe-porphyrins and Co(100) switches the magnetic coupling to anti-ferromagnetic. DFT+U calculations demonstrate that the antiparallel spin alignment is mediated *via* Fe-O-Co indirect superexchange [69]. Also decoupling CoOEP from Ni(111) through a graphene layer results in an anti ferromagnetic coupling between the Co metal center and the substrate (see figure 2.8b). In this case, *ab-initio* calculations reveal an indirect-direct double exchange mechanism between Ni and Co spins through the graphene layer and the overall magnetic coupling is weaker compared to metalloporphyrins directly in contact with the FM substrate [70].

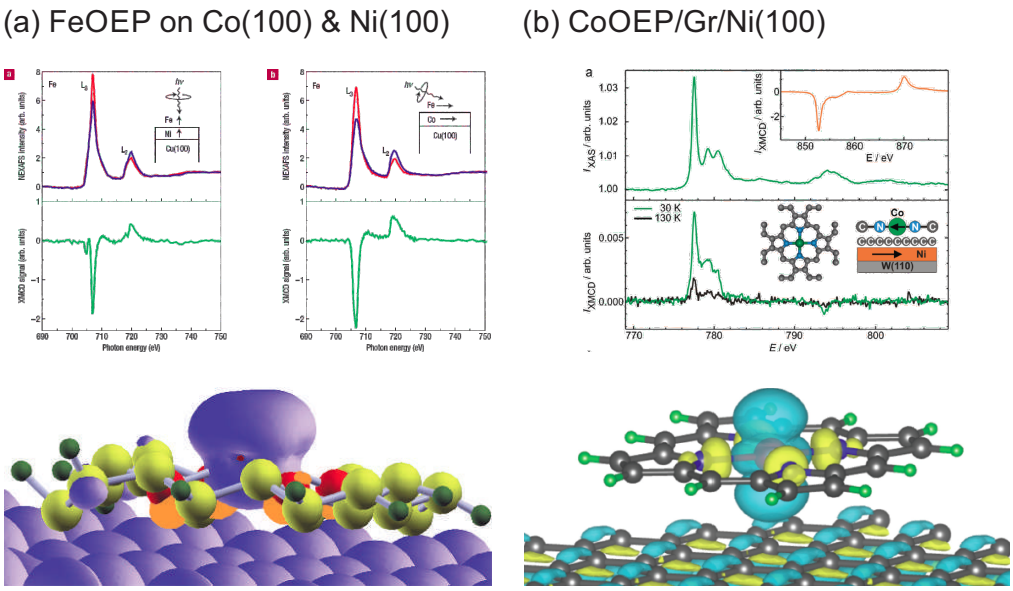

Figure 2.8: (a) Upper panel: magnetic coupling of the FeOEP molecule deposited on Ni and Co substrates determined by XMCD. Lower panel: magnetization density calculated within the GGA+U approximation for the FeOEP, highlighting the FM orientation of Fe and Co spins. The magnetization density iso-surfaces around the Fe and Co atoms are shown in blue. Reproduced from [65]. (b) Upper panel: Co $L_{2,3}$ XAS (upper panel) and XMCD (lower panel) spectra of 0.7 ML CoOEP on graphene/Ni/W(110) at 30 K (green) and 130 K (black). Lower panel: calculated magnetization density of a Co porphin adsorbed on graphene/Ni. The bright yellow hypersurfaces show contours of positive magnetization densities, the light blue hypersurface shows contours of negative magnetization density. Reproduced from [70].

The spin, and the resulting magnetic moment in adsorbed molecules can be controlled also by a "chemical switch". For example, CoTPP can be magnetically decoupled from the Ni(100) substrate by functionalizing the Co metal ion with nitrogen monoxide (NO). This process is reversible: NO can be desorbed from the surface by high temperature annealing, restoring the magnetic coupling to its original state [8]. On the contrary, in low-spin porphyrin/FM interfaces, such as NiTPP/Co(100), NH_3 can act to turn on the magnetic interaction. Also this process is totally reversible by NH_3 thermal desorption [38]. The on/off switch will be discussed in more details in the next section.

2.2.4 Functionalization

The desired electronic, structural and magnetic properties of porphyrins can be finely tuned not only by a careful choice of the central metal ion and proper substrate support, but also by exploiting the coordination-free site available at the metal center. Depending on the needs, several axial ligands, such as O_2, CO, NH_3 and NO, can be used to functionalize the metalloporphyrin layer.

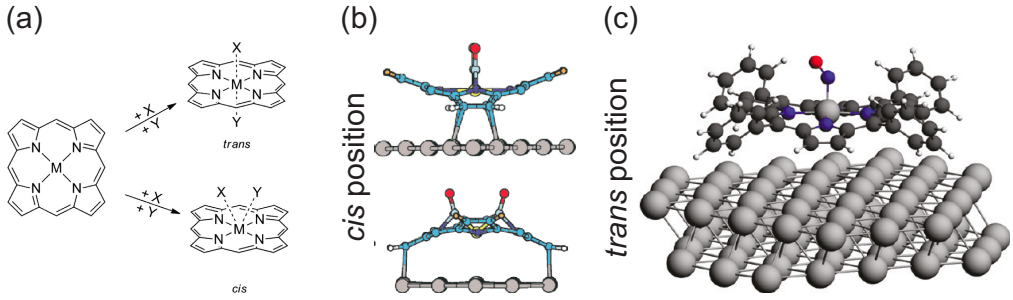

Figure 2.9: (a) Axial *trans*- and *cis*-ligation at a metallo porphin complex. Reproduced from [71]. (b) *Cis*-position example: DFT modelling showing the relaxed geometry of the 2CO-CoTPP system (side and front view). Reproduced from [72]. (c) *Trans*-position example: optimized structures of $(NO)(Ag_{72})$CoTPP. Reproduced from [52].

These ligands can bind to the TPP metal center in two different configurations: in *cis*-position two ligands are attached to the metal center on the same side of the molecule, in *trans*-position, instead, they are located on the opposite sides, as shown in figure 2.9a. The first configuration is less common for MTPP: *cis*-dicarbonyl attachment on CoTPP and FeTPP only occurs at low temperature and it is favored by the saddle-shape deformation of the porphyrin macrocycle (see figure 2.9b) [72]. On the other hand, the *trans*-configuration is well-known to produce appreciable changes in the electronic structure [7] as well as in the magnetic coupling [8, 38] between MTPP and FM substrates. In general, when two ligands are attached in *trans*-position, they compete for the stronger bond at the metal center. This phenomenon is called *trans*-effect. In order to better understand this mechanism, both σ and π orbitals have to be taken into account. Both ligands donate electron density to the metal center through σ-bonds. If one of the two ligands

is a stronger σ-donor (L_S), the bond with the other ligand (L_W) will be weakened. Besides, the metal can donate electron density from its occupied *d* states to unoccupied ligand orbitals *via* π interaction. This charge back-donation increases even more the L_S-M bond strength. Because of this donation/back-donation mechanism, the ligand adsorption configuration is crucial in predicting the strength of *trans*-effect [71].

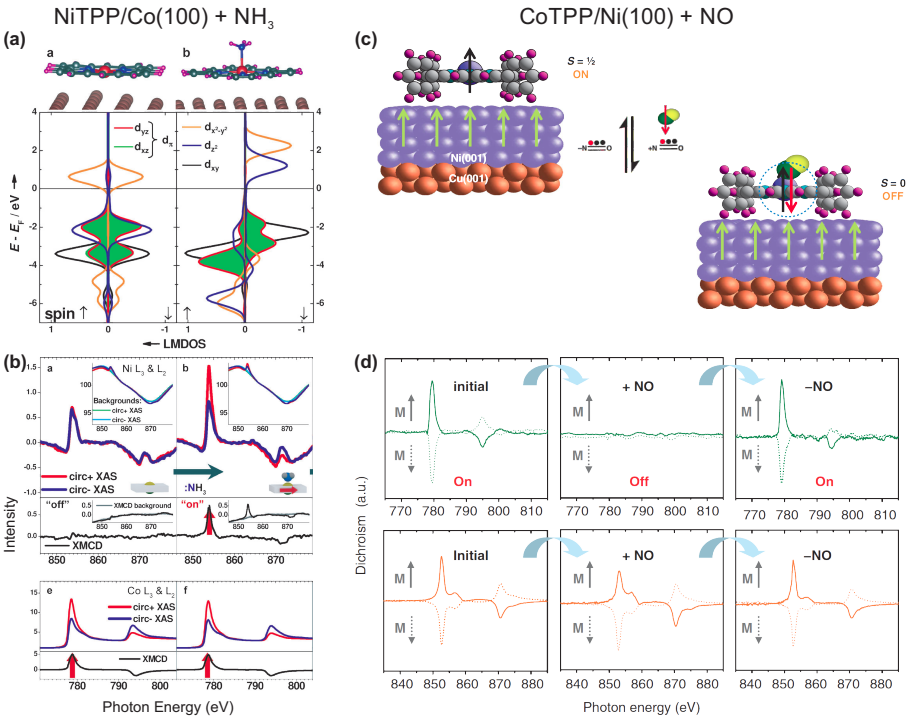

Figure 2.10: (a) DFT+U calculations presenting the spin-projected 3*d* orbital local magnetic density of states (LMDOS) for the Ni-porphine/Co system with S=0 before (left) and with S=1 after (right) reaction with NH_3. The given energies are with respect to the Fermi-level (E_F). (b) XAS/XMCD of Ni in the molecule and the Co substrate of the native NiTPP/Co (left), after exposure to NH_3 gas (right). Reproduced from [38]. (c) Schematic representation of the switching process. Switching on (left): the CoTPP molecule is ferromagnetically coupled to the Ni substrate. Switching off (right): on addition of NO, CoTPP (S = 1/2) forms the NO–CoTPP complex (S = 0) and the spin state of NO–CoTPP remains the same, irrespective of the Ni magnetization. (d) Spin-switching: L-edges XMCD spectra of Co (top panels) and Ni (bottom panels) recorded on the CoTPP/Ni(001) system after the initial preparation of molecular adlayers (left), after NO addition (center) and on temperature-induced NO desorption (right). The directions of the remanent substrate magnetization M are indicated by grey arrows to the left of each spectrum. Reproduced from [8].

Dealing with metalloporphyrins on metal substrates the concept of the *trans* effect can be extended by considering the surface underneath the molecule, as one of the two possible ligand which compete for the stronger bond at the metal center. This is the so-called "surface *trans* effect" (STE). NO adsorbed on CoTPP/Ag(111) can be chosen as example in order to illustrate the effects of such STE.

In absence of NO, some charge is transferred from the Ag substrate to the Co ion the and unoccupied orbitals of the molecule because of the Co-Ag interaction. As a result, a new state close to E_F become populated [16, 52]. Upon NO adsorption, these effects related to the surface-interactions, are no longer observed [52, 7]. This is because NO is a strong σ acceptor, capable of weakening the Co-Ag bond. DFT calculations show that the metal-substrate bond length in MTPP/Ag systems (M = Fe, Co) substantially increases upon NO trans coordination (see figure 2.9c) [52]. As a counterexample instead, the adsorption of CO, which is a much weaker ligand, leaves the electronic structure of CoTPP almost unaffected [73].

The STE concept can be extended to explain the total spin change of MTPP/FM substrate upon ligand coordination. In such systems, STE can modify the strength and the sign of the magnetic exchange interaction between the molecule and the FM substrate. Upon NO-CoTPP/Ni(100) complex formation, the CoTPP unpaired electron, responsible for the ferromagnetic coupling, is paired with the electron supplied by NO ligand (see figure 2.10a and 2.10b), as already mentioned in section 2.2.3 [8]. On the other hand, the NH_3 molecule ($S = 0$) change the spin state of NiTPP ($S = 0 \rightarrow S = 1$), switching-on the magnetic coupling with the underneath cobalt substrate (see figure 2.10c and 2.10d) [38].

The STE will be studied also in this thesis. In particular the attention will be focused on the interaction between NO and a porphyrin layer adsorbed on the copper surface.

Chapter 3

Methods

In this chapter we will introduce the experimental techniques used in this thesis. A brief introduction on photoemission spectroscopy (PES) and X-ray adsorption spectroscopy (XAS) will be given at the beginning. These two techniques can be implemented in a laterally-resolved manner in a photoemission electron microscope (PEEM), giving access to the surface morphology, electronic and magnetic structure at the micron-scale. In its laterally-averaged version, PES is available in the most common laboratory set-ups, which usually include standard energy analyzers and X-ray sources having a fixed wavelength. XAS, instead, requires a tunable light source in a X-ray extended energy range, available only at the synchrotron laboratories. Moreover, the high photon flux density provided by the synchrotron sources makes the laterally-resolved spectroscopy feasible.

Most of the results presented in this thesis have been collected with a modified version a commercially available NanoESCA PEEM. NanoESCA is the acronym for "electron spectroscopy for chemical analysis" at the nanometer scale. This microscope is part of the experimental end-station of the NanoESCA beamline at the Elettra synchrotron facility, Trieste, Italy. This photoelectron microscope is able not only to map the lateral distribution of the photoemitted electrons (real space mode) but also to image at the detector their angular distribution (reciprocal space mode). Therefore, using the NanoESCA set-up, we can study the surface chemistry and magnetic domains as well as the material's band structure, with good spatial ($\sim$ 100 nm) and energetic resolution ($\sim$ 70 meV).

Within the molecular orbital tomography approach, angle resolved photoemission experiments were supported by density functional theory (DFT) calculations performed at University of Graz, Austria by Dr. Daniel Lüftner and Professor Peter Puschnig.

The laterally-averaged XAS and PES measurements, presented in this work, were performed at the ALOISA beamline, at the Elettra synchrotron facility. Near edge adsorption fine structure (NEXAFS) and X-ray photoelectron spectroscopy (XPS) experiments provide an additional insight on the structure, chemical and magnetic properties of the organic/metal interface.

The structural characterization of the organic/metal interface was done by means of low

energy electron microscopy (LEEM), a technique available at the other branch of the NanoESCA beamline, where a commercial LEEM III is installed. The molecular self-assembly and the surface morphology, at the nano-scale level, was studied using a low-temperature scanning tunneling microscope (LT-STM). The LT-STM instrument is located at the CNR-IOM laboratory, Trieste, Italy and operated by the group of Prof. Giovanni Comelli.

3.1 Photoemission spectroscopy

Electrons are photoemitted from matter upon being excited with electromagnetic radiation of sufficient energy. Depending on the wavelength of the incoming electromagnetic radiation exciting the sample, PES is commonly divided into X-ray and ultraviolet photoemission spectroscopies, namely XPS and UPS.

The energy of the incident photon is transferred to an electron. If this energy is large enough to overcome the electron binding energy (BE) in the atom/crystal and the surface work function barrier (in most materials typically 4-5 eV), the electron can escape from the surface into the vacuum as a free electron. It leaves the sample with a well-defined kinetic energy (KE) and starting angle. In the simplest picture, the binding energy (E_B) of the photo-emitted electron can be derived from the equation 3.1:

$$E_K = h\nu - E_B - \phi \tag{3.1}$$

where $h\nu$ is the photon energy, E_K is the kinetic energy of the photoemitted electron and ϕ is the material-dependent work function. In PES, the photoelectrons are excited with monochromatized photons and then filtered according to their kinetic energy, using a spectrometer. Figure 3.1 (top right) shows a prototypical photoemission spectrum of a metal with the valence band crossing the Fermi level. In the spectrum, the core levels appear as well-defined lines because they are bound at discrete energy values. The valence band, instead, does not show sharp features because the electronic states are densely distributed over a wider energy range.

In a first approximation, the photoexcitation process can be described as a single electron process [74]. The electron is excited by a photon with energy $h\nu$ from its initial Bloch state $|i\rangle$ into a final unoccupied Bloch state $|f\rangle$. The transition probability ($w_{i\to f}$) from the initial to the final state is described by Fermi's golden rule:

$$w_{i\to f} = \frac{2\pi}{\hbar} |\langle f| H |i\rangle|^2 \cdot \delta(E_f - E_i - h\nu) \tag{3.2}$$

where H is the perturbation Hamiltonian of the photoexcitation and the δ function ensures the energy conservation. From equation 3.2 it becomes clear that the probability of the photoemission process always depends on the initial and final state, with the respective transition matrix element $M_{fi} = \langle f|H|i\rangle$ describing the interaction of an electron with the incident electromagnetic wave. In

first order perturbation theory the operator H can be described as:

$$\mathrm{H} \approx \frac{\hbar e}{mc}\mathbf{A}\cdot\mathbf{k} \tag{3.3}$$

where $\mathbf{k}$ is electron wave vector and $\mathbf{A}$ the electromagnetic vector potential. If $\mathbf{A}$ changes only slightly over atomic distances, the matrix element can be approximated as:

$$\mathrm{M_{fi}} \approx -\frac{ie}{c}A_0(E_f - E_i)\,\langle f|\,|\hat{\mathbf{P}}\cdot\hat{\mathbf{k}}|\,|i\rangle \tag{3.4}$$

Here $\mathrm{A_0}$ is the amplitude of the vector potential and $\hat{\mathbf{P}}$ the electric polarization. This is the so-called *dipole approximation* and, in general, holds for photon energies within the VUV and soft X-ray energy range. In this way, M_{fi} can be analyzed with respect to the symmetries of $|f\rangle$, $|i\rangle$ and $\hat{\mathbf{P}}$, in order to formulate the dipole selection rules. These rules can be applied to qualitatively analyze photoemission spectra in terms of allowed transitions[75].

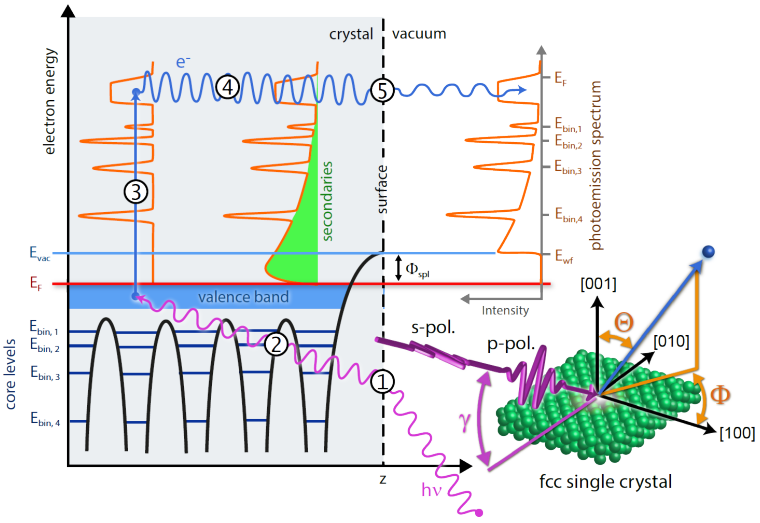

Figure 3.1: Photoemission in the three-step model. An electromagnetic wave is refracted at the surface (1) and penetrates through the solid (2) and excites a photoelectron (3). The photoelectron propagates through the solid to the surface (4) and might undergo elastic and inelastic scattering processes. The latter generates secondary electrons. The electron wave is finally refracted at the surface (5). If its energy is high enough to overcome the surface potential barrier it escapes into the vacuum and can be detected by a photoelectron analyzer. The 3D sketch shows a photoemission process seen from outside the solid. The incident angle and the polarization of the electromagnetic wave have an influence on which electron orbitals in the crystal are addressed and under which solid angles the excited photoelectrons escape the crystal. Reproduced from [76].

The simplest theoretical approach, which describes the photoemission process, is the so-called *three-step model*, proposed by Berglund and Spicer in 1964 [77] and it is schematically sketched in figure 3.1. This model involves three independent processes: photoabsorption of the

electromagnetic radiation, propagation through the surface of the excited electron and escape of the photoelectron into the vacuum.

In the first step electrons are excited from their initial state $|i, \mathbf{k}_i\rangle$ into a final state $|f, \mathbf{k}_f\rangle$. Energy and momentum conservation sets the following relation:

$$E_f = E_i + h\nu \tag{3.5}$$

$$\mathbf{k_f} = \mathbf{k_i} + \mathbf{G} \tag{3.6}$$

In equation 3.6 the momentum carried by the photon and transmitted to the electron is neglected. This assumption is valid for the in UV-soft X-ray energy range. The addition of the reciprocal lattice vector **G** preserves the momentum conservation [78].

The second step regards the propagation of the photoelectron in the material. The motion of electrons approaching the surface is disturbed by the inelastic scattering with other electrons, phonons or defects. The quantity which describes the average distance between two inelastic scattering processes in λ, the inelastic mean free path (IMFP):

$$\mathrm{I}(d) = \mathrm{I}_0 \exp(-d/\lambda) \tag{3.7}$$

$\mathrm{I}(d)$ is the attenuation of the photoemission current as a function of the path length d. Due to the exponential $\mathrm{I}(d)$ decay, 95% of the probed photoemitted electrons comes from $\sim 3 \cdot \lambda$ depth. In the energy range of 40-100 eV λ is in the order of 5-10 Å, which explains why PES is a surface sensitive technique: most of the photoelectrons come from the very first layers of the sample surface although the x-ray beam penetrates deeper into the crystal. The inelastically scattered electrons contribute to the photocurrent with a broad and featureless background (called secondary background), while elastically scattered electrons give rise to sharp peaks [79].

The last step describes the escape of photoemitted electrons from the surface to the vacuum. The parallel component of the photoelectron momentum ($\mathbf{k}_\parallel$) is conserved through the crystal surface, while the perpendicular component ($\mathbf{k}_\perp$) is not, because of the symmetry breaking along the z direction. In particular, the initial $\mathbf{k}_\parallel$, which is equal to $\mathbf{K}_\parallel$ (the parallel momentum of the photoelectron in the vacuum),

$$\mathrm{k}_{\mathrm{x},\parallel} + \mathrm{k}_{\mathrm{y},\parallel} = \mathbf{k}_\parallel = \sqrt{\frac{2m}{\hbar^2}\mathrm{E_K}} \cdot \sin(\theta) \tag{3.8}$$

can be determined from two measurable quantities $\mathrm{E_K}$ and θ (the exit angle of the photoemitted electron) [78]. The 3-dimensional band structure ($\mathrm{E}(\mathbf{k})$), instead, can be measured only when determining $\mathrm{k}_\perp$. The perpendicular component can be approximated as:

$$\mathrm{k}_\perp = \sqrt{\frac{2m}{\hbar^2}(\mathrm{E_K}\cos^2(\theta) + \mathrm{V}_0)} \tag{3.9}$$

$V_0 = E_0 + \Phi$ is called the *inner potential*, and it corresponds to the lowest energy level of the valence band E_0 with respect to the vacuum level. The *inner potential* complicates the 3D band structure mapping, because it can be only empirically determined and requires a tunable light source (the photon energy needs to be changed in order to change E_K).

Although the three-step model provides a qualitative description of the photoemission process, the influence of the sample surface is not properly taken into account since there is no distinction between bulk and surface electron. A more accurate and quantitative interpretation of photoemission spectra is given by the one-step model, which treats the photon excitation, electron removal and detection as a single quantum-mechanical process [80]. Within this formalism surface states, transition into evanescent final states and multiple final state scattering effects, due to electron-electron correlation, can be adequately described [81].

3.2 Absorption spectroscopy

X-ray absorption spectroscopy (XAS) is a widely used experimental technique for determining the local electronic and geometric structure of matter. If an x-ray beam, of I_0 intensity, traverses a specimen, the attenuation of the initial flux depends on the photon energy E and sample thickness d. According to Beer's law, the intensity transmitted ($I(d)$) is:

$$I(d) = I_0 e^{-\mu(E)d} \tag{3.10}$$

$\mu(E)$ is the *total attenuation coefficient*, which depends on photon energy, sample composition and density [82]:

$$\mu(E) \sim \rho Z^4 / m E^3 \tag{3.11}$$

(Z and m are the atomic number and mass, respectively). In the soft x-ray energy range, the principal mechanism contributing to the X-ray attenuation is the photo-electronic absorption, *i.e.* photons are absorbed during the excitation or ionization of the sample's atoms. The total attenuation coefficient μ is thus approximated with the *photoelectric adsorption coefficient* [82].

From equation 3.11 it is clear that $\mu(E)$ decreases smoothly increasing E. However, when the photon energy crosses the binding energy of a core-shell electron a new absorption channel becomes available, producing a sharp increase in the X-ray absorption, which interrupts the $\mu(E)$ monotonic decay: the so-called *absorption edge*. Edges are labeled using the principal quantum number of the excited shell: K for n = 1, L for n = 2, M for n = 3, *etc*. The angular momentum and spin-orbit coupling split the edges, *e.g.* L_1 ($2s$), L_2 ($2p_{1/2}$), L_3 ($2p_{3/2}$) for the L edge. Like for BEs, the edge energy position depends on the atomic species involved, providing XAS with chemical sensitivity [83]. For acquiring XAS spectra, the photon energy has to be tuned across a specific absorption edge, therefore, a tunable light source, like a synchrotron, is required.

The absorption of an ionizing X-ray leaves the atom in a excited state which relaxes *via* different mechanisms, with the two most important being emission of an Auger electron or an X-ray photon.

The energy of an emitted Auger electrons is very specific because it depends from the transitions between energetic sharply defined levels.

Both processes (Auger electron emission and X-ray fluorescence) are directly proportional to the amount of core-holes created in the X-ray absorption, therefore they can be used as a measure of the absorption coefficient. The radiative emission can be detected with a fluorescence detector, the partial electron yield (PEY), instead, can be measured with channeltron or an energy analyzer. The total electron yield (TEY), produced in the filling of the core-holes induced by the x-ray absorption, is usually measured with a picoammeter. In the soft X-ray energy range, the electron yield is much stronger than the fluorescence yield and provides a higher surface sensitivity [84].

The modulation of μ, across the adsorption edge, is called X-ray absorption fine structure (XAFS). For isolated atoms XAFS is limited to few eV around the edge, reflecting the transition from core levels to unoccupied states. In condensed matter, instead, XASF is also influenced by the neighbor atoms surrounding the absorber, resulting in a intensity modulation of the spectra which can extend for several hundreds of eV. For this reason, XAS spectra are commonly divided in two different regions:

1. **NEXAFS** (near edge XAFS), up to 30/50 eV above the edge.
2. **EXAFS** (extended XAFS), from 30/50 eV up to even 1000 eV above the edge.

The main difference between NEXAFS and EXAFS is that the sensitivity of the former is related mainly to the unoccupied electronic structure [85], whereas the latter depends predominantly on the relative atomic positions of the emitter to the nearest neighbors [86].

3.2.1 NEXAFS

General principle

The electronic transitions between the excited core level and the empty bound states in the valence band are responsible for the near-edge features in the absorption spectrum. The edge, instead, defines the ionization threshold. The position and the intensity of the edge depends on the specific element's valence state: increasing, for example, the oxidation state will shift the edge towards higher energies [85]. NEXAFS is dominated by multiple-scattering resonances of the photoelectrons ejected at low kinetic energy. The spectral lineshape is very sensitive to the band structure, as well as the atomic position of neighbors and bond angles.The XAS measurements presented in this thesis will regard mostly the pre-edge/edge and NEXAFS regions.

Stöhr and Outka, in their work published in 1987 [87], presented a model for recognizing the molecular orientations on surfaces from the angle-dependent NEXAFS spectra. They observed that in the K-shell (1s) NEXAFS of chemisorbed molecules on surfaces, the transitions to highly localized molecular π^* and σ^* orbitals, which contribute mostly to the spectrum, are not strongly affected by the interaction with the surface. These orbitals have a well-define spatial orientation which can be determined by acquiring different XAS spectra, varying the angle of the linearly

polarized light with respect to the scattering plane. The model gives quantitative results on the orbital geometry. The strong angle-dependence of the XAS intensity is related to the symmetry of the initial (1*s*) and the final π^* and σ^* states involved in the electronic dipole transitions. The dipole selection rules enhance the σ^* (π^*) resonance when the electrical field vector **E** of the incoming radiation is parallel to the σ^* (π^*) orbital axis. Instead, when **E** is perpendicular, the transition probability drops to zero. Therefore, by changing the direction of **E**, the orientation of π^* and σ^* can be determined. This is usually done in a grazing incidence conditions, by rotating the sample along the axis identified by the beam direction. Generally, measuring XAS at two different incidence angles (**E** $\parallel$ and almost $\perp$ to the surface) is enough to understand the orientation of the orbitals owning a well-defined σ or π character.

ALOISA beamline

NEXAFS experiment were carried out at the ALOISA (Advanced Line for Overlayer, Interface and Surface Analysis) beamline at the Elettra synchrotron facility in Trieste. ALOISA[1] is a multipurpose beamline dedicated to the chemical and structural characterization of surfaces, adsorbates and ultra-thin films. The wide energy range of the beamline and the complete set of detectors in the end-station allow the users to combine *in-situ* structural and chemical investigation techniques, such as XPS, PED and XAS. A grating-crystal monochromator is employed to cover a photon energy range spanning 130-1500 eV. The experimental workstation consists of two separated UHV chambers: the preparation chamber for the sample cleaning and preparation and the experimental chamber surrounded by a μ-metal shielding to screen the sample from stray magnetic fields which could deflect the electron trajectories. The experimental station is equipped with a combination of electron spectrometers and energy-resolved photodiodes for detecting both electrons and photons. The whole set of different detectors is hosted onto rotating frames inside the experimental chamber in order to perform complementary measurements in UHV conditions.

3.3 PEEM

Photoemission electron microscopy (PEEM) is a full-field, direct imaging technique. The microscope collects the photoemitted electrons in order to image a restricted portion of the specimen area. After being emitted, electrons are accelerated by a strong electric field through the first lens, the objective, also known as cathode lens. The objective produces a magnified image of the specimen and, simultaneously, creates an image of the diffraction pattern for crystalline surfaces, located in the lens back-focal plane (BFP) [88]. After the objective lens, other electron optical elements, which form the imaging column of the microscope, project the magnified image of the sample onto an imaging detector. Some instruments are also equipped with an energy analyzer, which allows one to select only photoemitted electrons with a well defined kinetic

[1] http://www.elettra.trieste.it/elettra-beamlines/aloisa.html.

energy. While the energy filter is essential to implement laterally resolved version of the most important synchrotron radiation spectroscopies, namely PES and ARPES, spatially resolved XAS and XMCD can be performed without it [89].

Photoemission electron microscopy, combined with synchrotron radiation, is a powerful technique to image surfaces, interfaces and thin films with high sensitivity to their chemical and magnetic state, as well as their electronic structure. It can be seen as an evolution of the classical powerful photoemission spectroscopy which preserves both spatial resolution and information on the emission angle of the photoemitted electrons [90, 91].

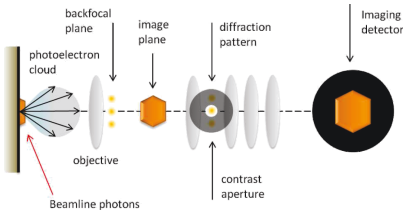

Figure 3.2: Simplified scheme of the PEEM working principle. Reproduced from [88].

3.3.1 NanoESCA microscope

Instrumental aspects

Developed in 2005, the NanoESCA microscope is one representative of commercially available energy filtered PEEMs [92]. It conciliates a good energy resolution with an adequate spatial resolution. The microscope consists of a first optical column, which collects the electrons photoemitted from the specimen; a subsequent double-hemispherical energy analyzer, which preserves the image during the energy filtering process; and a second optical column, which projects electrons onto the 2-D detector. Another 2-D detector is located, in a straightforward configuration, immediately after the first optical column. Furthermore, the microscope has, after the first hemisphere, a channeltron. All these elements, combined together, allow the microscope to operate in three different modes:

- **PEEM** The energy filter is not used. An image of the full photoelectron yield which leaves the sample in a certain area is magnified and projected on the extra 2D detector, placed immediately after the first optical column. This mode is often used in laterally-resolved XAS and XMCD measurements.

- **Energy-filtered PEEM** Photoemitted electrons, carrying the image information, are transmitted through the double-hemispherical energy analyzer. Only photoelectrons with a well-defined kinetic energy can pass the filter allowing for element-selective imaging.

- **Channeltron** After the first hemispherical analyzer, all photoelectrons of a defined KE, passing through the filter, are counted by the channeltron. The spatial resolution is sacrificed in favor of spectra with better counting statistic.

The microscope layout is shown schematically in figure 3.3. The objective, which is the most important lens, magnifies a portion of the sample surface and strongly affects the overall energy/lateral resolution and transmission of the microscope. A strong accelerating electric field is

applied between the sample and the objective, which draws the photoelectrons into the microscope column and creates a first intermediate image at the position of the iris aperture. The iris aperture defines a specific area of the projected image from which the photoelectron distribution can pass further into the microscope. The strong applied field, bends the photoelectron trajectories towards the optical axis of the microscope. Furthermore, a set of contrast apertures (CA) having different sizes, can be inserted at the back-focal plane of the objective lens, limiting the angular spread of photoelectrons. In this way, the spatial resolution can be increased but, at the same time, the microscope transmission will be lowered.

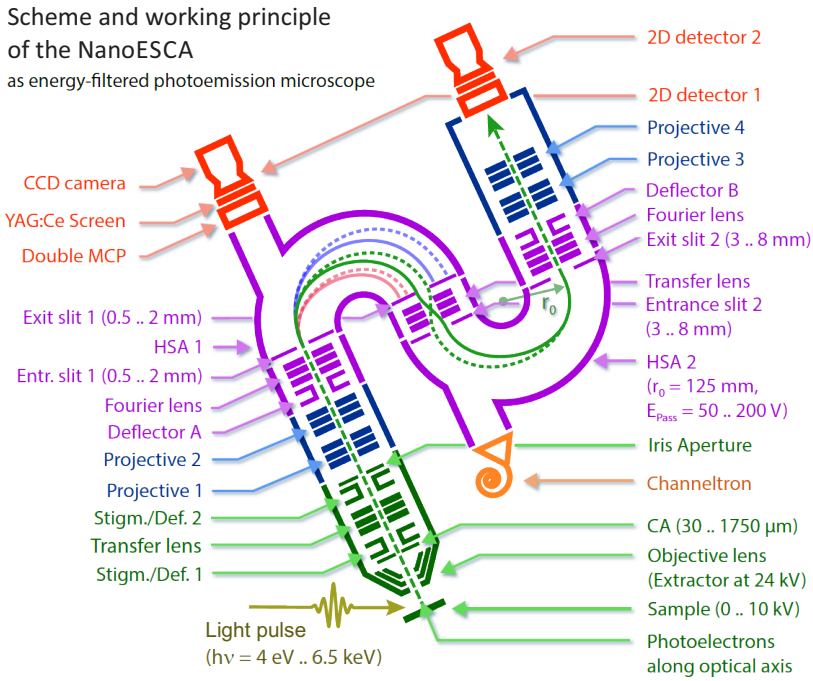

Figure 3.3: Scheme of the NanoESCA photoemission microscope. The photoemitted electrons travel through four main instrument parts: objective, first projection column, energy-filter and second projection column, until they reach the imaging detector. Two extra measurement modes are available: PEEM mode, where electrons are projected onto a 2D detector without the energy-filter. In the latter mode, photoemitted electrons are filtered only by the first HSA, losing the spatial information. Reproduced from [76].

The transfer lens is the optical element which provides an extreme flexibility to this microscope. It is needed to transfer the objective back-focal plane instead of the image plane through the electron optical path, allowing the microscope to switch between two different configurations:

- **Imaging (Real Space)** The photoelectron distribution is directly imaged on the 2D detector. The spatial information of the photoemitted electrons is preserved, while integrating over a range of emission angles in each point determined by the size of the contrast aperture. This

configuration works in both PEEM and energy-filtered PEEM modes.

- **Diffraction (Reciprocal Space)** The angular distribution of the photoemitted electrons is preserved, while averaging over an well-defined area of the sample. This configuration is used predominantly in the energy filter mode, thus enabling to access the electronic structure of solid surfaces, *i.e.* the electron band structure.

The two configurations are schematically summarized in figure 3.4.

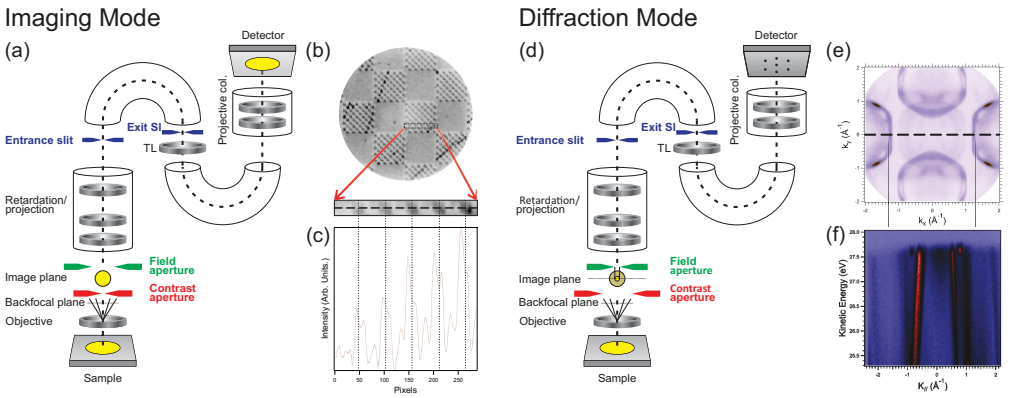

Figure 3.4: The scheme compares the imaging and diffraction operation modes. Left: Imaging mode (real space). (a) Spatially-resolved images are acquired from a specimen and projected onto the 2D detector. In order to increase the spatial resolution the contrast aperture can be inserted in the back focal plane of the objective lens. (b) Photoelectron distribution is laterally mapped at different sample positions. (c) Line profiles at different sample positions can be taken for a quantitative analysis of the electron distribution. Right: Diffraction mode (reciprocal space). (d) the back-focal plane of the objective is projected on the detector. The energy filter allows one to acquire the photoelectron distribution at different electron kinetic energies. To limit the surface probed area, a field limiting aperture, *i.e.* an iris aperture, can be closed at the first image plane after the objective lens. (e) Resulting angle resolved photoemission patterns. (f) Energy distribution curves are obtained by cutting, with a line profile, a stack of angle resolved photoemission maps, acquired varying electron kinetic energy.

The energy filter is the central part of the microscope: it consists of two (almost identical) hemispherical sector analyzers (HSA) in a point-symmetrical configuration (see figure 3.3). Electrons traveling in the first HSA are separated as a function of their kinetic energy, due to the dispersive effect of the electric field applied between an inner and outer part of the HSA. Two sets of rectangular slits, one at the entrance and the other at the HSA exit, define a small KE bandwidth which allows only electrons traveling on the correct trajectories to pass through. These slits are inserted at the center of the hemisphere mean radius. Electrons entering perpendicular to the entrance slit plane, must have a defined kinetic pass energy (E_{pass}) to travel through the HSA and leave the exit slit as well centered and perpendicular to it. The task of the second HSA is to correct the dispersive effect introduced by the first hemisphere, avoiding chromatic errors in a PEEM image sent through the filter [92]. The relevant parameters of the analyzer are given in table 3.1.

Table 3.1: Technical details of the energy filter.

HSA mean radius	125 mm
$\mathbf{E_{pass}}$	from 50 to 200 eV
Entrance slit size (short side)	0.2, 0.5, 1, 8 mm
Exit slit size	3, 4, 8 mm

The filtered photoelectrons are projected onto a double microchannel plate (MCP), which is an electron multiplier. The electrons are then accelerated towards a scintillator-screen, which is made of Cerium-doped Yttrium Aluminum Garnet (YAG:Ce). The light produced by this fluorescence screen is recorded by a digital fast-acquisition CCD camera. The YAG crystal operates in UHV, while the CCD camera is on the atmospheric pressure side, separated by a UHV-window. The images are subsequently transferred to the acquisition computer and saved for further evaluation.

In the *channeltron mode*, photoemitted electrons travel only through the first HSA and then, losing their spatial distribution, they are collected into a channeltron, placed immediately after the analyzer exit. This operation mode benefits from a better counting statistics, without the addition of artifacts coming from a more complicate acquisition set-up, like the one used for the image detection. Although the channeltron has no spatial resolution, closing the iris aperture in the first image plane, allows one to count only electrons coming from the selected region of interest on the sample surface. The iris can be closed down to approximately 6 μm in diameter. The parameters describing the overall performance of the microscope are summarized in table 3.2.

Table 3.2: Performances of the NanoESCA microscope.

Lateral resolution	>100 nm
$\mathbf{k_{\parallel}}$ **resolution**	$\sim$ 0.04 Å^{-1}
Energy resolution	80 meV @ 140 K
Exit slit size	60 meV @ 80 K
min T	80 K with LHe cooling

The NanoESCA Beamline

The NanoESCA beamline[2] has been designed to deliver high photon flux density at the microscope focus in order to maximize collection efficiency. It offers intermediate energy resolution up to a photon energy of 1000 eV. Two Sasaki type undulators with a period of 10 cm, phased by a electromagnet modulator, are used as source; they provide elliptically polarized radiation, as well as vertical and horizontal linear polarization as special cases. The beamline employs a high throughput monochromator based on the variable line spacing (VLS) grating scheme, covering the energy range from 40 to 1000 eV, and one spherical grating for low energies. The beamline is split in two branch lines, alternatively operated by means of a deflecting mirror located after the

[2] http://www.elettra.trieste.it/elettra-beamlines/nanoesca.html

monochromator exit slit. Each branch features a refocusing section with two bendable elliptical mirrors arranged in the Kirkpatrick-Baez configuration. They permit a strong demagnification of the source, achieving a micron-sized illumination spot at the microscope focus, matching the typical working conditions. A scheme of the beamline is shown in figure 3.5.

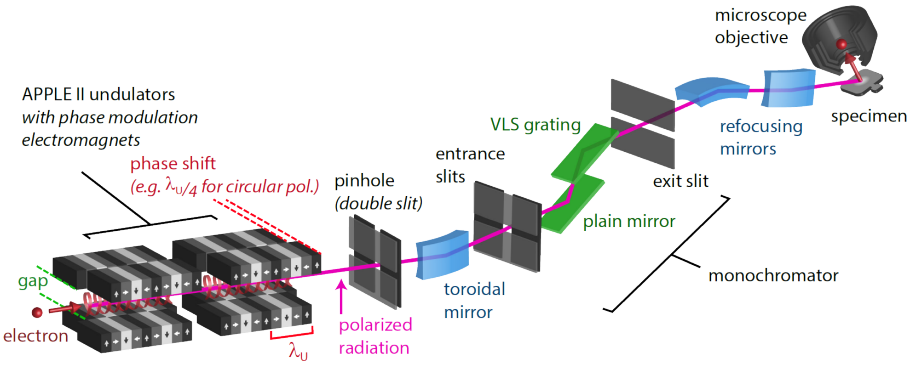

Figure 3.5: Scheme of the NanoESCA beamline at Elettra. The gap and the phase shift of the two undulator columns can be adjusted to generate photons with a specific energy and polarization (vertical linear, horizontal linear, left or right circular). Unwanted radiation is stopped by the pinhole and the transmitted beam is demagnified by a toroidal mirror before it enters the monochromator. The angle of the plain mirror and the grating can be adjusted to reflect a nearly monochromatic beam with the desired photon energy onto the exit slit. The width of the exit slit determines the final energy resolution. The refocusing mirrors finally produce a small beamspot on the specimen.

The beamline and monochromator specifications are summarized in table 3.3:

Table 3.3: Beamline specifications.

Photon source	2 Apple II type undulators with 10 cm period and phase modulation electromagnet
Polarization	linear horizontal and vertical, elliptical
Energy range	40-1000 eV
Source size	560 μm x 55 μm (Hor. $\times$ Vert.) FWHM
Beamline Horizontal demagnification	x45
Beamline Vertical demagnification	x92
Beamspot on the sample	20 μm x 10 μm (Hor. x Vert.) at 24° grazing incident

The monochromator specification are summarized in table 3.4:

Table 3.4: Monochromator specifications.

Grating	Energy Range (eV)	Resolving Power	Maximum Flux (2 GeV, 200 mA)
VLS 400	200-1000	4000 @ 400 eV	$1 \cdot 10^{12} ph/s$ [250-600 eV]
VLS 200	40-300	4000 @ 200 eV	$1 \cdot 10^{13} ph/s$ [100-200 eV]
Spherical Grating 10	3-40	1000 @ 20 eV	$1 \cdot 10^{13} ph/s$ [40 eV]

3.3.2 Laterally resolved XPS

As described in section 3.1, measuring the energy of photoemitted core shell and valence band electrons, provides chemical and electronic structure information on the surface. Laterally resolved photoemission spectroscopy, performed by exciting the sample with X-ray radiation (XPS), can be performed with our PEEM. In XPS the photon wavelength is fixed and the analyzer measures the kinetic energy of photoelectrons. In the simplest picture, the binding energy (E_b) of the photo-emitted electron can be derived from the equation 3.1. In practice, E_K is unknown and can be replaced by a bias voltage applied to the sample, often referred to as E_{kin}, and ϕ can be interpreted as the work function difference between sample and analyzer. Referencing the energy scale to the Fermi level permits a reliable determination of the electron binding energies. By acquiring images at different values of the sample bias, it is possible to measure the energy spectrum of photoelectrons in a laterally-resolved manner. Since the core-level photoemission intensity is directly proportional to the number of surface emitters, PEEM can provide a quantitative estimate of the local coverage of a certain adsorbate. In addition to the intensity, binding energy shifts due to different chemical environments may cause further contrast variations, permitting the identification of chemically non-equivalent atoms of a given species.

Chemical contrast in laterally resolved XPS

The element specificity of binding energies in XPS allows one to probe the chemical composition of surfaces. By setting the energy of the band pass filter we can select electrons with a well-defined binding energy, constructing a PEEM image showing the lateral distribution of the corresponding emitters. Since the photoemission intensity is proportional to the amount of one particular element on the surface, we can thus obtain laterally resolved maps of the surface composition. In this type of measurements the photon energy is chosen to maximize both photo-emission cross section and sensitivity to the surface emitters.

The energy-filtered PEEM also allows one to select photoelectrons emitted from atoms experiencing a different chemical environment or bonding configuration, whose binding energy is shifted from the main emission line. Accordingly, chemical contrast will arise in PEEM due to sensitivity to the different chemical states of the same element on the surface [93].

Work function contrast

Energy-filtered-PEEM can also measure the lateral variations of the surface work function using secondary electrons.

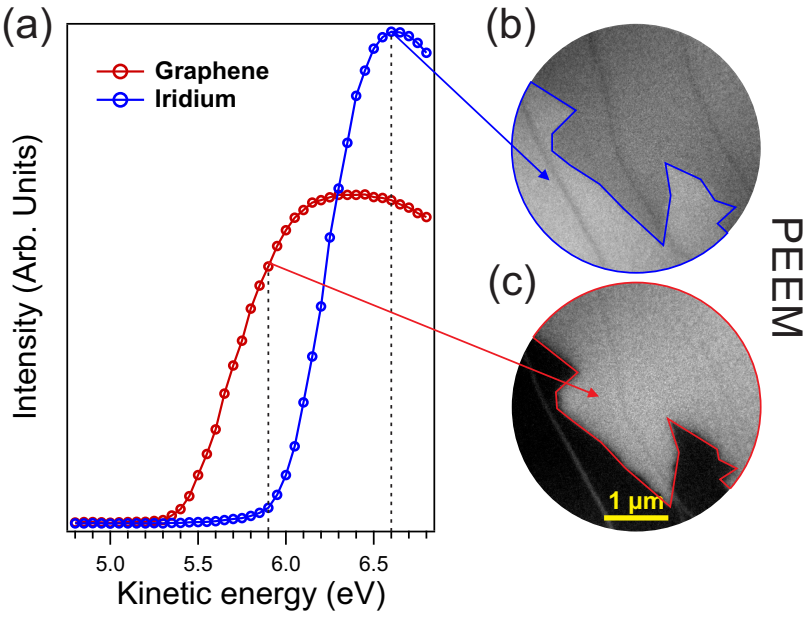

Figure 3.6: Work function contrast of graphene on Ir(100). (a) Average photoemission intensity in ROI in graphene and Ir plotted as a function of the electron kinetic energy. (b) and (c) PEEM images taken at different electron kinetic energies, maximizing the intensity of the graphene island or that of Ir. $h\nu = 40\ eV$.

Figure 3.6 illustrates an example of work function contrasts in PEEM images: graphene on Ir(100). Fig. 3.6a shows the photoemission spectra of the secondary electrons acquired from well-defined regions of interest (ROI) located inside and outside the graphene flake. The spectra were extracted from a sequence of PEEM images ($h\nu$ = 40 eV) recorded in the bias voltage range from just below the iridium work function (where photoelectrons cannot leave the surface) up to 3 eV. Each data point was obtained by calculating the average image intensity within the ROI defined above.

This kind of measurements makes it possible to extract information about work function differences, which can be then referenced to a known value. Figure 3.6b and 3.6c are taken for different electron kinetic energies, fig. 3.6b is acquired at the maximum intensity of the iridium peak. Looking at the figure 3.6b it is clear that the maximization of the contrast occurs when the difference between the blue and the red curves is largest, which occurs at kinetic energy value of 5.9 eV. Owing to the higher work function of Ir with respect to that of graphene, the graphene show up brighter at low E_{kin}, as shown in fig. 3.6c.

3.3.3 μ-ARPES

As anticipated in section 3.3.1, this microscope is able to image directly a large portion of the angle-resolved photoemission pattern (ARPES), thus enabling the access to the electronic structure of solids, surfaces and adsorbed molecular systems. In this mode, both energy and in-plane momentum k of the photoemitted electron can be measured simultaneously. This is possible because the energy (see equation 3.1) and k (see equation 3.8) are conserved in the photoemission process. In particular, k is conserved within a unit vector of the reciprocal lattice $\mathbf{G}$, due to the translational symmetry of the lattice:

$$\mathbf{k}_{\parallel}^{\mathbf{f}} = \mathbf{k}_{\parallel}^{\mathbf{i}} + \mathbf{G}_{\parallel} \tag{3.12}$$

This not true for $k_{\perp}$, due to the potential barrier at the surface (see section 3.1). By changing the photon energy, however, the entire band structure can be determined.

While a standard ARPES measurement is performed by scanning the azimuthal and polar angles, NanoESCA acquires 2-dimensional maps of the angular distribution of photoemitted electrons in a single image, when operated in the diffraction mode. The wide angular acceptance of the objective lens allows one to probe the entire Brillouin zone of most materials, *i.e.* $\sim \pm 2$ Å. By varying the kinetic energy of the electrons admitted into the energy filter, we can acquire series of APRES patterns corresponding to different binding energies. Accordingly, the band dispersion along high-symmetry directions can be obtained by taking the corresponding intensity profiles within such image stacks. The insertion of a field limiting aperture (see section 3.3.1) restricts the probed surface area down to few μm^2, for this reason this method is also called μ-ARPES.

3.3.4 Laterally resolved XAS

Laterally-resolved X-ray absorption spectroscopy, in the NanoESCA instrument, is performed by measuring the intensity of the secondary emission yield as a function of the photon energy. The energy resolution is ultimately determined by the x-ray monochromator, and in principle no energy analyzer would be required. Moreover, the large electron inelastic mean free path at low kinetic energies (typically less than 10 eV) allows one to probe buried layers and interfaces down to a depth of more than 5 nm.

Furthermore, the magnetic state of surfaces, thin films and buried layers, imaging ferromagnetic and antiferromagnetic domains can be studied combining PEEM with circular and linear dichroism [90].

3.4 LEEM

3.4.1 Working principle

LEEM is a cathode lens microscopy technique which probes surfaces and interfaces with elastic backscattering of low energy electrons. Owing to the large electron backscattering cross section of

most materials, LEEM warrants acquisition at video rate. Therefore, it is particularly well suited to monitor dynamic processes, such as surface reconstructions, epitaxial growth, step dynamics, self-organization, *etc*. LEEM adds structure sensitivity to the capabilities of synchrotron based PEEM, providing several complementary methods for structural characterization, of which the most important is low energy micro-probe electron diffraction (μ-LEED).

The basic scheme of a LEEM apparatus is shown in fig. 3.7. The electrons are emitted from a cathode and are accelerated to an energy of several keV. The beam separator deflects electrons from their original trajectory allowing them to reach the surface at normal incidence. Before reaching the sample the electrons are decelerated to low kinetic energy. The kinetic energy range is generally tuned in the range from 0 to few hundreds eV. Electrons interact with the surface and are elastically backscattered. Reflected electrons are then re-accelerated through the objective lens, following the same pathway in reverse. The objective produces a magnified image of the specimen in the beam separator, which is further magnified by several additional lenses in the imaging column of the instrument. This image is projected onto an imaging detector with microchannel plate and phosphorous screen, and finally acquired by a computer controlled CCD camera. Along with real space imaging, a LEEM microscope is also capable of reciprocal space imaging. The first diffraction plane along the LEEM electron optics is in the back-focal plane of the objective lens. By changing the excitation of the lenses in the imaging column, it is straightforward to produce a magnified image of the diffraction pattern, thus, a LEEM microscope can be used as a LEED instrument [94, 95].

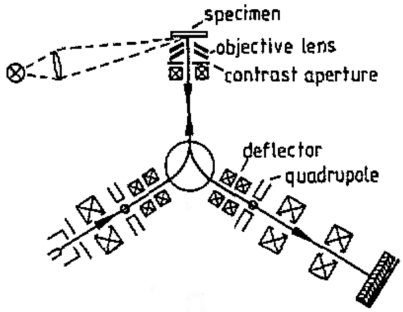

Figure 3.7: Simple scheme of the first LEEM apparatus [94].

3.4.2 SPELEEM microscope

The spectroscopic photoemission and low energy electron microscope (SPELEEM) is a hybrid LEEM-PEEM microscope equipped with band-pass energy filter [96]. The SPELEEM is a multi-method instrument offering imaging, microprobe-diffraction, and microprobe-spectroscopy. Depending on whether electrons or photons are used as probe, one can carry out LEEM or PEEM imaging. By choosing diffraction operation, μ-LEED, microprobe x-ray photoelectron diffraction (XPD) and μ-ARPES are available, all requiring the use of the energy filter. Microprobe spectroscopy, or μ-XPS, is yet another operation mode, which allows fast spectroscopy from micron-sized areas. The regions of interest are selected by means of special apertures inserted in the optical column of the instrument.

In the SPELEEM, the electron kinetic energy is controlled by biasing the sample with a negative potential. This bias is referred to as Start Voltage (SV). The kinetic energy of the electrons scattered (or emitted) by the sample is equal to $E_{\text{kin}} = \text{SV} - \delta W_{\text{i-s}}$, the latter being the difference in work

function between the instrument (i) and the specimen (s).

SPELEEM can also image the dispersive plane of the analyzer onto the 2D detector. The dispersive plane appears as a line, whose intensity profile represents the photoemission spectrum. In this operation mode the microscope reaches its best energy resolution, which can be as low as 110 meV in favorable cases. The field-limiting and contrast apertures determine the probed area and angular acceptance, respectively.

The SPELEEM allows also to measure the LEED pattern of a microscopic area of the sample. The microscope is provided with apertures, to be inserted in the image plane located at the beam splitter on the illumination column side. These apertures reduce the size of the electron beam, allowing us to illuminate very small surface regions. Three illumination apertures with diameters of 0.5 μm, 1 μm and 5 μm are available. μ-LEED is used to characterize the structural properties of surfaces and interfaces on the micron scale, providing access to surface phases and reconstructions, rotational domains *etc*.

3.4.3 Contrast methods in LEEM

Diffraction Contrast

Diffraction contrast is the most frequently used contrast method in LEEM. The backscattering intensities and their energy dependence may vary considerably depending on differences in structure and crystal orientation, formation of ordered adsorbate structures, etc. Therefore, they are unique fingerprints of the surface structure. As one can see from the example in figure 3.8, the different faces of the same crystal, tungsten, display different reflectivity at normal incidence.

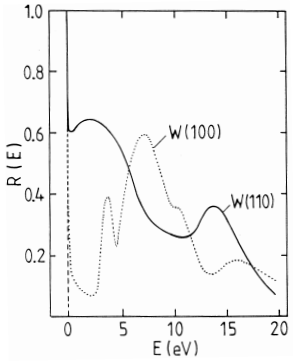

Figure 3.8: Comparison between the normal incidence reflectivity of W(110) and W(100) surfaces at low energies [97].

Bright-field and dark-field operation

LEEM images can be produced using either zero or higher order diffraction beams. The diffraction beams are selected by means of an aperture, which is inserted in the diffraction plane along the imaging column of the microscope. We talk about bright-field (BF) mode when the LEEM image is constructed using the zero-order diffraction beam. In dark-field (DF) LEEM higher or fractional order diffraction spots are used to image the surface. The dark-field mode allows a direct measurement of the lateral extent of a given surface phase.

A scheme of the operating principle of BF and DF operation is shown in figure 3.9. This a simplified illustration of the mechanism. In practice, one does not move the contrast aperture, but rather deflects the incoming electron beam until the chosen backscattered beam passes through the aperture [95].

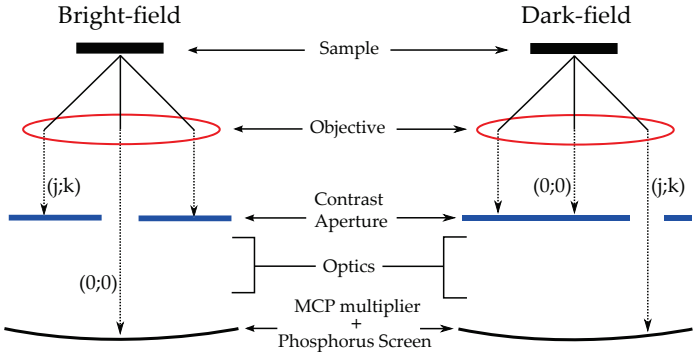

Figure 3.9: Simplified scheme of brightfield/darkfield operation mode.

3.5 Molecular Orbital Tomography

3.5.1 The plane wave approximation

It is well-known that, upon adsorption on a metal substrate, the electronic structure of an organic layer is affected by the interaction with the surface, resulting in changes of the energy position of the frontier molecular orbitals. These changes are often studied by ultraviolet photoelectron spectroscopy [98, 16, 71] or by scanning tunneling spectroscopy [47, 99]. However such approaches sometimes might be inconclusive. Therefore, a complementary technique providing access to the molecular electronic states is desirable. Angle-resolved photoelectron spectroscopy is a well-established method to study the band structure of solids (see also 3.1) and recently it has been shown that it can also provide an alternative route to obtain information regarding the charge distribution of individual molecular orbitals [20, 21]. Under specific assumptions about the final state of the photoemitted electron, molecular orbital structures can be investigated using data from the angle-resolved photoemission. This approach, based on the comparison between ARPES measurements and theoretical calculations, forms the basis of molecular orbital tomography (MOT).

The photoemission current (I) within the dipole approximation is proportional to:

$$I(\theta, \phi, E_{kin}) \propto \sum_i |\, \langle \psi_f(\theta, \phi, E_{kin}) | \mathbf{A} \cdot \mathbf{k} | \psi_i \rangle \,|^2 \times \delta(E_i + \Phi + E_{kin} - h\nu) \tag{3.13}$$

where θ and ϕ are the polar and azimuthal emission angles, respectively. I is given by the sum over all transitions from the the occupied initial states ψ_i to the final states ψ_f characterized by the direction (θ, ϕ) and the kinetic energy of the photoemitted electron. The final state, in the most simple approach, can be approximated by a plane wave (PW) only characterized by the direction and wave number of the emitted electron [20]. This ansatz simplifies the evaluation of equation 3.13: the photocurrent (I_i), arising from one particular initial state i, can be found from

the Fourier transform (FT) $\widetilde{\psi}_i(\mathbf{k})$ of the initial-state wave function corrected by the polarization factor $\mathbf{A} \cdot \mathbf{k}$:

$$|\widetilde{\psi}_i(\mathbf{k})| \propto \frac{\sqrt{I_i(\theta, \phi)}}{|\mathbf{A} \cdot \mathbf{k}|} \tag{3.14}$$

For organic molecules, the photocurrent of a well-defined initial state can be selectively measured, when the energetic separation of individual molecular orbitals is bigger than the intermolecular band dispersion. Equation 3.14 allows the measurement of $|\widetilde{\psi}_f(\mathbf{k})|$ and, via a subsequent inverse FT, the reconstruction of molecular orbital densities in real space, providing a new tool for the investigation of organic molecular films on metallic substrates. In case of molecules, the plane-wave approximation for the final state is valid under the following conditions [20]:

1. Electron emission from π orbital of large planar molecules.

2. An experimental geometry in which the angle between the polarization vector **A** and the direction of the emitted electron **k** is rather small.

3. Molecules consisting of many light atoms, *e.g.* H, C, N and O.

There is also another important experimental requirement: the organic film should be long-range ordered to avoid an increasing of background in ARPES patterns. If molecules are randomly oriented, their contribution to the ARPES maps do not sum coherently, giving rise to such background.

Equation 3.14 relates the absolute value of the molecular orbital FT to the photoemission current, losing information about the phase. This complicates the retrieval of the real space MO. However, through an iterative procedure, a real space image of molecular orbitals (also with the phase) in two and three dimensions can be reconstructed from the photoemission data [100, 101].

3.5.2 A practical example

The viability of the plane-wave final-state approximation, in conjunction with initial-state orbitals taken from density-functional, has been shown in several examples [20, 22, 23, 24]. As an example of MOT applications, we present the multilayer pentacene, deposited p(2x1) oxygen reconstructed Cu(110) surface [20]. The first step is to calculate the electronic structure of an isolated pentacene molecule using DFT, the resulting HOMO orbital is presented in figure 3.10a. Then, its corresponding three-dimensional FT (3D-FT) has been performed (see figure 3.10b). Finally, a 2D cut of the 3D-FT (indicated in red) must be evaluated on a hemisphere of radius $k = \sqrt{(2m/\hbar^2) \cdot E_{kin}}$ and it is shown in figure 3.10c.

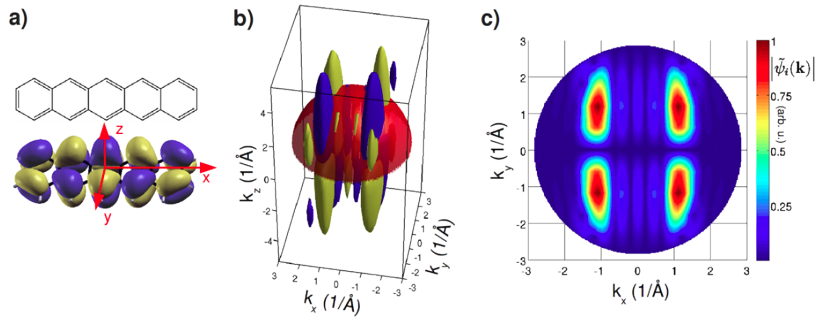

Figure 3.10: (a) Chemical structure of pentacene and its HOMO calculated from DFT. (b) 3D FT of the pentacene HOMO orbital, yellow (blue) showing an isosurface of a constant positive (negative) value. The red hemisphere, with $|\mathbf{k}|$ radius, illustrates a cut of the 3D FT taken at constant kinetic energy. (c) Absolute value of the pentacene HOMO Fourier transform on the hemisphere indicated in panel (b). Reproduced from [102].

Before directly comparing the so obtained 2D FT to the ARPES map, the geometric arrangement of pentacene must to be taken into account. The molecules adsorb with their long axis parallel to the surface, but the π orbitals are tilted out from the normal surface plane (β) by 26°. Due to the two-fold symmetry of the substrate, the contribution of two domains ($\beta = \pm 26°$), in the final simulated FT, is expected for the multilayer film, and the resulting image is shown in figure 3.11a. Figure 3.11b also shows an experimental ARPES pattern, taken at the HOMO energy of a pentacene multilayer. The agreement between the simulated momentum map (fig. 3.11a) and the measurement (fig. 3.11b) is very satisfying. Within MOT, the contribution of multiple ordered molecular domains to the angle-resolved photoemission intensity can be disentangled. Clearly, this approach not only describes well the PE intensity, but also provides a tool for determining the molecular orientations.

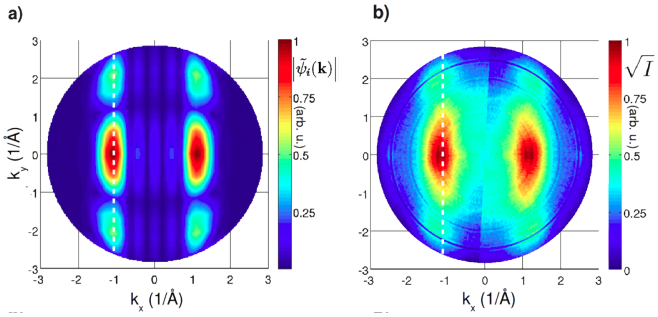

Figure 3.11: (a) Simulated FT for penatacene which takes into account the contribution from the two tilted domains ($\beta = \pm 26°$). (b) Experimental photoemission intensity at a constant binding energy corresponding to the pentacene HOMO from the multilayer of pentacene. Reproduced from [102].

MOT has been proved itself to be extremely useful also for identifying molecular states of adsorbed molecules on metallic surfaces beyond a simple comparison of energy-distribution

curves measured in photoemission experiment with the calculated orbital energies. The example reported here regards *p*-sexiphenyl adsorbed on the Cu(110) [20]. Upon adsorption, two new features appear in the low–binding energy region of the valence band spectrum, one centered at 0.3 eV below E_F, and the other at a binding energy of 1.9 eV, close to Cu *sp* and *d* band intersection. Momentum maps, taken at these two binding energies (fig. 3.12a and fig. 3.12c, respectively), agree well with the calculated FTs of the HOMO and LUMO from an isolated sexiphenyl (fig. 3.12b and fig. 3.12d, respectively). These findings prove that the molecular feature observed at a BE of 1.9 eV can be attributed to the sexiphenyl HOMO and, moreover, that its character is preserved even in a strongly interacting monolayer on a metal surface. The peak at 0.3 eV, assigned to the gas-phase sexiphenyl LUMO, indicates electron charge transfer from the substrate to the molecular layer.

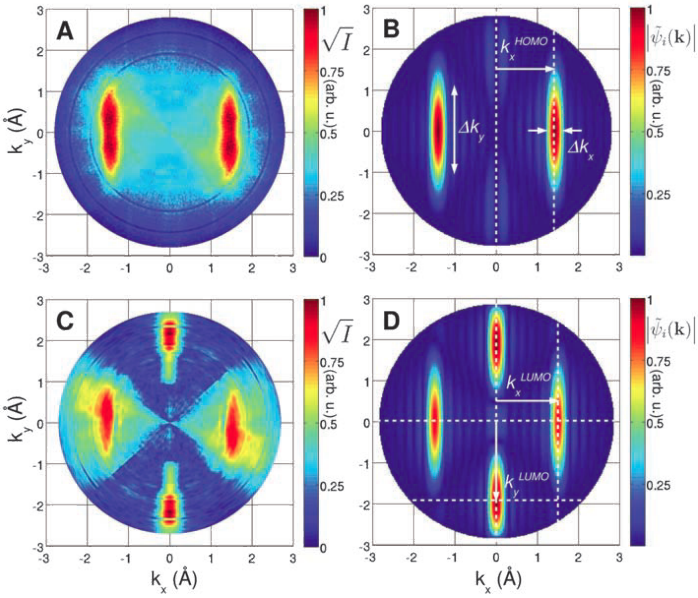

Figure 3.12: Measured PE intensities compared to calculated FTs. (a) PE momentum map (square root of the intensity) from a monolayer of sexiphenyl on Cu(110) at a binding energy of 1.9 eV, which corresponds to the sexiphenyl HOMO. (b) Absolute value of the FT of the sexiphenyl HOMO calculated for an isolated molecule within DFT. (c) Same as in (a) but for a binding energy of 0.3 eV. (d) Same as in (b) but for the sexiphenyl LUMO. Characteristic features in the computed FTs are indicated by the white arrows, as described in the text. Reproduced from [20].

Using this tomographic method, contributions from different molecular orbitals to the angle-resolved valence band spectrum can be deconvoluted. In this way, an orbital-by-orbital characterization of large adsorbate systems can be carried out without need of sophisticate photoemission theory. In the PTCDA/Ag(110) system, the contributions of 6 different molecular orbitals have been disentangled from the ARPES maps within an energy window of $\sim$ 4 eV [23].

3.6 Scanning Tunneling Microscopy

Scanning tunneling microscopy (STM) is an experimental technique developed in the eighties which lead to revolutionary developments in surface science. STM is one of the few microscopy techniques which can reach atomic length scales: lateral and vertical resolution are respectively ~ 1 Å and ~ 0.01 Å, which gives the possibility to resolve single atoms and molecules on the surface, though without direct chemical sensitivity. STM does not require ultra-high vacuum conditions, but it can be also performed in air and at low or high temperature. In most cases it is not intrusive; the system is not modified by the measure as could happen with other techniques.

The interaction with the surface, which has a local character, provides information on the atomic scale only from the top surface layer. This capability is used to study adsorbates, defects and surface reconstructions; along with dynamic phenomena at surfaces as some instruments di allow fast acquisition.

3.6.1 Working principle

STM measurements involve two electrodes: one is the sample and the other is a tip. The tip approaches towards the sample until tunneling conditions are established. The space between the two electrodes creates a potential barrier, which does not allow the flow of electrons from one side to the other according to classical mechanics. However, quantum mechanics allow a non-zero probability that an an electron can tunnel through a potential barrier, resulting in a measurable current. The height of the potential barrier depends on the work function of the two electrodes, and thus of the materials of which the tip and sample are made. Instead, the width is related to the distance between the two electrodes. The STM tip is typically made of tungsten or platinum-iridium. In the simplest approximation, the tip-sample potential barrier can be assumed to be one-dimensional, with a rectangular profile, as represented in the scheme in figure 3.13.

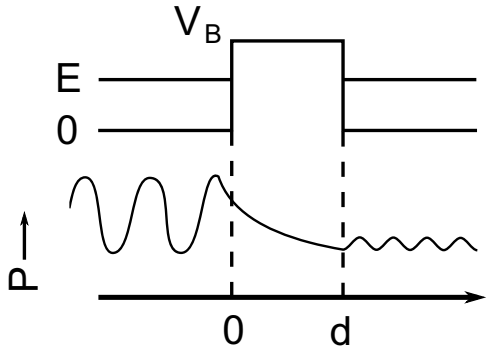

Figure 3.13: Simple scheme of rectangular potential barrier of V_B height. P is the probability density to overcome the barrier.

The decay of the wave function inside the 1-D potential barrier is exponential:

$$\phi(z) = \phi(0)e^{-kz} \tag{3.15}$$

where z is the spatial coordinate and k is the wavevector described by the relation:

$$k^2 = \frac{2m \cdot (\mathrm{V_B} - \mathrm{E})}{\hbar^2} \tag{3.16}$$

where m is the electron mass, $\hbar$ the Planck's constant, $\mathrm{V_B}$ the energy of the potential barrier and E the electron energy in the electrode. $\mathrm{V_B} - \mathrm{E}$ is the energy needed to extract an electron from the level E. The term $|\phi(z)^2|$ is the probability density to find an electron at distance z. The exponential term describing the barrier (e^{-2kz}) implies that there is a non-zero probability to overcome the barrier. Higher energy states, in accord to eq. 3.16, have higher tunneling probability.

If the Fermi levels of the two electrodes are different, a net charge transfer takes place to align them, but it is not possible to have a current flow unless a potential difference is applied between the two electrodes. When applying an electrostatic potential V between the two metals, an electron flow occurs from the filled states of the anode to the empty states of the cathode in the energy range from $\mathrm{E_F}$ to $\mathrm{E_F} - \mathrm{eV}$. If a negative bias is applied to the tip, the current flows from the sample to the tip, probing the filled states of the sample; conversely, in the case of a positive bias, the current flows in the opposite direction, probing in this case the empty states of the sample (see figure 3.14).

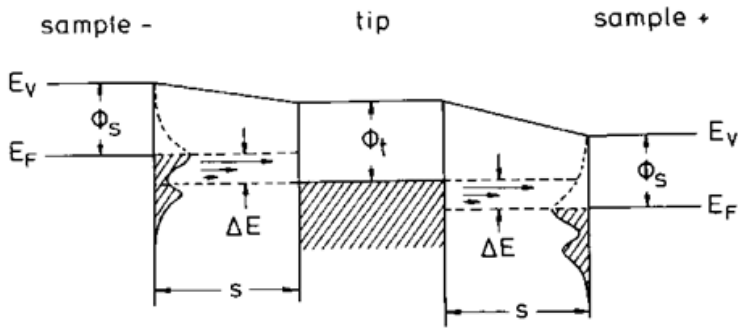

Figure 3.14: Schematic diagram of the tunneling between metallic tip and the surface. On the left, the case of a negative biased sample with respect to the tip. On the right we have the opposite situation: the bias applied to the sample is positive. Reproduced from [103].

The tunneling current is due to the integrated contribution of the states in the energy range from $\mathrm{E_F}$ to $\mathrm{E_F} - \mathrm{eV}$ and from $\mathrm{E_F}$ to $\mathrm{E_F} + \mathrm{eV}$, for the cases of positive and negative bias, respectively, which are involved in the tunneling process. In accordance to the Tersoff-Hamann model (spherical

tip with *s*-type wave functions), for small bias voltage the tunneling current can be expressed in terms of the local DOS of the sample, $\rho_S(z; E_F)$, at the tip position, near the Fermi level.

$$I = eV \cdot \rho_S(z; E_F) \tag{3.17}$$

Furthermore the tunneling current decays exponentially, *i.e.* the current amplitude decreases by one order of magnitude for displacements of 1 Å. The tunneling condition is therefore established only for very small distances between the two electrodes. Measuring these currents requires very precise and sensible instrumentation; furthermore special precautions have to be used to avoid vibrations. In practice, the tip is raster scanned across the surface using a feedback system, which keeps the tunneling current constant while varying the height of the tip from the sample. To achieve movements of the order of few 10^{-2} Å piezoelectric actuators are used. These materials change their shape when a potential difference is applied at their ends. Piezoelectric actuators are also used to raster the surface in the (x,y) directions. In this way, we can obtain spatial maps representing the constant DOS at the Fermi level, which, in a first approximation, corresponds to the surface morphology. Due to the finite size of the tip, the topography resolution is also finite. Working with very sharp tips, ideally with only one atom at the end, is essential to achieve the best resolution [104, 105, 103].

3.6.2 Experimental apparatus

The STM measurements were carried out in the STM laboratory of the Surface Structure and Reactivity group at the IOM-CNR TASC-laboratory in Trieste. The experimental system is composed by two UHV chambers, one for the sample preparation and the other accommodating an Omicron Low Temperature STM (LT-STM). The mechanical stability of the tip-sample junction is provided by means of three springs, which suspend the STM head below the cryostat. The operating temperature range of the LT-STM is ideally between 2.5 K and room temperature (RT). To reach temperatures below RT a cooling system made up of two concentric cylindrical cryostats is used (the STM head is fixed below them). These have to be filled with cryogenic liquids: liquid nitrogen (LN_2: boiling point at 77 K) and liquid helium (LHe: boiling point at 4.2 K). The external cryostat is always filled with LN_2, while the inner cryostat can be filled with LN_2 or LHe according to the desired temperature. All the intermediate temperatures can be reached by means of a resistive heater located near the sample stage and powered by a PID temperature controller. The temperature is measured by means of a silicon diode installed behind the sample stage. If no counter-heating is applied, the STM can be kept at 4 K for 24 hours before having to refill the inner cryostat. To reach temperatures as low as 4 K at the sample, the STM head is surrounded by a double shielding mechanism, in order to prevent external electromagnetic radiation from limiting the cooling power. The low temperature range of operation makes the LT-STM suitable to study molecular adsorbates.

Chapter 4

Experimental details

4.1 Sample preparation and methods

All the sample crystal surfaces used in this work, namely Cu(100), Cu(110) and Ag(110), were prepared by cycles of Ar^+ ion sputtering at 2.0 keV, followed by annealing at 800 K. The surface order and cleanliness were monitored by low energy electron diffraction (LEED), Auger or photoelectron spectroscopy. Sample cleaning and the organic film deposition were done in the same way in all experiments. Conversely, the molecular coverage was determined with different methods, which will be specified each time, depending on the experimental set-up used. A few milligrams of NiTPP (or CoTPP), commercially available from Porphyrin Systems, were loaded into a quartz crucible of a home-made Knudsen cell evaporator connected to a separate preparation chamber. Prior to the experiments, the molecule powder was thoroughly degassed at 480 K for several hours. The molecules were thermally evaporated, under UHV conditions (pressure $< 5 \cdot 10^{-10}$ mbar) at 520 K onto the metal substrate kept at room temperature (RT). For the measurements performed at the NanoESCA beamline the porphyrin (CoTPP and NiTPP) layer growth was optimized using LEED. Close to the 1 ML regime, sharp LEED patterns were observed, while additional deposition on an already saturated surface broadens the diffraction spots. At the ALOISA beamline, instead, the NiTPP evaporation rate was calibrated by means of a quartz micro-balance. The molecular film quality was then also checked by XPS. In the STM experiments, the NiTPP coverage was determined directly from the STM images, comparing the bare copper area to the NiTPP covered surface.

All the μ-ARPES experiments were carried out at the NanoESCA beamline, with a nominal photon energy of 27 eV. Time-dependent photoemission measurements of the valence band showed that the adsorbed molecular layers were sensitive to the NanoESCA micro-focused beam ($\sim 100\ \mu m^2$ at the sample surface, photon flux: $3 \cdot 10^{12}\ ph/s$). For this reason, the sample was continuously rastered with a speed of $\sim 1.5\ \mu m/s$ during the data acquisition, in order to minimize radiation damage.

Additional NEXAFS and XPS measurements were performed at the ALOISA beamline. This

beamline provides a larger photon beam spot ($30 \times 200\ \mu m^2$ at the sample surface, photon flux: $5 \cdot 10^{10}\ ph/s$), which damages the molecular film only slightly. No changes were observed on the valence band and core level spectra, after 1 hour of X-ray irradiation. Thus, we concluded that porphyrin films were reasonably stable under our experimental conditions. The XPS spectra were measured using a photon energy of 515 eV for C 1*s* and N 1*s* core levels, 650 eV for O 1*s* and 1000 eV for Ni 2*p*. NEXAFS data were acquired in partial electron yield mode with a cutoff of the secondary electrons at 240 eV and 370 eV for the C 1*s* and N 1*s* threshold, respectively. The overall resolution of XPS and NEXAFS spectra was 0.3 eV and 0.2 eV, respectively. The measurements were performed in the end-station with a base pressure of $5 \cdot 10^{-11}$ mbar at NanoESCA and $1 \cdot 10^{-10}$ mbar at ALOISA, in a temperature range varying from 140 K to room temperature (RT).

The structural characterization of the organic/metal interface, at the *meso*-scale, along with the quantification of the damage upon electron beam irradiation, was performed in the SPELEEM set-up, installed at the Nanospectroscopy beamline of the Elettra synchrotron. Molecules were evaporated onto the copper surface in a separate chamber (base pressure $p = 1 \cdot 10^{-9}$ mbar), the sample was then transferred into the LEEM chamber (base pressure of $1 \cdot 10^{-10}$ mbar) to be measured. All the experiments were done at RT.

Low temperature STM measurements were carried out at a temperature of approximately 77 K, unless otherwise stated. The STM microscope is hosted in an ultra-high vacuum (UHV) chamber, operating at a base pressure of about $1 \cdot 10^{-10}$ mbar. Images were acquired in constant current mode, with the bias voltage applied to the sample, and the tip at ground. Electrochemically etched tungsten tips were used for imaging. Simulated images have been obtained within the Tersoff-Hamann approximation based on the optimized adsorption structure of NiTPP on Cu(100). STM images were processed by subtracting a background plane to correct the sample tilt. The applied enhancements consist of B-spline resampling, to increase the sample count, and mild Gaussian filtering, to remove high frequency noise components [106].

4.2 Sample characterization

Immediately after the cleaning procedure, the crystal structure was checked by LEED. Figure 4.1a shows, as an example, the LEED pattern obtained after one cleaning cycle for the Cu(100) surface. The square pattern corresponds to the (100) surface orientation of the FCC crystal. The spot sharpness, absence of diffuse background and/or extra fractional spots, are indicators of the surface cleanliness. After the NiTPP deposition, the LEED pattern shows additional spots, clearly visible in figure 4.1b. These sharp spots are indeed related to the formation of a well-ordered molecular overlayer, close to the 1 ML regime. The resulting structure will be discussed extensively in the next chapter. The present LEED pattern is very reproducible and no other phases are observed for varying the molecular coverages. The NiTPP second layer growth has two effects: it smears the molecular-related LEED pattern and attenuates the intensity of the first order Cu(100) diffraction spots. This indicates, that the molecules in the second layer do not form a well-ordered

lattice. No LEED was observed for the multilayer regime. The presence of a long-range ordered molecular film, close to 1 ML coverage, makes this system suitable to be investigated by the MOT technique.

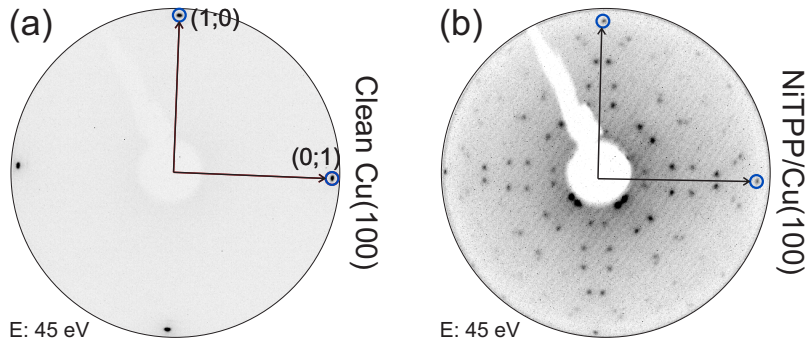

Figure 4.1: (a) Cu(100) LEED pattern at E = 45 eV, taken immediately after annealing at 800 K. The first oder diffraction spots are circled and pointed by the reciprocal unit cell vectors. (b) LEED pattern taken after deposition of NiTPP molecules on Cu(100), E = 45 eV. Extra spots appear now and are related to the long-range ordered structure formed by the molecules upon adsorption.

In addition to the LEED measurements discussed above, the substrate cleanliness and the molecular layer growth were further checked using XPS and Auger electron spectroscopy. In the example shown in figure 4.2a, we report the wide range XPS spectra taken before and after NiTPP deposition on Cu(100). The main emission lines are labeled in the figure. After sample cleaning, the amount of carbon and other impurities present on the surface were found to be below the apparatus sensitivity (<0.5%). Upon NiTPP deposition, two new peaks, assigned to the N 1*s* and C 1*s* core levels, appear at higher BE*s*. A detailed analysis of these two peaks will be presented in the following. The Auger spectra, displayed in figure 4.2b, basically confirm the analysis of the XPS data. The five components at higher electron kinetic energy are ascribed to the the copper *LMM* Augers lines. Another component at 273 eV appears only after NiTPP adsorption, and it is related to the C *KLL* transition. The absence of the O *KLL* lines in the [480-510] eV range, in both spectra, indicates that eventual O impurities are below the Auger sensitivity.

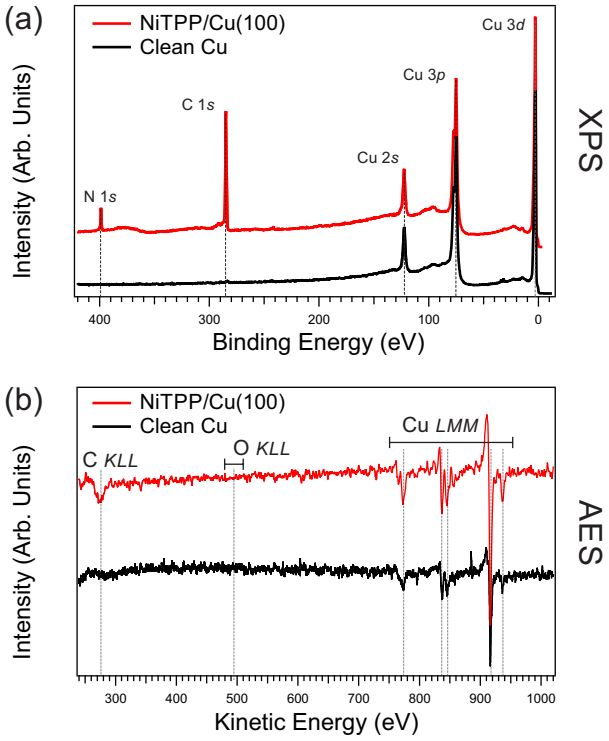

Figure 4.2: (a) XPS wide range spectra in normal emission geometry from clean Cu (black curve) and after the NiTPP deposition (red curve). $h\nu = 630$ eV. (b) Auger spectra from clean Cu (black curve) and after the NiTPP deposition (red curve).

The sublimation temperature should be carefully selected for organic molecules, as at too high temperatures the organic compound may thermally decompose already in the crucible. Therefore, we performed the quantitative analysis of the core level spectra and checked the stoichiometry of the deposited molecules. The high resolution N 1*s* and C 1*s* spectra, measured in normal emission geometry, are shown in figure 4.3a and 4.3b, respectively. The binding energy scales are referred to the copper E_F.

The fitting of the N 1*s* core level with a Doniach-Sunjic lineshape, shows that the N 1*s* line (fig. 4.3b) has only one component at BE = 398.57 eV. The presence of a single peak in the spectrum suggests that all four nitrogen atoms of the deposited molecules are chemically equivalent, proving that the porphyrin is indeed metalated [36]. The peak BE is in good agreement with the one observed in other MTPPs [107, 37]. Based on this analysis, we can exclude non-metalated porphyrin impurities, which might be present in the loaded organic powder. In this case, two non-equivalent nitrogen species (iminic and pyrrolic) would contribute to the N 1*s* spectrum with two distinct peaks separated by 2 eV [107, 37].

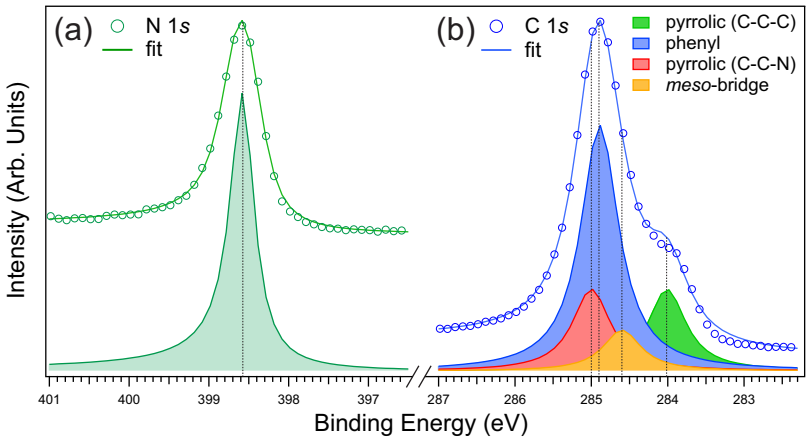

Figure 4.3: Photoemission spectra of N 1*s* (a) and C 1*s* (b) core levels (experimental data and fits) of self-assembly NiTPP arrays on Cu(100). Both spectra are acquired in normal emission geometry, at photon energy of 515 eV.

Instead, the large full-width at half-maximum (FWHM) of the C 1*s* core level (> 0.8 eV), fig. 4.3b, together with the pronounced shoulder at lower binding energy, suggest the presence of several components. Within the NiTPP structure (see also figure 2.1c), we note that there are 20 carbon atoms belonging to the macrocycle plus 24 located in the phenyl rings. Moreover, the latter contain three inequivalent types of carbon atoms: *meso*-carbon bridges (4 atoms), C−C−C pyrrolic (8 atoms) and C−C−N pyrrolic (8 atoms). The spectrum can be reasonably well fitted using a Voigt lineshape, with four components having the same Lorentzian (0.6 eV) and Gaussian (0.3 eV) widths and fixed intensity ratios 24:8:8:4. The four peaks are superimposed to the measured C 1*s* spectrum in figure 4.3a, and their BEs are listed in table 4.1.

Table 4.1: Binding energies of the four components contributing to the C 1*s* core level spectrum.

	C−C−N pyrrolic	**Phenyl**	***meso*-carbon bridge**	**C−C−C pyrrolic**
BE (eV)	285.01 eV	284.89	284.62	284.01

The chemical shift of the two pyrrolic components (∼1 eV) is in good agreement with the one measured for pyrrole molecules in the gas-phase [108]. Considering the whole tetraphenyl porphyrin C 1*s*, we can compare the present results to a ZnTPP multilayer deposited on Si(111) [109]. While phenyl and C-C-N peaks have similar BEs to those reported for ZnTPP multilayer, the other two exchanged their energetic order: the C-C-C pyrrolic has the lowest BE, followed by the *meso*-carbon bridge. This change in energy position can be explained by the different local environment experienced by these carbon species in case of the ZnTPP multilayer and NiTPP/Cu(100). In the latter, as will be shown in the following, the macrocycle sits very close to the copper surface modifying strongly the electronic structure of the entire molecule.

Chapter 5

Organic semiconductors on transition metals: NiTPP/Cu(100)

5.1 Introduction

In this chapter, we develop a consistent picture of the adsorption geometry and electronic properties of the tetraphenyl porphyrin (NiTPP) adsorbed on the Cu(100) surface, combining different state-of-the-art experimental techniques supported by density functional theory calculations. The chapter consists of parts that appeared in Zamborlini, G. *et al.*, *Nature Communications*, accepted (2017) [110].

We unequivocally determine the electronic occupancy of the molecular frontier orbitals, *i.e.* HOMOs and LUMOs, by means of molecular orbital tomography (MOT). Our findings indicate an unexpectedly high electron charge transfer from the Cu(100) surface to the macrocycle of the NiTPP molecules, involving even the gas-phase LUMO+3 of NiTPP. By comparing STM and DFT-simulated images, we demonstrate that the topography contrast arises mainly from the electronic states of the porphyrin phenyl rings, which are strongly tilted upwards. This molecular configuration allows the macrocycle to get close to the copper surface, while preventing the frontier orbitals, spatially located on this moiety, to be probed by STM.

5.2 Geometric structure

5.2.1 Characterization of the highly oriented NiTPP self-assembly

In order to identify NiTPP on the close-packed structure on Cu(100), we first focus on the appearance of a single molecule in STM. Figure 5.1 shows the STM image of an isolated molecule. In the image, the four symmetric bright lobes are associated to the four phenyl terminations and the central depression to the macrocycle, with the metal in the center (see the superimposed chemical structure in fig. 5.1). This interpretation agrees with the assignments made for CoTPP molecules

on Cu(110) [48], where the cobalt porphyrins exhibit a similar STM contrast. Unfortunately, the orientation of the phenyl plane with respect to the substrate (θ angle, introduced in figure 2.4) cannot be directly evaluated from STM images. The symmetric appearance of the four lobes suggests $\theta = 90°$, because, as already discussed in section 2.2.1, $\theta = 0°$is not energetically favored.

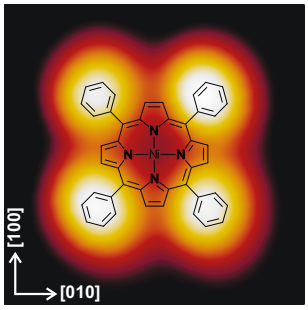

Figure 5.1: STM image of a single isolated NiTPP on Cu(100). STM image parameters: V_b = -0.2 V, I_t = 0.2 nA, 2x2 nm^2

Because of the different tunneling conditions, the atomic resolution was not achieved at the same time on both NiTPP islands and the free copper substrate. For this reason the clean (100) copper surface was measured separately. The STM image of the bare substrate allows one to construct a grid matching the copper lattice. This grid, properly scaled by the field of view, can be superimposed to the NiTPP/Cu(100) STM images, making it possible to determine the orientation of single molecules and the unit cell of the NiTPP self-assembly. This procedure does not allow one to find experimentally the molecular adsorption site, because the grid cannot be anchored to the substrate while measuring the NiTPP lattice. An isolated NiTPP molecule is oriented along the [001] direction of Cu(100), *i.e.* with the N-Ni-N axes parallel to the [001] and [010] directions, respectively.

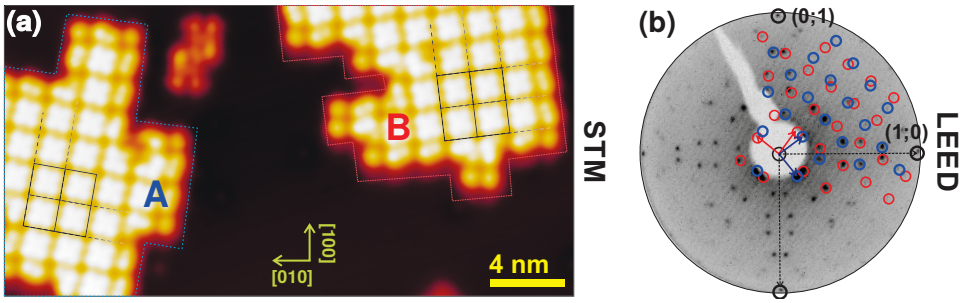

Figure 5.2: (a) STM image including A and B NiTPP domains. The STM image parameters: V_b = -1.5 V, I_t = 0.2 nA, image size 15x20 nm^2, measured at 4.3 K. (b) LEED pattern of NiTPP/Cu(100) acquired at E_K = 45 eV. The simulated structure is superimposed: blue and red spots correspond to A and B domains, respectively.

At coverages higher than $\sim$ 0.3 ML, we observe that the molecules tend to assemble into

compact islands. STM images reveal the presence of two rotational domains (labeled A and B in figure 5.2a). These domains are mirrored with respect to the [001] direction. Only these two are observed, as a consequence of the four-fold symmetry of both substrate and NiTPP. They are both commensurate with the copper lattice, and their square unit cells can be described by the following epitaxial matrices:

$$A = \begin{bmatrix} 4 & 3 \\ -3 & 4 \end{bmatrix} \qquad B = \begin{bmatrix} 3 & 4 \\ -4 & 3 \end{bmatrix}$$

The unit cell size is determined experimentally as the distance between two molecular centers ($\sim$ 1.27 nm). STM provides only local information on the NiTPP unit cell and domain orientation, LEED patterns, however, are averaged on a few mm^2 wide area. The LEED pattern of NiTPP/Cu(100) is shown in figure 5.2b. The first order diffraction spots related to the substrate are marked by black circles and indicated by the black arrows. The other spots appear only after NiTPP deposition and are related to an ordered superstructure formed by the close-packed molecules. Knowing the unit cell of a given supramolecular array, it is possible to simulate the resulting LEED pattern. The excellent agreement between the measured and simulated LEED patterns of the organic film (see fig. 5.2b), based on the matrices determined above, confirms the STM findings, also indicating the existence of long-range order across the surface. Furthermore, this well-defined LEED pattern can be used as a fingerprint to find and reproduce experimental conditions for the NiTPP deposition on Cu(100) on different experimental set-ups. By comparing the simulated and experimental LEED patterns, the diffraction spots are associated to the corresponding domain (see fig. 5.2, circled in red and blue, respectively). Additionally, uncommon features, having a different appearance with respect to the single and close-packed NiTPPs, are also observed in figure 5.2a. These features can be related to species/defects on the surface, such as chemically modified rectangular-NiTPP or H_2TPP, for example [111]. The quantitative analysis of the C 1*s* and N 1*s* core level spectra (shown in section 4.2), reveals that the peak intensity ratios well agree with the NiTPP stoichiometry and no additional features have been detected in the spectra. This suggests that the amount of these species/defects on the NiTPP layer is below the XPS sensitivity.

5.2.2 Adsorption geometry

In order to obtain further insight into the bonding and conformation of the adsorbed NiTPP molecule on Cu(100), the unit cell determined above was used to carry out periodic DFT calculations of the system using the VASP code [112, 113]. A repeated slab approach was employed, where the metallic substrate was modeled by four copper layers, and a vacuum layer of $\approx$ 15 Å was added between the slabs. To avoid spurious electrical fields, a dipole layer was inserted in the vacuum region [114]. Two types of approximations for exchange-correlation effects have been used: the general gradient approximation (GGA) [115] for the geometry optimization and the

HSE functional [116] for a subsequent calculation of the electronic structure. A Monkhorst-Pack $3 \times 3 \times 1$ grid of k-points [117] and the projector augmented wave [118] approach were used, allowing a relatively low kinetic energy cut-off of about 500 eV. The super cell geometry has been constructed according to the experimental LEED structure shown in figure 5.2b. During the geometry optimization, the atomic positions of the molecular layer and the first metallic layer were allowed to relax. In order to account for van-der-Waals interactions, the vdW-surf method according to Ruiz *et al.* [119, 120] was employed during the geometry optimization. All the simulations presented in this thesis have been performed by Dr. Daniel Lüftner and Prof. Peter Puschnig, at University of Graz, Austria.

For each of the three adsorption sites considered, where the central Ni atom is either at a top, bridge, or hollow site of the Cu(100) surface, the geometry has been optimized using the vdW-surf method [119, 120], to account for the van-der-Waals interactions. The hollow site was found to be energetically more favorable compared to the bridge and on-top sites by 1 and 2 eV, respectively. The reason for these significant differences lies in the fact that, in the relaxed structure of the hollow site, the macrocycle can move very close to the surface (about 2.0 Å), maximizing the interaction with the Cu substrate. This has a significant impact on the molecular adsorption geometry. As already found by Donovan *et al.* [48] by means of combined STM experiments and DFT calculations for CoTPP on Cu(110), the strength of the substrate-macrocycle bond has two important effects: first, the macrocycle remains almost planar in order to maximize the contact area with the substrate, and second, significant tilt and twist deformations are induced in two distinct pairs of diametrically opposite phenyls.

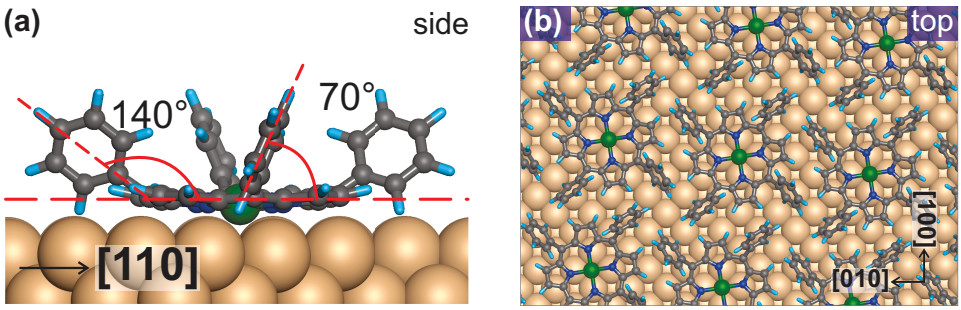

Figure 5.3: Proposed adsorption model for NiTPP/Cu(100). (a) side view. (b) top view.

The result of DFT calculations is shown in figure 5.3. The simulations reveal geometrical trends similar to those observed in the case of CoTPP on Cu(110) [48], even though in our case the geometrical distortions are slightly more pronounced. As in ref. [48], the molecule ends up very close to the surface, with the macrocycle just slightly corrugated, but with the phenyl rings pointing away from the surface under a tilt angle ϕ of about 140°, and a twist angle θ of approximately 70° (see figure 5.3a). As already analyzed in detail in the literature [48], the distortion of the molecule costs energy, which is compensated by the energy gained through the

interaction with the substrate. This geometry has a strong impact on the electronic structure at the interface, as it will be discussed in the next section. It is also worth mentioning that during the procedure for the geometry relaxation, two local energy minima were found for each adsorption site: one where the macrocycle is located about 4 Å above the surface and the other, significantly lower in energy, with the macrocycle much closer to the surface (2 Å). In the former minimum, the phenyl rings remain almost gas-phase-like ($\phi = 180°$, $\theta = 68°$), whereas in the latter they are strongly tilted and twisted, as described above. In the optimized structure, NiTPPs rotate by 8° with respect to the [001] direction, *i.e.* the N-Ni-N axes is 8° off with respect to the [001] and [010] directions (see figure 5.3b).

From the high resolution STM image of the self-assembled NiTPP, presented in figure 5.4a, we note that the four lobes (already assigned to the phenyl ligands) appear now asymmetric, revealing a chiral character. The chirality arises from the twisting of the phenyls as predicted by the DFT and confirms that phenyls are no longer perpendicular to the surface, like for the isolated molecule (see figure 5.1). It has to be noted that the orientation of the NiTPP with respect to the substrate can only be determined with a large uncertainty. In fact, no features related to the macrocycle are visible in the experimental images, and therefore a measurement of the azimuthal molecule-substrate angle can only rely on the protrusions related to the phenyl rings. The latter, however, appear somehow distorted due to their chiral character, making it difficult to correlate their orientation and mutual alignment with the orientation of the macrocycle. Taking into account all these sources of error, we can only state that the azimuthal molecule-substrate angle lies in the $[-6°, 10°]$ interval. For this reason, a complementary experimental technique, μ-ARPES, has been used to obtain this missing information and the result will be discussed below.

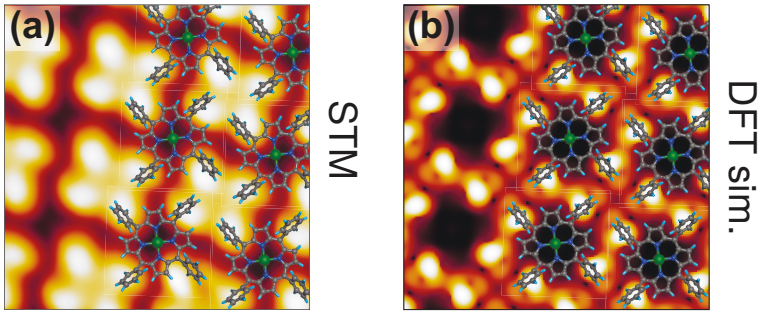

Figure 5.4: Comparison between STM measured and DFT simulated images. (a) Atomic resolution STM image on NiTPP/Cu(100) film. NiTPP molecule is superimposed. STM image parameters: V_b = +1.5 V, I_t = 0.5 nA, image size 3x3 nm^2. (b) DFT simulated STM image using the relaxed structure showed in Figure 5.3.

Starting from the optimized adsorption structure, the STM image has been simulated, and the result is shown in figure 5.4b. As already reported in Ref. [48] and Ref. [121], the four lobe appearance of NiTPP in the experimental STM images is associated with strongly tilted phenyl ring terminations while the central dark depression is associated to the macrocycle which

approaches very close to the substrate. The contrast, in both images, is vastly dominated by the features arising from the phenyl rings: due to their very large twist and tilt angles, they extend well above the plane of the macrocycle, preventing the macrocycle from being resolved by the STM tip.

Overall, the experimental and simulated STM images are in reasonable agreement. However, the simulated images unavoidably show many features that the STM tip cannot resolve experimentally, due to the broadening caused by the intrinsically large width and the electronic properties of the real tip apex (in the calculations, apex-copper surface distance $\sim 5.5 - 7.5$ Å). Therefore, the phenyls in the simulation appear slightly different from the experimental image. In accordance with the simulated images, the appearance of NiTPP in the STM images is almost bias independent within the [-2.0,+2.0] V range, as it will be shown in the next section.

The conformation of the highly oriented NiTPP film is also investigated by angle-dependent NEXAFS measurements. Probing the molecular unoccupied states, it is possible to obtain information on the phenyl ring twisting and the macrocycle saddling *via* the angular dependence of the π^* resonance intensities. As illustrated in section 1.1, the π^* states consist of p_z orbitals perpendicular to the aromatic structure plane. The intensity of these orbitals in the NEXAFS spectra, depends on the angle (Θ) between the electric field of the linearly polarized incoming light (**E**) and their spatial orientation. For an aromatic π^* system planarly adsorbed on the substrate, the corresponding NEXAFS resonances are enhanced when **E** is parallel to the orbital and almost vanish when perpendicular. σ resonances, *vice-versa*, show the opposite behaviour.

In the experimental geometry used, the synchrotron light illuminates the sample at grazing incidence (7° with respect to the surface plane), therefore linearly *p*-polarized light (*p*-pol) has its electric field oscillating almost perpendicular to the surface plane, while in the *s*-polarized light (*s*-pol) is parallel. According to the "building-block principle" [85], the NEXAFS spectrum of a molecule made up by various moieties, can be decomposed into the different contributions of each subgroup, as long as the corresponding orbitals are independent from each other. Thus, NEXAFS can be employed to qualitatively determine the orientation of each moiety with respect to the incoming synchrotron light.

The angle-dependent NEXAFS spectra taken at the carbon K-edge are shown in figure 5.5. We identified six features related to the $1s \rightarrow \pi^*$ transitions and two other associated to $1s \rightarrow \sigma^*$ [37, 122]. All the π^* resonances show a strong angle dependence: while A_C, C_C and D_C are stronger for *p*-pol and weaker (or almost vanished) for *s*-pol, B_C and E_C show the opposite trend.

A_C (283.9 eV) is assigned completely to the macrocycle, B_C ($\sim$285 eV), instead, mainly originates from the phenyl rings [37] plus a small contribution from the macrocycle. Therefore, the specific polarization-dependent behavior suggests that the NiTPP macrocycle is oriented almost parallel to the Cu(100) surface, while the phenyl groups are strongly tilted with respect to the surface plane. These experimental findings clearly support the proposed DFT adsorption model (see figure 5.3). This qualitative description of the adsorption geometry can be accompanied by a more rigorous analysis of the NEXAFS spectra. θ, *i.e.* the phenyl twist angle is calculated from the intensities of

π^* resonances, related to phenyls, for p-pol and s-pol spectra (I_p and I_s, respectively), using the following equation [123]:

$$\theta = \arcsin\sqrt{\frac{2\cos^2\alpha}{(I_p/I_s) + 3\cos^2\alpha - 1}} \tag{5.1}$$

where α is the incident angle of the synchrotron radiation on the sample (in the ALOISA setup, $\alpha = 7°$). In this expression the x-ray beam is assumed 100% linearly polarized. I_p and I_s are determined by the areas of the Voigt function used to fit the π^* resonances related to the phenyl rings. This analysis, carried out on B_C, leads to: $\theta = 68° \pm 5°$ which is in reasonable agreement with the DFT calculations of the adsorption structure.

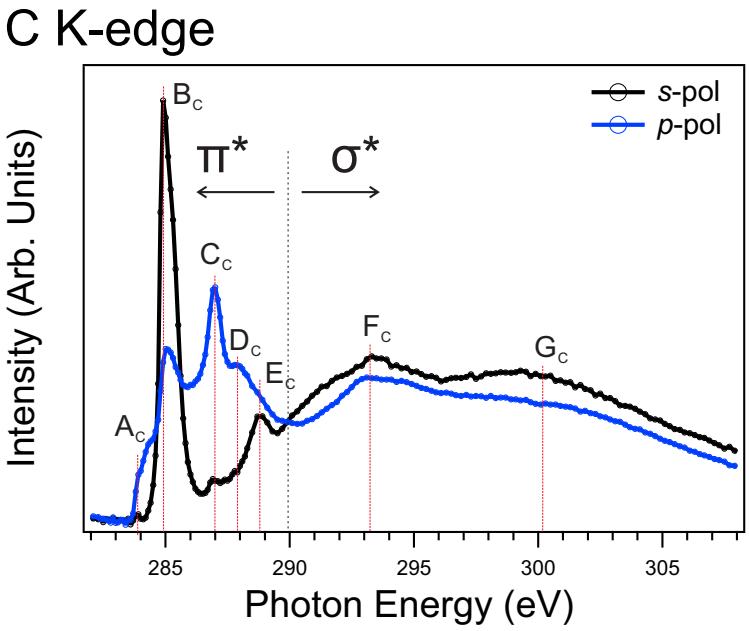

Figure 5.5: Carbon K-edge of NiTPP/Cu(100). The main peaks, related to specific transitions to unoccupied states are indicated by the dashed lines, and labeled in alphabetic order, starting from the pre-edge.

5.3 Electronic structure

5.3.1 Periodic DFT calculations

We now focus on the electronic structure of the NiTPP/Cu(100) interface where our main interest lies in the frontier orbitals localized at the porphyrin core. The density of states of the NiTPP/Cu(100) interface has been computed by means of DFT for the optimized adsorption geometry. The DOS was calculated using the HSE short-range hybrid functional [116] to account for the presence of both the delocalized π-orbitals of the macrocycle and the localized states at the

Ni atom. Note that using standard GGA functionals in the calculations would lead to an incorrect orbital ordering due to problems related to the self-interaction error [55, 19]. Figure 5.6 shows the corresponding DOS projected onto specific molecular orbitals (PDOS). We observe that the degenerate gas-phase LUMO/LUMO+1 (blue and light blue lines in figure 5.6a) are below the Fermi level, indicating that, upon adsorption, they become occupied. Surprisingly, the gas-phase LUMO+2 and LUMO+3 also have a non-zero contribution below E_F. These molecular levels are filled by charge transfer taking place from the substrate to the molecular film.

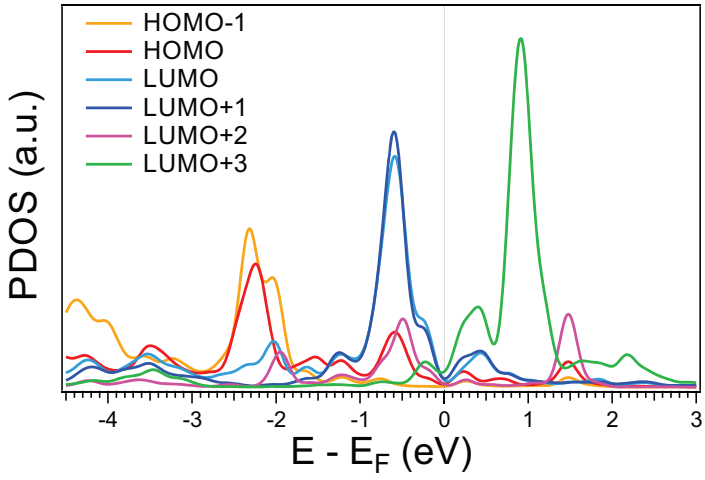

Figure 5.6: PDOS of adsorbed molecules onto molecular orbitals for the NiTPP/Cu(100) system.

It should be emphasized, however, that the occupancy of LUMO/LUMO+1 and the partial occupation of LUMO+2 and LUMO+3 does not express the net charge transfer. As is well-known from other systems [56], there is also a back-donation from the molecule to the substrate. We attribute the filling of formerly unoccupied MOs, *i.e.* the LUMOs, to the extremely short distance between the molecular backbone and the substrate. As a further consequence of this short distance, the charge spill-out at the surface is pushed into the metal (push-back effect) [124, 125, 22]. This push-back results in a dipole which substantially reduces the work function, thereby shifting the molecule's LUMOs below E_F. On the other hand, the charge transfer to the molecule creates a dipole of opposite sign. In accordance with the experimentally observed reduction of the work function upon the formation of the NiTPP layer, the DFT calculations suggest that for the overall interface dipole, the push-back effect dominates over charge transfer into the molecule.

In order to further analyze the work function changes upon adsorption of the molecular layer, we have calculated the plane averaged charge density differences $\Delta\rho$ as the difference between the charge density of the full system ρ_f and the sum of the charge densities of the two separate

systems, *i.e.* the freestanding molecular layer ρ_m and the substrate slab ρ_s:

$$\Delta\rho = \rho_f(r) - (\rho_m(r) + \rho_s(r)) \tag{5.2}$$

The corresponding results are shown in figure 5.7a. Here, red areas correspond to the regions of charge accumulation, while blue areas show regions of charge depletion. One can see, that a series of rather large dipoles appear upon adsorption in the z direction, along the surface normal.

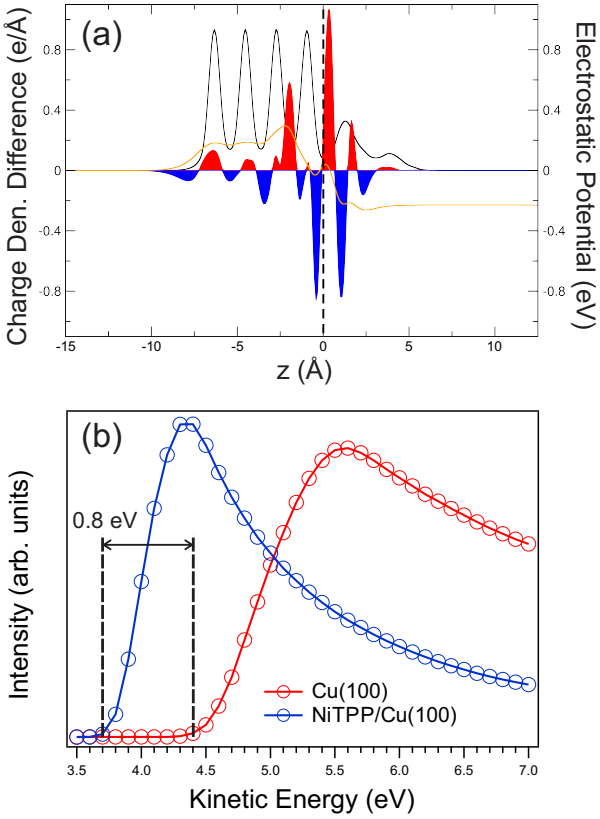

Figure 5.7: (a) Plane-averaged charge density difference (red-blue curve, left axis) and electrostatic potential (orange curve, right axis) as a function of the z direction, perpendicular to the substrate. In order to indicate the position of the metallic layers and the molecular layer, the plane averaged charge density of the full system is shown as a black line in arbitrary units. The copper surface is located at ~ 0 Å (dashed line) (b) Photoemission spectrum at the secondary electron onset for bare copper (red curve) and NiTPP/Cu(100) (blue curve), taken at $h\nu = 27$ eV.

The changes in the electrostatic potential, *i.e.* the change in work function, due to the push-back effect and charge transfer, can be calculated by solving the one dimensional Poisson equation for the charge density difference, integrating it twice along the z coordinate. The result is shown as

an orange line and emphasizes that in total the dipoles induced by the adsorption reduces the work function and hence that the push back effect dominates. The reduction of the work function takes place despite the rather large charge transfer to the molecule and can be understood due to the small distance between adsorbate and metallic substrate. Work function changes of the system, upon NiTPP adsorption, have been measured using our PEEM set-up. All changes were referred to the value for the clean copper work function. The work function difference between the bare Cu(100) and NiTPP/Cu(100) has been defined as the difference of the inflection point of the secondary photoelectron threshold for the two systems, as shown in figure 5.7b. The NiTPP, upon adsorption, lowers the work function of the overall system by $\sim$0.80 eV, which is in agreement with the DFT predictions.

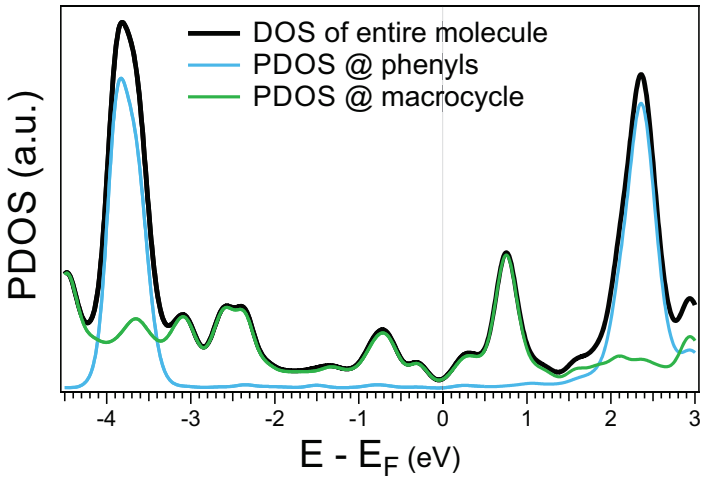

Figure 5.8: DOS of the entire molecule (Black curve), projected density of states (PDOS) onto the phenyl group (light blue curve) and on macrocycle (green curve).

Upon adsorption, the frontier orbitals, *i.e.* HOMOs and LUMOs close to the band gap, spread over a wide energy range, [-3.0,+1.5] eV (see figure 5.6a). In order to understand where these orbitals are localized over the molecule, in figure 5.8 the DOS projected onto the macrocycle (green curve) and the one projected onto the phenyls (light blue curve) have been compared. It has to be noted that, in this energy range, the PDOS of the phenyl rings has a rather featureless plateau, whereas the macrocycle PDOS is structured. We can conclude that the frontier orbitals are almost entirely located on the porphyrin macrocycle.

STM images taken at different bias voltage are shown in figure 5.9. The NiTPP appearance in the STM images does not noticeably change in the [-2.0,+1.0] V range, while the phenyl features start to blur when approaching the +2.0 V bias. This is in agreement with the simulated PDOS (see figure 5.8). Indeed, in the [-3.3,+2.0] eV range, the projected DOS on phenyl group has a rather featureless plateau, beyond this range it increases very rapidly.

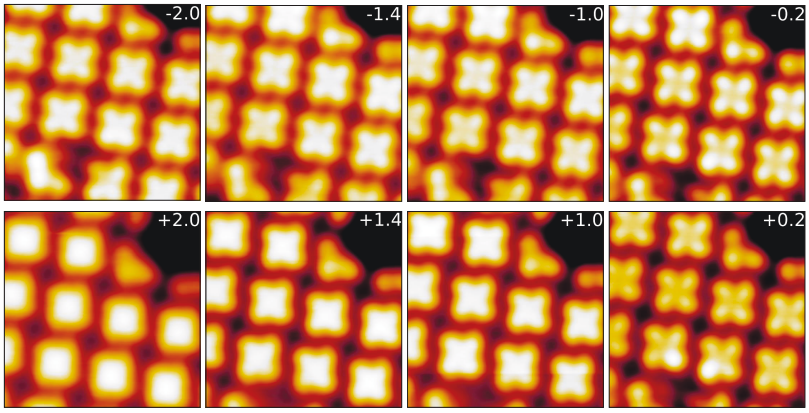

Figure 5.9: Series of STM images of the same surface region, acquired at different bias voltages (the correspondent V_b, in volts, is written at the top-right of each images). For all images, STM parameters: I_t = 0.5 nA, 4.4x4.4 nm^2.

In figure 5.10 we compare the STM image taken at +2.4 V with the correspondent DFT-simulated image. The image is taken around the maximum of the phenyl PDOS (fig. 5.8, light blue curve). At this bias the DFT-simulated image is almost identical to the experimental one supporting the validity of the calculated structure.

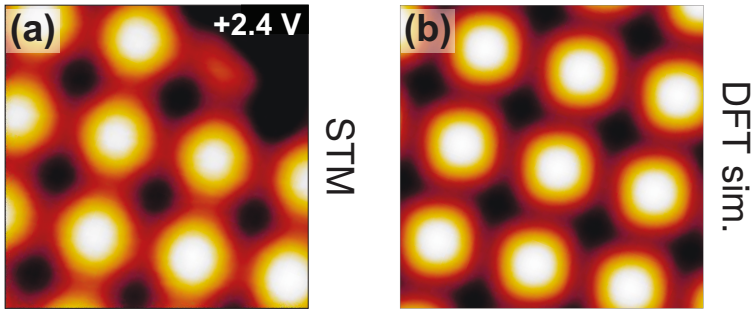

Figure 5.10: Comparison between STM-measured and DFT-simulated images at the maximum of the phenyl DOS. (a) Atomic resolution STM image on NiTPP/Cu(100) film. NiTPP molecule is superimposed. STM image parameters: V_b = +2.4 V, I_t = 0.5 nA, image size 4.4x4.4 nm^2. (b) the correspondent DFT simulated STM image.

5.3.2 Valence band

Figure 5.11a shows the angle-integrated photoelectron spectra of the clean Cu(100) substrate (red line) and of the NiTPP/Cu(100) (blue line). The valence band of the clean copper is dominated by the *sp* band and has a rather featureless plateau, while the NiTPP/Cu(100) spectrum shows two prominent features at binding energies (BEs) of 0.15 eV and 0.98 eV. A third feature, at 1.73 eV, becomes resolvable only after performing μ-ARPES measurements, because it is hidden under the Cu 3*d* bands (all three features are marked in fig 5.11a). The corresponding angle-

resolved photoemission maps, at these three BE energies, have been acquired and are presented in figure 5.11b. We remind that, in the μ-ARPES maps, the entire $\{k_x, k_y\}$ momentum space is acquired at once a given kinetic energy. The wide reciprocal space range covers $k_x, k_y \in [-2.0, 2.0]$ Å^{-1}. Several images (>20) at the same energy are acquired in one scan while moving the sample holder with a constant speed (1.5 μm/s) in order to avoid radiation damage. The typical exposure time for each image is 3 s.

The momentum maps in figure 5.11b were symmetrized according to the 4-fold symmetry of the substrate, getting rid of illumination effects related to experimental geometry, *i.e.* the grazing incidence on the sample of the synchrotron radiation. In figure 5.11b (bottom right), a μ-ARPES map of the clean copper, taken at binding energy of 0.98 eV, is shown as well. This BE corresponds to the one of the 2nd peak of the NiTPP/Cu(100) system. The sharp features indicated by the arrows and having a four-fold symmetry are the *sp*-band of the Cu(100) substrate [126]. By comparing the clean Cu and NiTPP/Cu(100) μ-ARPES maps at the 2nd peak position, it is immediately clear that new and distinct features appear upon molecular adsorption.

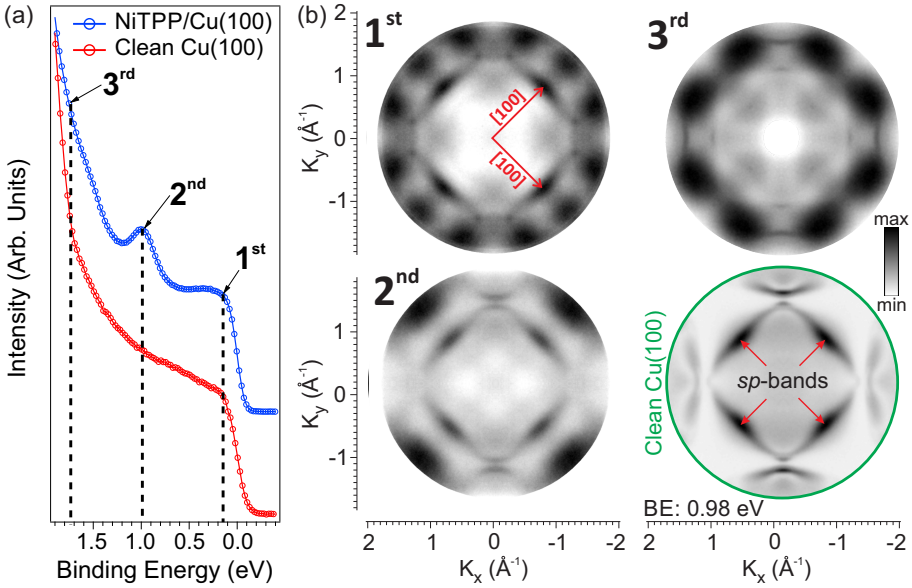

Figure 5.11: (a) Angle-integrated photoemission spectrum of clean Cu(100) and NiTPP/Cu(100) acquired at 26 eV of photon energy. (b) μ-ARPES patterns at the three energies indicated in (a). Bottom-left corner: μ-ARPES of the clean copper taken at the same binding energy of the 2nd peak. All momentum maps are measured at $h\nu = 26$ eV.

The assignment of individual molecular orbitals to the observed peaks in the integrated valence band spectrum, carried out only on the basis of the calculated PDOS, might be problematic due to fundamental limitations of DFT, such as the wrong asymptotic behavior of the potential or the band gap problem due to the derivative-discontinuity issue [127, 128]. Indeed, although the

HSE functional presents some improvement over GGA, it still may lead to an incorrect energy alignment [129]. Moreover, the PDOS for various molecular states extends over several eV due to hybridization with the substrate. Therefore, a complementary experimental technique allowing for a deconvolution of the molecular emissions into contributions from different molecular orbitals would be desirable. This can be realized by utilizing the angular distribution of the photoemitted electrons in the μ-ARPES presented in figure 5.11. These experimental momentum maps can be compared to simulated orbital patterns based on DFT calculations. Within the MOT approach [20, 130, 10, 101] introduced in section 3.5, the photoemitted electron is approximated by a plane wave. Thus the angular dependence of the photoemission intensity is determined by the Fourier transform (FT) of the respective initial state wave function.

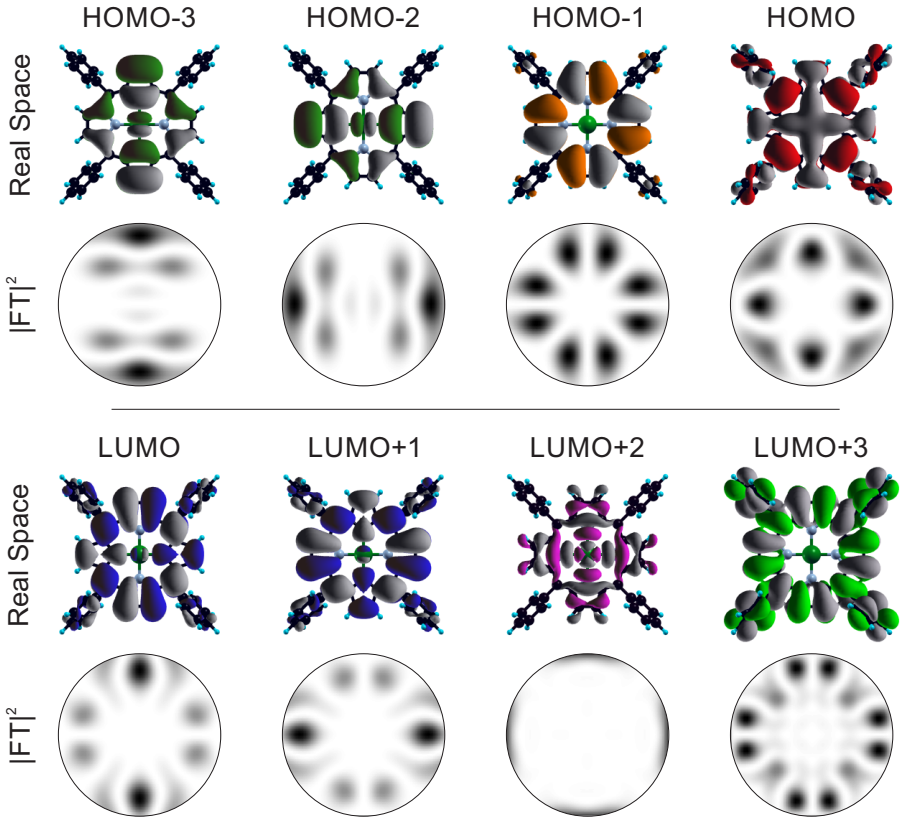

Figure 5.12: Calculated real space molecular orbitals for the gas-phase NiTPP, from HOMO-3 up to LUMO+3, with the correspondent $|\mathrm{FT}|^2$ below. The k range in the $|\mathrm{FT}|^2$s is: k_x;$k_y \in [-2.2, 2.2]\text{Å}^{-1}$

Figure 5.12 shows the molecular orbitals (MOs) from HOMO-3 up to LUMO+3 with the correspondent $|\mathrm{FT}|^2$. MOs are calculated starting from the Kohn-Sham eigenstates of a gas phase

molecule, and then a 3D Fourier transform of each considered orbital is performed. Subsequently, the 2D map is obtained by cutting the 3D FT at constant k value, *i.e.* at constant electron kinetic energy. This method is based on the assumption that the final state of the photo-emitted electron from the i-*th* molecular orbital can be approximated by a plane wave [20]. The gas-phase MO*s* were computed using the NWCHEM [131] DFT code, together with the range separated Heyd-Scuseria-Ernzerhof (HSE) hybrid functional [116] to account for exchange-correlation effects. These calculations were based on the NiTPP geometry determined above, which results from the adsorption on copper. Anyway, starting from the NiTPP gas-phase geometry produces only small changes in the simulated Fourier transforms. This is not surprising, because the corresponding states are located on the macrocycle, which is only slightly deformed upon adsorption. None of the states localized on the phenyl rings are found in the considered energy window (see fig. 5.8).

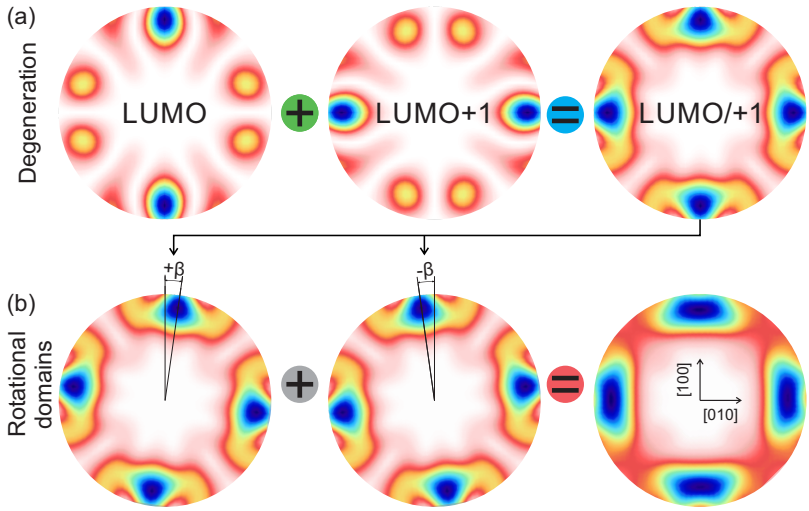

Figure 5.13: (a) The LUMO and LUMO+1 contributions to the final $|FT|^2$ are taken into account, since the two orbitals are degenerate. (b) The azimuthal rotation of the NiTPP within the two rotational domain is also considered. The resulting $|FT|^2$ is rotated by an angle $\pm\alpha$ with respect to the [100] direction and summed up. The so obtained $|FT|^2$ can be directly compared to the measured μ-ARPES maps. β is varied until a good agreement between theoretical and experimental data is found.

Because μ-ARPES averages over a large number of molecules, the two mirror domains of NiTPP with different azimuthal orientations of the molecules must be taken into account. Moreover, due to the degeneracy of some molecular states in the gas phase, *e.g.* LUMO and LUMO+1 (in the following abbreviated with LUMO/+1), the simulated ARPES maps should be computed as a superposition of such degenerate states. In figure 5.13 we report, as an example, the procedure followed to obtain the LUMO/+1 $|FT|^2$ which will be shown later. First, LUMO and LUMO+1, which are degenerate and rotated by 90° one with respect to the other, are summed (fig. 5.13a). In the last step, the contribution of the different NiTPP azimuthal orientations within the two

domains (A and B) needs to be taken into account. This is done by rotating the $|FT|^2$ obtained previously by an angle $\pm\beta$ with respect to the copper [100] direction (fig. 5.13b). β was varied until a good agreement between the experimental μ-ARPES and simulated $|FT|^2$ was reached. This procedure was used to reproduce the $|FT|^2 s$ which better resemble the three molecular features measured experimentally (see fig. 5.12). The corresponding results are shown in figure 5.14. Based on the excellent agreement between experimental and theoretical momentum maps, the features in the photoelectron spectra of NiTPP/Cu(100) can now be unambiguously assigned to the emissions from the LUMO+3, LUMO/LUMO+1 and HOMO-1 of NiTPP, respectively. This provides direct feedback to the theory on the choice of the best approximation for exchange-correlation effects in DFT.

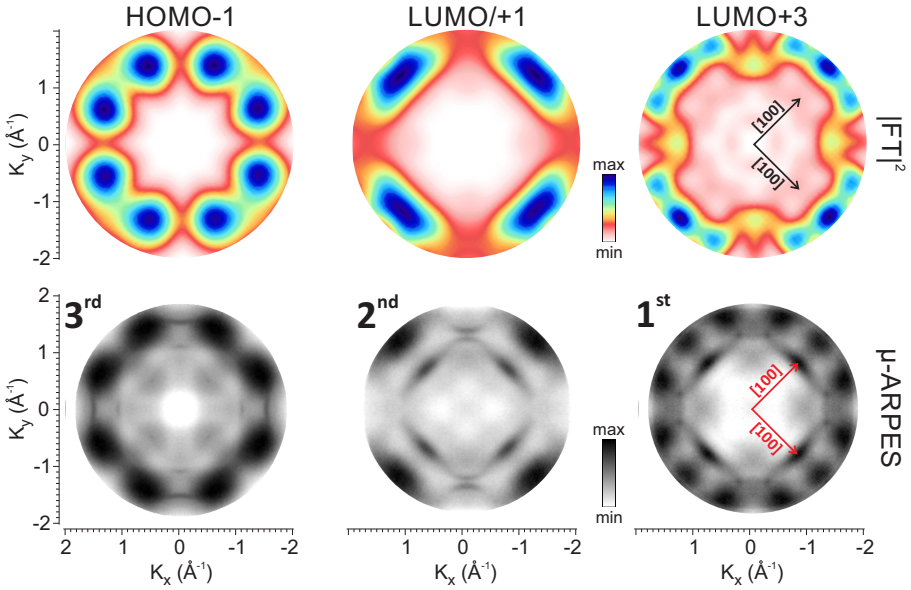

Figure 5.14: Comparison between μ-ARPES measured patterns (bottom) and the correspondent calculated $|FT|^2$s of the molecular orbitals (top). In the experimental maps, the sharp inner features are related to the copper (100) *sp*-band (see also fig. 5.12).

The MOT analysis also confirms the tentative assignment suggested by the computed PDOS and proves that indeed the gas-phase LUMO+3 and the degenerate LUMO and LUMO+1 become occupied upon adsorption of NiTPP on the metal surface, demonstrating the strong chemisorption nature of the NiTPP/Cu interaction. The results also show that the HOMO-1, rather than the HOMO, is the origin of the feature at a BE of 1.73 eV. Note that the HOMO and HOMO-1 are quite close in energy for the gas-phase NiTPP and the PDOS of the NiTPP/Cu interface also predicts that the HOMO and HOMO-1 change their energetic order. Since the HOMO-1 peak sits on the onset of the strong Cu *d*-band emissions, no molecular features were observed in that energy range. Although the calculated PDOS (see fig. 5.6) predicts the partial occupation of the gas-phase

LUMO+2, no features related to this orbital were measured in the μ-ARPES maps. Note that this might be related to the fact that the LUMO+2 momentum map shows only four narrow lobes, presumably located outside the experimentally probed k-space range.

Exploiting the clear signals from the *sp* band of the Cu substrate in the momentum maps, the orientation of the molecule with respect to the high symmetry substrate directions can be easily determined. The best agreement between all experimental and corresponding simulated momentum maps is for an azimuthal orientation of NiTPP of $\pm 8^\circ$ with respect to the [001] direction of the substrate. Within experimental error bars, this agrees with the orientation determined by the analysis of the STM images.

5.3.3 Core level spectroscopies

The changes in the electronic structure are also supported by angle-resolved NEXAFS spectroscopy. The occupancy of the empty states can be determined by looking at the intensity of the π^* resonances. In general, this analysis is carried out by comparing the NEXAFS spectrum of a monolayer organic film, where the molecule-substrate interaction plays a fundamental role, to the one acquired on the multilayer, where the effect of this interaction is indeed reduced. In the absence of the latter, the NEXAFS analysis can be based on multilayer references, also for similar metalloporphyrins, available in literature.

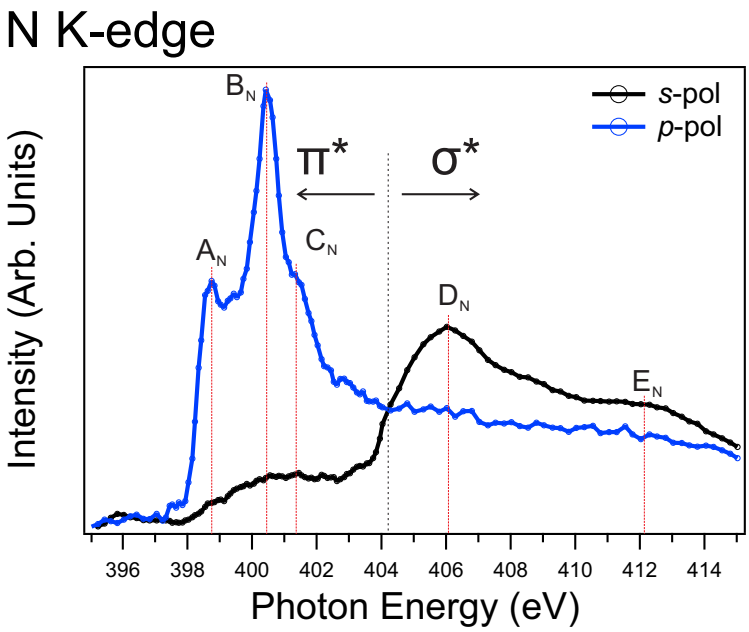

Figure 5.15: Nitrogen K-edge of NiTPP/Cu(100). The main peaks, related to specific transitions to unoccupied states are indicated by the dashed lines, and labeled in alphabetic order, starting from the pre-edge.

Angle-dependent NEXAFS spectra taken at the nitrogen K-edge are presented in figure 5.15. Five features are clearly identified and marked: A_N at 398.8 eV, B_N at 400.4 eV, C_N at 401.4 eV, D_N at 406.1 eV, and E_N at 412.2 eV. All peaks show a strong polarization dependence: while the first three are enhanced in the spectra measured with *p*-pol synchrotron light and almost vanish in with *s*-pol. The other two features, D_N and E_N, have the opposite behaviour. Since these resonances originate from the four pyrrolic nitrogens of the macrocycle, which lies almost planar on the copper surface, this behaviour can be explained associating A_N, B_N and C_N to $1s \rightarrow \pi^*$ transitions, D_N and E_N, instead, to $1s \rightarrow \sigma^*$. The present analysis is confirmed by previous studies on CoTPP, ZnTPP [132] and CuTPP [37]. In the latter, theoretical calculations on the NEXAFS

spectral lines help to understand the origin of the main three π^* resonances. A_N is mostly related to 1s→LUMO and 1s→LUMO+3 transitions [37], B_N, instead, to 1s→LUMO+4 and 1s→LUMO+8. The measured energy position of these peaks is very close to the calculated one [37]. The charge transfer influence also the A_N/B_N intensity ratio [37]. In the multilayer spectrum, where no charge transfer is observed [132], it is close to one. Here, instead, we note that the A_N is partially quenched, supporting the LUMO+3 filling scenario.

The strong molecule-substrate interaction affects also the electronic structure of the Ni ion at the macrocycle center. For this reason we measured the Ni $2p_{3/2}$ core level, which is presented in figure 5.16a. The Ni 2p XPS spectrum shows one main peak at BE = 853.15 eV and weak satellite features located at higher BE. The binding energy position of the peak was determined using a standard fitting procedure with a Doniach-Sunjic lineshape and the energy scale was referred to E_F of copper . This value agrees well with the ones reported for monolayer NiTPP deposited on other reactive surfaces, such as Cu(111) [133] and fcc Co(100)/Cu(100) [38]. The binding energy of 853.15 eV is typical for the metallic nickel in the (0) oxidation state [134]. Conversely, the nickel porphyrin adsorbed on Au(111), an almost inert surface, does not show any chemical shift of the Ni $2p_{3/2}$ core level, its binding energy (∼855.4 eV) corresponds to the one of Ni in a formal 2^+ oxidation state, coordinated with the four nitrogens of the macrocycle [135].

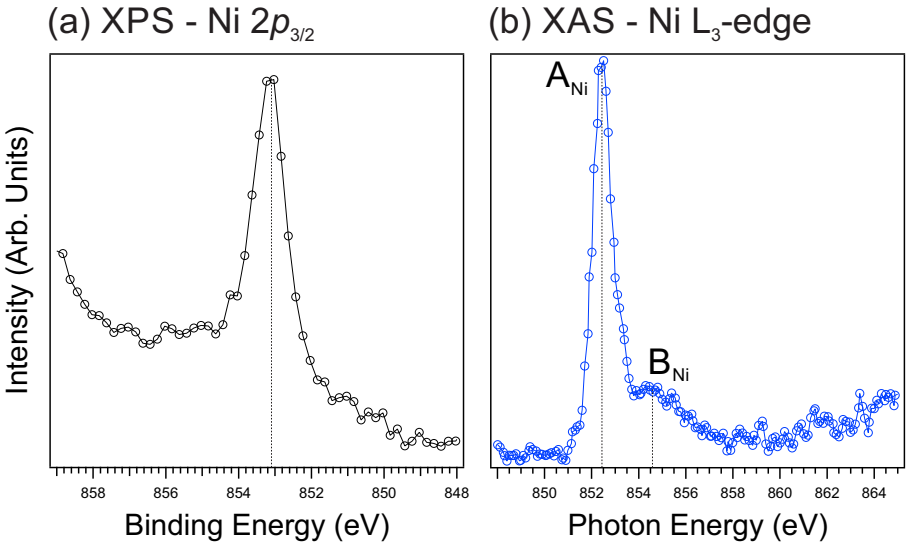

Figure 5.16: (a) Ni $2p_{3/2}$ core level photoemission spectra of NiTPP/Cu(100), experimental data and fit. Spectrum collected in normal emission geometry with photon energy of 1000 eV. (b) p-pol XAS spectrum at the Ni L_3-edge.

The core level energy shift in the XPS spectrum might be caused by initial/final state effects, or a combination of both. A possible initial state effect is the charge transfer from the copper substrate to the Ni ion, which results in a reduction of its oxidation state. This is in agreement

with the filling up of the LUMOs observed in before. The charge transfer is facilitated by the short Cu-Ni distance, which is about 2 Å. Alternatively, final state effects could be responsible for the energy shift of the main peak in the Ni $2p_{3/2}$ core level spectrum of the NiTPP monolayer. According to the Gunnarsson and Schönhammer model [136], the charge transfer of valence band Cu electron into the NiTPP unoccupied states may screen the core-hole. However, the present data cannot lead to a final conclusion, since it is not possible to separate the contribution of initial and final state effects related to the charge transfer.

To further investigate the chemical properties of the Ni atom, in figure 5.16b) we present the NEXAFS spectrum of NiTPP/Cu(100) system taken at the Ni L_3-edge. The two main features visible in the spectrum, A_{Ni} and B_{Ni}, are a fingerprint of the Ni coordination within the porphyrin macrocycle [122]. The A_{Ni} and B_{Ni} energy position (852.5 eV and 854.5 eV, respectively) differ from the ones of the NiTPP multilayer by ∼2 eV towards lower photon energies, which is a further indication of the Ni(0) oxidation state [137].

It is also worth mentioning that another possible explanation for the energy shift in core level spectra is the metal interexchange between the substrate atom with the one inside the molecule. This phenomenon has been observed for different porphyrins [138] and phthalocyanines [139], such as NiDBrDPP, NiTBrPP and CoPC, deposited on Cu(111). In the first case, the substitution must be triggered by temperature, because at RT almost no exchange is observed, while annealing the sample at 160 °C leads to a 100 %-complete ion exchange (slightly less for NiTBrPP). This process is easily followed in the Ni $2p_{3/2}$ XPS, where two distinguishable Ni species are present. One associated to the metallic Ni, *i.e.* Ni(0), and the other to the Ni(II) of NiTPP. Annealing the sample at higher temperature leads to the decreasing of the former and increasing of the latter, while the total area under the two peaks remains constant. CoPC behaves similarly, except that immediately after deposition a few percentage of the molecules have already exchanges their metal ions turning into CuPC [139], reaching the 100 % annealing up to 300 °C.

No Ni–Cu interexchange was observed for NiTPP adsorbed on the Cu(100) surface. The cited works suggest that the temperature is needed to trigger the process, while we would like to note that the present experiments were performed at room temperature and the samples were not annealed after molecular deposition. Additionally, we deposited the H_2TPP molecules on Cu(100) without seeing any evidence of TPP self-metalation at room temperature. This can be verified by looking at the presence in the N 1*s* core-level spectrum of the two peaks related to the non-equivalent nitrogen atoms of H_2TPP. The exposure of the NiTPP/Cu(100) system to NO, which will be shown later, in chapter 7, further supports our conclusions, excluding the formation of the CuTPP *via* de-metalation of the NiTPP. Changes in the oxidation state of the porphyrin metal ion have been already reported for the other systems, such as CoTPP adsorbed on Ag(111) surface [16]. The observed chemical shift (∼2 eV) in the Co $2p_{3/2}$ core level spectrum, between the CoTPP mono and multilayer, was explained in terms of initial/final states effects related to the change of the cobalt ion oxidation state (Co(II)→Co(0)). In this case the Ag atoms cannot be introduced to the porphyrin macrocycle, preventing the Ni-Ag interexchange.

5.4 LEEM studies of the NiTPP self-assembly

5.4.1 Radiation damage of the molecular film

It is well known that particle beam irradiation may damage the organic film, breaking molecules apart [140]. In case of electron beam, this effect must be properly taken into account when we access the organic-metal interface with techniques that involve electron beam as surface probe, such as low energy electron microscopy (LEEM), Auger electron spectroscopy (AES) and low energy electron diffraction (LEED). Studying the induced damage caused by electron irradiation may be also of general interest for other spectro-microscopic tools used to characterize the adsorption behaviour and the physical properties of the organic films *e.g.* scanning electron microscope (SEM), electron energy loss spectroscopy (EELS). In these kind of experiments, the effects of the organic layer corruption can bee seen typically in the degradation of the image resolution [141] or broadening of diffraction/spectroscopic features with an increasing of the background noise. In the nanostructure fabrication field, instead, the damage induced by the surface irradiation with an electron beam is exploited to achieve the control over the chemical composition on surfaces. For example, electron irradiation can be used to chemically activate an organic layer such that it become locally reactive toward the decomposition of other molecules [142]. The focused electron beam induced deposition is another well-established method which exploits the capability of the electron beam to decompose precursor molecules to create 3D metal-containing nanoscale structures [143].

In all the examples mentioned, quantifying the radiation damage becomes of crucial importance. For this reason, this section is dedicated to the study of the degradation of the NiTPP monolayer, upon electron irradiation, at different incident electron kinetic energies ($E^{e^-}_{kin}$) in the [6,50] eV range.

The first order expression for the rate of change of coverage upon electron irradiation is [144]:

$$\frac{d\theta}{dt} = -F\sigma\theta(t) \tag{5.3}$$

where $\theta(t)$ is the coverage (adsorbed species/cm^2) and F is the electron flux density. We can integrate eq. 5.3 to obtain:

$$\theta(t) = \theta_0 e^{-F\sigma t} = \theta_0 e^{-\frac{t}{\tau}} \tag{5.4}$$

where $\theta(t)$ is the coverage after time t of electron bombardment, θ_0 is the initial coverage and τ the characteristic decay time. According to ref. [145], we can express σ as a function of both F and τ:

$$\sigma = \frac{1}{\tau F} \tag{5.5}$$

The intensity decay of the diffraction spots can be used to monitor the radiation damaged induced by the electron beam [146] to the NiTPP molecular film. Thus, the characteristic decay time, τ, for the long-range ordered phase of the NiTPP, can be extracted by measuring the decrease

in the related LEED spot intensity as a function of the time. This τ_{LEED} is twice as large of the effective one. For this reason, the τ reported below have been properly scaled. This method was successfully employed to monitor the induced radiation damage as a function of the electron dose for cobalt and copper phthalocyanines [147, 148].

SPELEEM can be used for this purpose because it allows one to easily switch between the real and reciprocal space, just changing instrumental settings. Furthermore, by inserting an illumination aperture immediately after the electron gun, the irradiated surface area is reduced down to only $\sim$ 20 μm^2. Therefore, by moving the sample by 10-20 μm we always probe a non-irradiated area. In this way one entire data set can be collected with only one sample preparation.

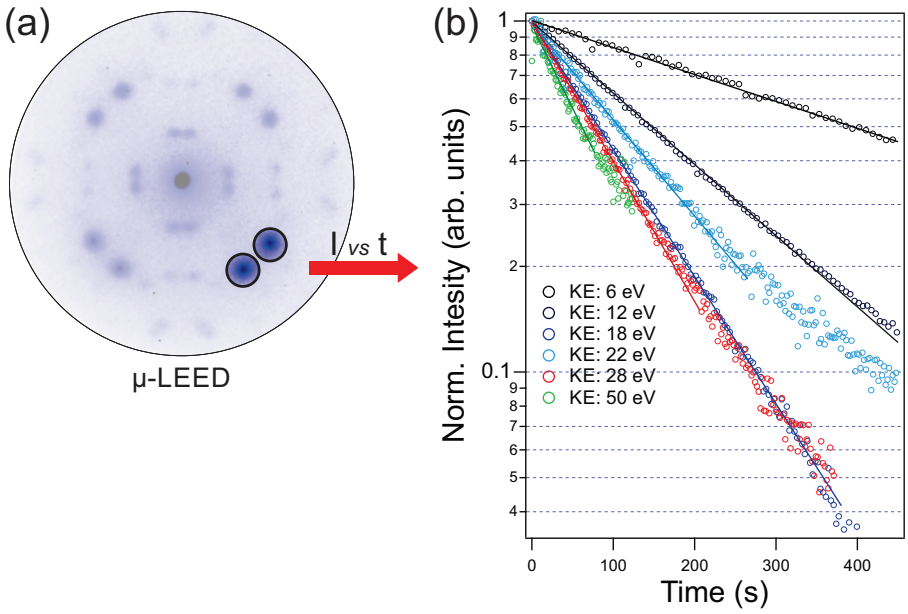

Figure 5.17: μ-LEED of NiTPP/Cu(100) film, SV: 12 eV. A semi-transparent mask highlights the spots used to measure the I *vs* t curve. (b) Intensity decay as a function of the time, for the two diffraction spots marked in (a), for different SV energies. Electron flux density: $7.4 \cdot 10^{14}$ $e^-/(cm^2 \cdot s)$.

The experiment was performed as follows: a NiTPP long-range ordered layer was grown on Cu(100) and the decay of the diffraction spots was monitored by acquiring every 5 seconds the LEED pattern of the NiTPP/Cu(100) surface. The obtained image stack was subsequently analyzed by extracting the spot intensity as a function of time. The experiment was repeated with different kinetic energies of the impinging electrons, by changing the start voltage in the 6-50 eV range. The sample was moved to a "fresh" area immediately before starting a new measurement. Figure 5.17a shows the typical LEED pattern of NiTPP/Cu(100), taken at SV = 12 eV. The two diffraction spots used for the present analysis are marked on the figure. As it will be discussed in

detail in the next section, these two diffraction spots are generated from two equivalent mirrored domains of the NiTPP with respect to the Cu(100) symmetry directions. The averaged intensity of the two spots, as a function of time, is reported in figure 5.17b for several $E^{e^-}_{kin}$. Since the intensity decays exponentially only in the first 250-300 s, according to equation 5.4, each spectrum was fitted in the region where the exponential decay can be clearly established. The so obtained values for the characteristic time (τ) are displayed in figure 5.18a.

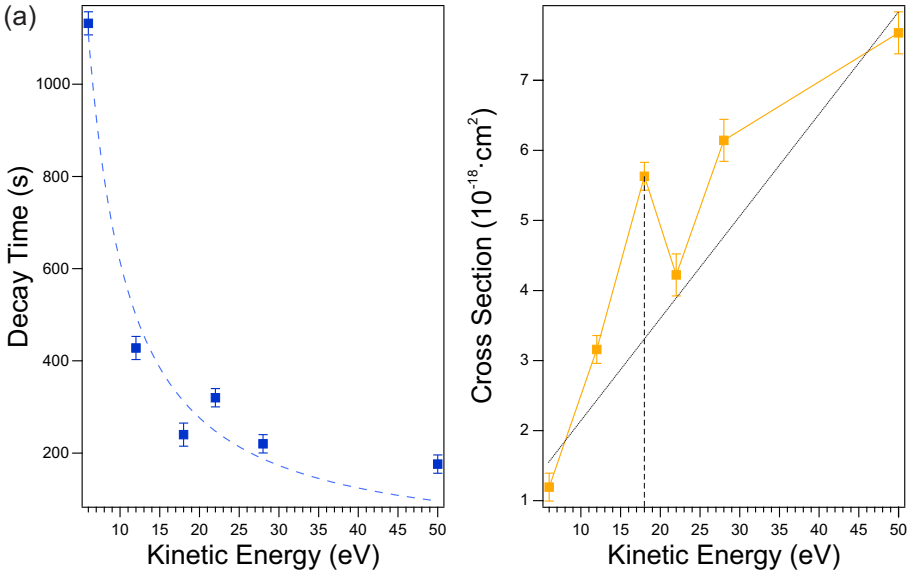

Figure 5.18: (a) Characteristic decay time of the intensity of LEED spots related to the NiTPP lattice. (b) Effective cross-section as a function of the incident electron energy. Electron flux density: $7.4 \cdot 10^{14}$ $e^-/(cm^2 \cdot s)$.

Looking at figure 5.18a we can conclude that working at very low energies, *e.g.* 4-6 eV, with an electron flux density of $F = 7.4 \cdot 10^{14}$ $e^-/(cm^2 \cdot s)$, the same surface area can be measured for a 6-8 min without being severely damaged.

Four main mechanisms may lead to the molecular dissociation in the low electron energy regime (typically below 100 eV): dissociative electron attachment (DEA), dissociative ionization (DI), neutral dissociation (ND) and dipolar dissociation (DD) [143]. DEA is a resonant process occurring at low energies (from 0 to 20 eV) in which an electron binds to the neutral molecule forming a negative ion, which relaxes either by re-emitting the captured electron or through dissociation. In DI, instead, the incident electron ionizes the molecule. If the incident electron kinetic energy exceeds the ionization threshold, the cation goes to an excited state and its decaying leads to fragmentation. The related cross-section increases monotonically from $E^{e^-}_{kin}$ ~12-15 eV and reaching a broad maximum at 50-70 eV. In ND, no cations or anions are formed. The inelastic scattering of the incoming electron promotes the molecule to an excited state, which, decaying, may lead to fragmentation. ND cross-section increases gradually, with increasing $E^{e^-}_{kin}$,

because new excitation channels open up. It has a fairly high cross-section even at $E^{e^-}_{kin} = 100$ eV. DD is similarly to ND but the molecular fragments, resulting from dissociation, are positively and negatively charged. This process activates usually above an incident electron energy of 12 eV [149, 143].

In order to separate the cross-section of each specific process, a complicated experimental set-up is required. Especially a mass spectrometer is needed for the anion/cation detection. In our experimental set-up is not possible to discriminate between the different products of the molecular dissociation. We determine an "effective" electron-induced cross-section (σ_{eff}), which reflects the most dominant process for each energy. Knowing the characteristic τ for each incident electron kinetic energy and the electron flux density on the sample, the effective cross-section can be calculated using the equation 5.5. The energy-dependent σ_{eff} are displayed in figure 5.18b. In the [6-50] eV energy range, σ_{eff} increases almost linearly, showing a peak of magnitude ($5.6 \pm 0.2 \cdot 10^{-18}$ cm^2) at 18 eV. Because of the few data points in that energy region the peak is not well-defined. An analogue peak at this kinetic energy has been observed already for other organic molecules, such as oligonucleotides (DNA bases), irradiated with low energy electrons [150]. DI, ND and DD are all linear processes. Their cross-sections increase monotonically increasing $E^{e^-}_{kin}$, while DEA is the only resonant mechanism. Therefore, similarly to ref. [150], we interpret this peak at 18 eV to arise from dissociative electron attachment.

Most of the works studying radiation damage of porphyrin and phthalocyanine [147, 148, 146] films are mainly focused on the maximum electron dose allowed before damaging the sample. Here, instead, we reported the values of σ and τ as a function of the incident electron energy, which might be useful for whom would like to study organic-metal interfaces with techniques micro-spectroscopic methods that use low energy electrons as a probe. In particular, the graph in figure 5.18a gives an estimation of the time that the sample can be irradiated before being severely damaged as a function of the incident electron kinetic energy. While looking at σ_{eff} *vs.* time curve (see fig. 5.18b) it is suggested to avoid $E^{e^-}_{kin}$ around 16-20 eV because of the resonant peak due to DEA.

5.4.2 Dark-field LEEM on the ordered NiTPP phases

Dark-field (DF) LEEM can be used to assess the lateral extent of the two NiTPP domains and exclude the formation of other phases, at larger length scale compare to STM. Imaging was carried out using the fractional order diffraction spots of A and B phases. The inset in figure 5.19a shows a μ-LEED pattern of the NiTPP/Cu(100) surface acquired at the SPELEEM set-up. Inserting the contrast aperture, we selectively image one of the two mirrored domains (fig. 5.19a), the corresponding DF images are presented in figure 5.2c (DF_A) and 5.2d (DF_B). Simultaneously, we also acquired the bright-field (BF) image of the surface, using the zero-order diffraction spot (figure 5.2b), which it is not sensitive to the orientation of the equivalent NiTPP domains. If no other phases are present on the surface, the two images would be complementary. In order to visualize the lateral extension of these two domains, the asymmetry betweenDF_A and DF_B has

been calculated in the following way: $(DF_A - DF_B)/(DF_A + DF_B)$. The resulting image is shown in figure 5.2e, the blue and red areas are associated to A and B phases, respectively.

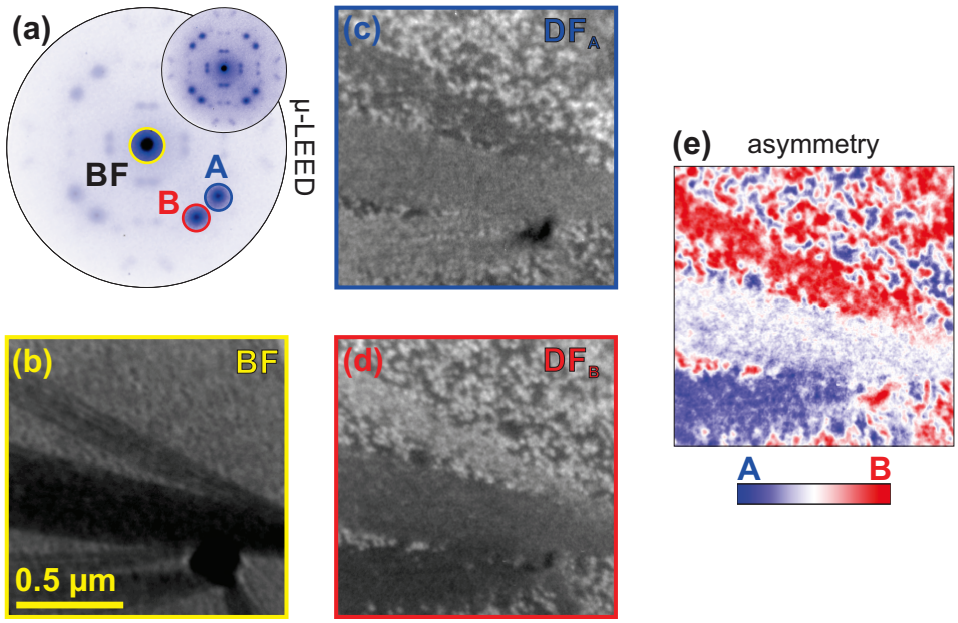

Figure 5.19: (a) μ-LEED of NiTPP/Cu(100) film, SV: 12 eV. A transparent mask highlights the diffraction spots used for the dark-field imaging, marked with A, B and BF, respectively. Inset: μ-LEED of NiTPP/Cu(100) without the mask. (b) Bright-field image of the surface, SV: 4 eV. (c) Dark-field image, taken using the A diffraction spot, SV: 4 eV. (d) Dark-field image, taken using the B diffraction spot, SV: 4 eV. (e) Lateral distribution of A and B domains calculated as the asymmetry of (c) and (d).

Looking at the asymmetry, A and B are almost complementary over the entire image, except for a region, crossing almost horizontally the image in the middle, which does not show a clear red or blue contrast. The area where no molecular order is observed is the darkest in the the BF image taken at SV = 4 eV (fig. 5.19b). LEEM images taken at larger field of view reveals that the surface is rich of such areas having this particular contrast at this energy. Nevertheless, the reflectivity curve (LEEM-IV) taken on bright and dark areas, does not change significantly, *i.e.* these regions have the same geometrical structure. Only the intensity changes, revealing that the dark areas are more disordered, preventing the formation of a long range ordered molecular lattice. Above and below we note other two stripe-like regions where B and A, respectively, are almost homogeneous and extend for few microns. These areas are associated to the step bunches. Elsewhere A and B are not bigger than 100/200 nm, which is in agreement with STM images taken at higher coverage.

5.5 From nickel to cobalt tetraphenyl porphyrin

The robustness of the MOT approach will be tested by extending it to another metalloporphyrin, the cobalt tetraphenyl porphyrin (CoTPP), adsorbed on the same Cu(100) surface. CoTPP were deposited on Cu(100) following the exact same procedure employed for NiTPP, which is described in chapter 4. Upon deposition, CoTPP exhibits a LEED pattern (not shown) almost identical to the one of NiTPP shown in figure 5.2. Therefore, we conclude that also CoTPP forms the same two well-ordered domains on the surface, which are mirrored respect to the high symmetry directions of the (100) surface.

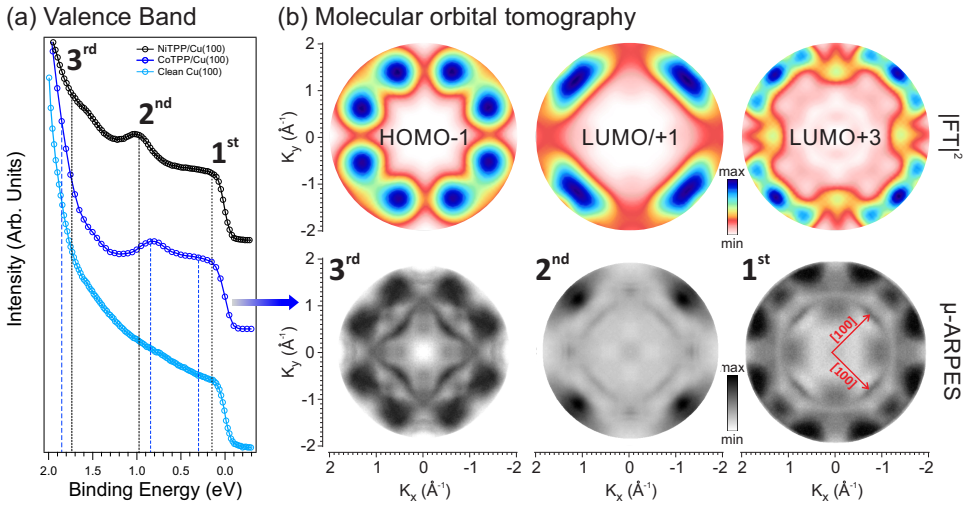

Figure 5.20: (a) Angle integrated valence band for clean Cu(100), CoTPP/Cu(100) and NiTPP/Cu(100). (b) Comparison between μ-ARPES measured patterns (bottom) of CoTPP/Cu(100) and the calculated $|FT|^2$ of the CoTPP molecular orbitals (top). In the experimental maps, the sharp inner features are related to the *sp* band of the copper surface. The angle-integrated valence band and all the μ-ARPES were taken at $h\nu = 27$ eV.

In figure 5.20a we compare the angle-integrated photoelectron spectra of the clean Cu(100) substrate (light blue line), CoTPP/Cu(100) (blue line) and NiTPP/Cu(100) interfaces (black line). While the valence band of the clean copper has a rather featureless plateau, the CoTPP/Cu(100) spectrum shows two prominent features at binding energies (BEs) of 0.30 eV and 0.85 eV. A third feature, at 1.85 eV, becomes resolvable only after performing μ-ARPES measurements, because it is hidden under the strong Cu 3*d* bands (all three features are marked in fig. 5.20a). In figure 5.20b (bottom row) we present the angle-resolved photoemission momentum maps collected at these three energies. If compared to the μ-ARPES of the clean substrate (section 5.3, fig. 5.11b), these momentum maps show distinct patterns, which must be ascribed to the adsorbed molecules. Similarly to NiTPP/Cu(100), we determined the energy level alignment upon CoTPP deposition by comparing the measured μ-ARPES pattern to the $|FT^2|$ of gas-phase molecular orbital wave

functions, within the MOT approach [20, 130, 10, 101].

First of all, we note that the CoTPP (fig. 5.20b) and NiTPP (fig. 5.14) momentum maps are very similar, suggesting that the molecular geometry and the charge distribution of the frontier orbitals are not strongly influenced by the metal ion at the porphyrin core. Furthermore, the Fourier transforms of the gas-phase MOs (from HOMO-3 to LUMO+3), calculated for the CoTPP molecule, are almost identical to the NiTPP ones. This can be explained by the fact that these orbitals do not own a strong *d* character, where the difference between Ni and Co lies, but are located almost on the macrocycle and phenyl moieties.

The MOT analysis confirms that, also for CoTPP/Cu(100), the gas-phase LUMO+3 and the degenerate LUMO and LUMO+1 become partially occupied upon adsorption on the copper surface, demonstrating the chemisorption nature of the molecule-substrate interaction. The peak at higher BE is attributed to HOMO-1, rather than the HOMO as already observed for NiTPP/Cu(100) (see sec. 5.3.2). These two orbitals change their energetic order upon adsorption. Since the HOMO peak sits at the onset of the strong Cu *d*-band emissions, no molecular features were observed in that energy range. Similarly to the case of NiTPP on Cu(100), there is no experimental evidence of the occupation of LUMO+2.

We focus now our attention on the energy shift between the valence band features corresponding to the photoionization of NiTPP and CoTPP molecular orbitals adsorbed on the Cu(100) surface. In case of NiTPP, the HOMO-1 and LUMO+3 are shifted by 120 and 150 meV towards higher binding energies respect to the same features in the CoTPP spectrum, the degenerate LUMO/LUMO+1, instead, moves in the opposite direction by 130 meV. Since the occupation of the *d* orbitals is different going from Co to Ni in the MTPP [55], these changes can be related to the metal ion at the porphyrin center. However, the calculations do not reveal a strong *d* character of the HOMO-1 and LUMOs discussed above, where the charge is mostly delocalized on the macrocycle. It is safe to state that the presence of nickel, rather than cobalt ion inside the porphyrin, modifies the overall molecule-substrate interaction, possibly leading to a slightly different adsorption height, as for MTPP deposited on Ag(111) [52]. This difference may affect the energy position of the molecular orbitals with respect the Fermi level. In order to unravel the complex mechanism that determines the orbital BE*s* depending on the metal ion inside the porphyrin, further theoretical calculations on the CoTPP/Cu(100) interface are needed. On the other hand, we also show that the comparison between $|FT^2|$s and experimental μ-ARPES maps can be extended also to CoTPP on the same surface and reliable assignment of the observed experimental features in the VB to the corresponding frontier molecular orbitals can be achieved.

5.6 Conclusions

In conclusion, combining multiple surface science techniques, such as STM, LEED, NEXAFS and ARPES, with ab-initio DFT calculations, we develop a consistent picture of the adsorption behavior of NiTPP on Cu(100) and clarify the electronic structure of this organic/metal interface.

NiTPP molecules form two long-range ordered domains, mirrored with respect to the [001] direction and commensurate with the substrate. Van-der-Waals-corrected DFT calculations reveal the NiTPP adsorption geometry: the molecules form a very close-packed arrangement, having the macrocycle lying only 2 Å above the metal surface. As a consequence, the four phenyl side-groups of NiTPP tilt and twist upwards, leading to the four main protrusions visible in STM images, in accordance with DFT simulations. The calculated adsorption geometry is supported by angle-dependent NEXAFS measurements, which confirm the strong twisting of the peripheral substituents and the planarity of the macrocycle. Due to the strong molecule-metal interaction, pronounced charge rearrangements are observed upon adsorption. In particular, hybrid functional DFT calculations suggest a significant charge transfer from Cu to the molecule resulting in the occupation of the gas-phase LUMO/LUMO+1 and LUMO+3 molecular orbitals, accompanied by a back-donation of charge from the molecule to the substrate. The interpretation of the three molecular resonances observed in the valence band regime is confirmed by molecular orbital tomography results. Thereby, our measured momentum maps allow us to unambiguously assign the photoemission features to molecular states and to accurately determine the azimuthal orientation of the molecule. This charge transfer leads to an energy shift of ~ 2.3 eV of the Ni $2p_{3/2}$ XPS core level, which can be explained in terms of both initial/final states effect, *i.e.* change in the Ni oxidation state or screening of core-hole by the occupied MOs. We exclude a Ni-Cu interexchange upon NiTPP adsorption.

The MOT analysis can be extended also to CoTPP/Cu(100). The CoTPP and NiTPP exhibit almost the same electronic structure upon adsorption on copper, which results in the occupation of the gas-phase LUMO+3, indicating that the overall molecule-substrate interaction is quite similar in both cases.

We also emphasize the complementary role of STM and μ-ARPES measurements for such systems. While the former provides information on the molecular states localized on the phenyl rings, the latter reveals the electronic structure of the frontier orbitals located on the macrocycle. Thus in general, a multi-technique approach including support from electronic structure calculations is necessary to develop a consistent picture of the adsorption behavior and electronic properties of interfaces between non-planar molecules and metallic surfaces.

Chapter 6

Electronic structure of NiTPP and CoTPP on different substrates

In the previous chapter we closely investigated the physical properties of NiTPP and CoTPP molecules deposited on the (100) copper surface, determining their adsorption configuration, as well as the electronic structure. We will now investigate the role of the substrate in the molecular energy level alignment by comparing the electronic properties of NiTPP and CoTPP deposited on two noble metals having different reactivities, such as copper and silver.

6.1 Introduction

Self-assembly of organic molecules on different substrates is one of the new routes towards building molecular nano-devices with innovative properties [151]. Using such a bottom-up approach, predetermined and defect-free two dimensional nano-structured materials may be synthesized in a simple and effective way. The metal substrate drastically affects the subtle equilibrium between weak and reversible lateral (intermolecular) and vertical (molecule-substrate) interactions, which are ultimately responsible for the self-assembly [152]. If the molecule-substrate interaction is either too weak or too strong, molecules may not be able to organize themselves in long-range ordered structures. To this end, the detailed knowledge of the electronic properties at the nano-scale of the self organizing molecular systems can provide the necessary know-how to build increasingly complex and chemically stable 2D functional nano-systems. From this perspective the anisotropy of (110) low symmetry surfaces offers a unique template to drive the molecular self-assembly [51, 153, 15].

Thanks to their great structural flexibility and their electronic structure, porphyrins are one of the most suitable candidates for 2D molecular array construction. So far, porphyrin systems, deposited on (110) substrates, have not been studied in detail and remain poorly understood. It has been shown that the molecule-substrate interaction is stronger when porphyrins are deposited on copper [37], while it gets weaker when the same molecules are adsorbed on silver [50]. In this

regard, molecular orbital tomography has been revealed to be a powerful tool for characterizing the organic-metal interfaces [121, 10], helping to determine the energy alignment of the molecular orbitals once the molecule is adsorbed on the metal surface.

In the present chapter, we will investigate the nickel and cobalt tetraphenyl porphyrins (NiTPP and CoTPP) molecules deposited on Cu(110) and Ag(100) by means of molecular orbital tomography and low energy electron diffraction. The former is used to determine the occupation of the frontier orbitals close to the Fermi energy, as well as the azimuthal orientation of the molecule respect to the substrate. The latter, instead, will give us the orientation and size of the unit cell of the long range ordered molecular film. Even though CoTPP/Cu(110) has been extensively studied using a combined experimental/theoretical approach [48], here we will be able to provide new insights on the filling of the unoccupied molecular orbitals due to the strong molecule-substrate interaction.

6.2 NiTPP and CoTPP on Cu(110)

The first step is the characterization of the NiTPP and CoTPP self-assembly on Cu(110). The LEED patterns of NiTPP and CoTPP are shown in figure 6.1a and 6.1b, respectively. Both molecules form a long range ordered structure on the Cu(110) surface, as demonstrated by the presence of sharp spots in the diffraction patterns. It is known that CoTPP on Cu(110) forms two domains (labeled with A and B) mirrored with respect to the [001] direction [48]. The simulated LEED pattern is superimposed to the experimental one (see fig. 6.1). The same structures is used for both NiTPP and CoTPP molecules. The simulated structure well reproduce the experimental patterns in both cases. Therefore, we can conclude that the different metal center does not change the orientation and size of the unit cell upon adsorption.

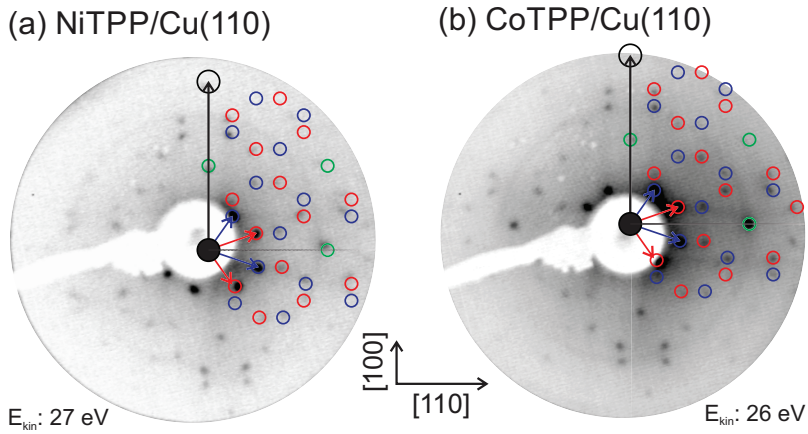

Figure 6.1: (a) LEED pattern of NiTPP deposited on Cu(110), taken at E_{kin}: 27eV. (b) LEED pattern of CoTPP on Cu(110) taken at E_{kin}: 26 eV. The simulated diffraction pattern is superimposed to the experimental ones. Red and blue circles mark diffraction spots belonging to the two mirrored domains. Green circles, instead, highlight the common spots to the two domains. The substrate first order diffraction spots are located outside, or almost at the edge, of the probed Ewald sphere at this energy and are indicated by the black arrows.

The molecular superstructures can be well described by the following matrices:

$$A = \begin{bmatrix} 2 & -4 \\ -6 & 2 \end{bmatrix} \qquad B = \begin{bmatrix} 2 & 4 \\ -6 & -2 \end{bmatrix}$$

Since the two domains are commensurate to the substrate, the matrices have all integer elements. The unit cell is not square and, for this reason, the two base vectors, separated by an angle of 74°, have different lengths: 15.3 and 16.9 Å, respectively.

Regarding the electronic structure of the NiTPP(CoTPP)/Cu(110) interface, figure 6.2a shows angle-integrated valence band structure of the clean Cu(110) substrate (light blue line), NiTPP/Cu(110) (black line) and CoTPP/Cu(110) (blue line). In that energy window, the valence band of clean

copper is dominated by the *sp* band and has a rather featureless plateau up to 1.5 eV. Conversely, the CoTPP/Cu(110) spectrum presents two prominent features at binding energies (BEs) of 0.15 eV and 0.70 eV (both marked in fig. 6.2a), while in the NiTPP spectrum they are shifted to BE of 0.12 eV and 0.89 eV, respectively. In the NiTPP VB, also a third feature becomes resolvable at 1.75 eV only after performing μ-ARPES measurements, because, similarly to the previous systems, this signal is hidden under the Cu 3*d* band signal.

μ-ARPES patterns were acquired in correspondence of the spectroscopic features identified in the previous paragraph and marked in figure 6.2a. The measured patterns are shown in fig 6.2b (middle and bottom row). Clean copper momentum maps (not shown here) exhibit only the sharp features of the *sp*-bands of the substrate at $k_y \cong 1$ Å, $k_x \in [-0.7, 0.7]$ Å. Upon deposition of the NiTPP and CoTPP molecules, extra features appear in μ-ARPES maps weakening the signal related to the copper states.

Within the MOT approach, the measured μ-ARPES map can be directly compared to the calculated $|\mathrm{FT}|^2$ of a specific molecular orbital. In order to further improve the agreement between the DFT simulations and the raw data, the $|\mathrm{FT}|^2$ have been corrected by the polarization factor $|\mathbf{A} \cdot \mathbf{k}|^2$, introduced in section 3.5 eq. 3.14. $|\mathbf{A} \cdot \mathbf{k}|^2$ accounts for the experimental geometry, *i.e.* the ARPES intensity is modulated by the scalar product between the potential vector of the incoming radiation **A** and the direction of the photoemitted electron **k** (see sec. 3.5). Finally, also the two rotational domains and the azimuthal orientation of the molecule within each domain must be taken into account. We bear in mind that the NiTPP and CoTPP frontier orbitals (from HOMO-3 to LUMO+3) are almost identical, for this reason, in the following figures, only calculations for the NiTPP molecules will be shown. The resulting $|\mathrm{FT}|^2$ are presented in figure 6.2b (top row).

Based on the excellent agreement between experimental and theoretical data, we make the following assignments: in case of NiTPP/Cu(110), the three observed features in the photoelectron spectrum correspond to the emissions from the LUMO+3, LUMO/LUMO+1 and HOMO-1 of the NiTPP molecules, respectively (see fig. 6.2b). A similar situation occurs also for the other porphyrin, where the two measured features were assigned to the LUMO+3 and LUMO/LUMO+1 of CoTPP. The gas-phase LUMO+3 and the degenerate LUMO and LUMO+1 become occupied upon adsorption of NiTPP and CoTPP on the Cu(110) surface, suggesting a strong charge transfer scenario between molecules and the metal substrate, similar to the one already observed for the Cu(100) surface. The filling of the LUMOs is a direct consequence of the strong molecule-metal interaction. As already found for NiTPP/Cu(100), for NiTPP/Cu(110) HOMO and HOMO-1 change their energetic order and, for this reason, HOMO-1, rather than the HOMO, is at the origin of the third feature at 1.75 eV BE. This feature, for the CoTPP molecules, has not been observed. Probably, the energy position of this orbital is slightly shifted towards higher BEs, making it difficult to be resolved, due to the strong signal from copper *d* states dominating in this BE regions. Similarly to NiTPP (CoTPP)/Cu(100), we did not measure any contribution of the LUMO+2 in the μ-ARPES maps, for both Ni and Co porphyrins.

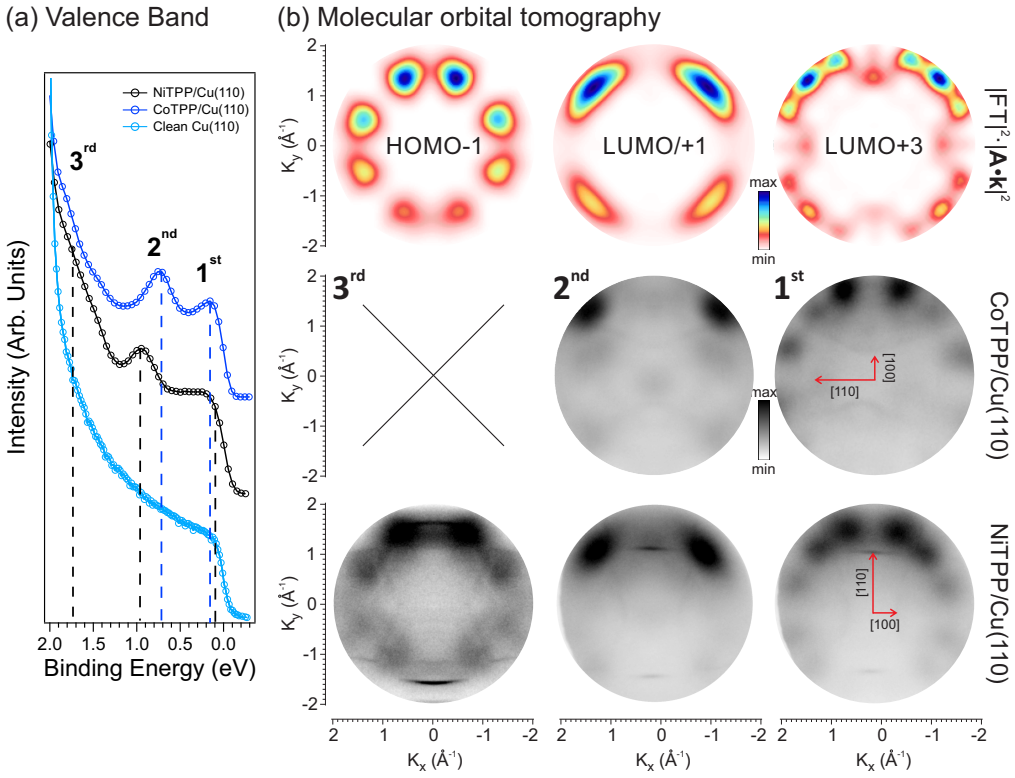

Figure 6.2: (a) Angle-integrated valence band for clean Cu(110), NiTPP/Cu(110) and CoTPP/Cu(110). (b) Comparison between the μ-ARPES measured patterns of CoTPP/Cu(110) (middle row), NiTPP/Cu(110) (bottom row) and the correspondent calculated $|\mathrm{FT}|^2$ of the molecular orbitals, multiplied by the square of the polarization factor $|\mathbf{A}\cdot\mathbf{k}|^2$ (top row). The crystallographic directions are indicated in the experimental momentum maps, the NiTPP molecules were deposited on the same Cu(110) rotated by 90°. The angle-integrated valence band and all the μ-ARPES were taken at $h\nu = 27$ eV.

The presence of the LUMO+3 molecular orbital below E_F was not predicted by previous DFT calculations on the CoTPP/Cu(110) system [48], which show only a partial filling of the almost degenerate LUMO and LUMO+1 and a complete occupation of the Co d_{z^2}. The latter, according to the authors, is responsible for the lack of the core structure in their STM images. However, the massive charge transfer, taking place at the molecule-metal interface, was not properly treated: our finding reveals that the orbitals, which have been involved in the charge transfer are indeed not only LUMO and LUMO+1 but also LUMO+3. These orbitals, in the gas-phase, are mostly localized on the macrocycle, while the first MO possessing a strong *d* character are HOMO and, mostly, HOMO-4. The last two are not experimentally observed in the valence band close to E_F. The good agreement between simulated and measured μ-ARPES patterns also suggests that the spatial charge distribution of the LUMO/LUMO+1 and LUMO+3, calculated for the molecule in gas-phase, is almost preserved upon CoTPP (NiTPP) adsorption. The reason of the discrepancy

in the MO alignment between the present and previously published works [48], may lie in the DFT approximation used. While HSE hybrid functionals have been employed, Donovan and co-workers used the generalized gradient approximation (GGA), which has already been proved to be unreliable in determining the energy level alignment. This is a clear example, which shows that MOT can be used as a very suitable technique to test different theoretical approximations, helping to choose the most reliable one.

Beside the energy level alignment, we can exploit the *sp* copper band features present in the μ-ARPES maps for determining precisely the orientation of molecule with respect to the high symmetry directions of the substrate. The azimuthal rotation of the molecule, giving the best agreement between the calculated $|\mathrm{FT}|^2$s and the experimental momentum maps, is $\pm$ 37° with respect to the [110] direction. This is the angle between the N-M-N axis (M= Ni, Co) and the [110] direction, as indicated in figure 6.3. Unfortunately, without further calculations of the relaxed adsorption structure, we cannot specify the relative orientation of the molecule with respect to the unit vectors of the ordered layer. Taking into account the LEED and μ-ARPES data, we propose an adsorption model, which is shown in figure 6.3. This model is valid for both NiTPP and CoTPP on Cu(110). The porphyrin adsorption configuration used is the one calculated in ref. [48] for CoTPP/Cu(110). We assigned the $-37°$ and $+37°$ azimuthal rotations to A and B domains, respectively. We would like to note that MOT does not require any preliminary knowledge about the azimuthal orientation of the molecule and it is not influenced by topographic features produced from the peripheral substituents, which may affect the interpretation of STM images.

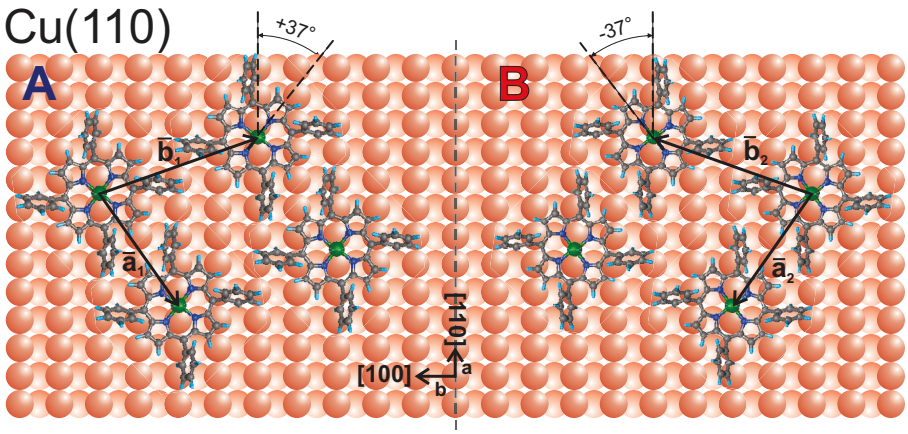

Figure 6.3: Proposed adsorption model valid for both CoTPP and NiTPP deposited on Cu(110). The two rotational domains, mirrored with respect to the [110] direction, are labeled with A and B, respectively. The azimuthal orientation of the molecules is specified in each domain

6.3 NiTPP and CoTPP on Ag(110)

In the previous sections we only considered porphyrins deposited on copper surfaces, where the molecule-metal interaction is strong and leads to a notable charge transfer into the organic film. We also showed that the electronic properties of these interfaces can be successfully characterized by means of molecular orbital tomography. Now, we would like to apply MOT to NiTPP (CoTPP) molecule deposited on a less reactive surface, Ag(110). The aim of this section is to determine the energy level alignment of NiTPP and CoTPP upon adsorption as well as studying the charge transfer phenomena between the organic film and Ag surface. About 1 ML of NiTPP (CoTPP) was grown on Ag(110) using the procedure described in chapter 4. The LEED patterns of NiTPP/Ag(110) and CoTPP/Ag(110) are shown in figure 6.4. The sharpness of the resulting diffraction patterns prove that both molecules form long range ordered domains on the Ag(110).

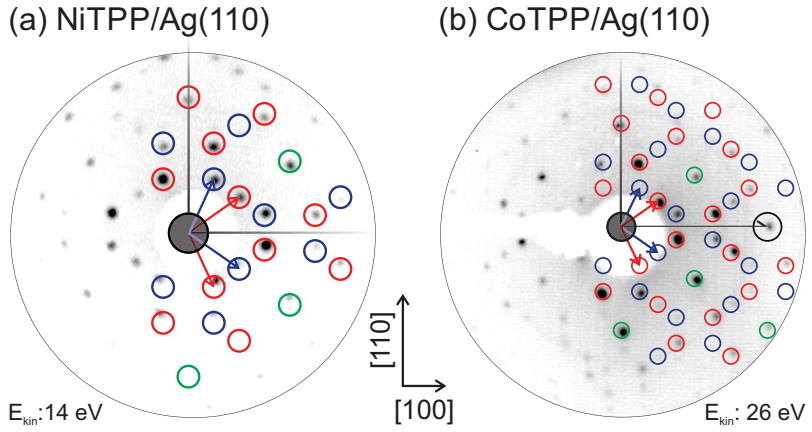

Figure 6.4: (a) LEED pattern of NiTPP deposited on Ag(110), taken at E_{kin}: 14 eV. (b) LEED pattern of CoTPP on Ag(110) taken at E_{kin}: 26 eV. The simulated diffraction patterns are superimposed to the experimental ones. Red and blue circles mark diffraction spots belonging to the two mirrored domains. Green circles, instead, highlight the common spots to the two structures. The substrate first order diffraction spots are located outside, or almost at the edge, of the probed Ewald sphere and indicated by the black arrows.

We carried out LEED pattern simulations (superimposed to the experimental ones in figure 6.4) which allowed to determine size and orientation of the unit cell. Both molecular overlayers have the same lattice structure: two rotational domains, mirrored along the high symmetry directions and commensurate with the Ag substrate. These two domains are described by the following matrices:

$$A = \begin{bmatrix} 2 & 3 \\ 4 & -2 \end{bmatrix} \qquad B = \begin{bmatrix} 2 & -3 \\ 4 & 2 \end{bmatrix}$$

Even for this surface, as already observed for Cu(110), the unit cell is not square and its vectors, separated by an angle of 100°, are 13.5 and 14.2 Å long. The present lattice structure slightly

differs from the one measured for H_2TPP and H_2TPPNH_2 on the same surface [51]. The NiTPP (CoTPP) overlayer on Ag(110) has a molecular density ∼20% higher than the one formed on Cu(110). A more detailed model of the molecular arrangement on the Ag(110) will be presented in the following.

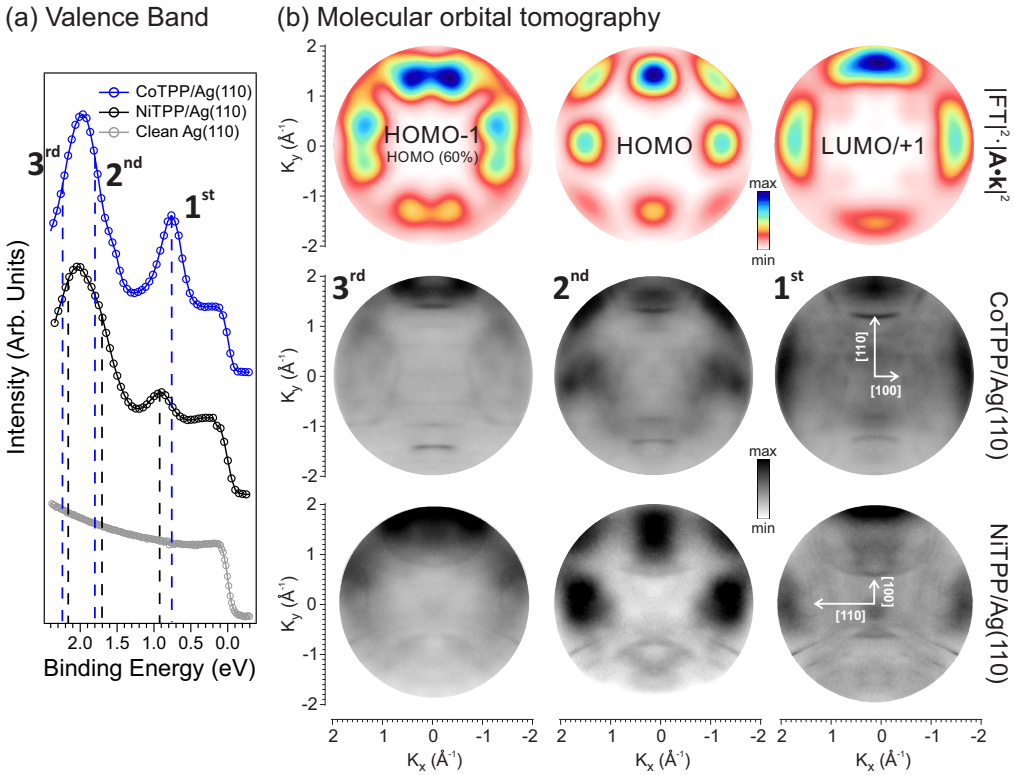

Figure 6.5: (a) Angle-integrated valence band for clean Ag(110), NiTPP/Ag(110) and CoTPP/Ag(110). (b) Comparison between the μ-ARPES measured patterns of CoTPP/Ag(110) (middle row), NiTPP/Ag(110) (bottom row) and the correspondent calculated $|FT|^2$ of the molecular orbitals, multiplied by the square of the polarization factor $|\mathbf{A}\cdot\mathbf{k}|^2$ (top row). In the experimental maps, the sharp inner features are related to the *sp* band of the copper surface. The crystallographic directions are indicated in the experimental momentum maps, the NiTPP molecules were deposited on the same Ag(110) rotated by 90°. The angle-integrated valence band and all the μ-ARPES were taken at $h\nu = 27$ eV.

Figure 6.5a shows angle-integrated valence band of the clean Ag(110) substrate (light blue line), NiTPP/Ag(110) (black line) and CoTPP/Ag(110) (blue line). The valence band of the clean silver is dominated by the signal from the *sp* band and has a featureless plateau up to 3 eV below the Fermi level. Both NiTPP/Ag(110) and CoTPP/Ag(110) spectra, instead, show two prominent features at BE values of 0.92 eV, 1.9 eV (NiTPP) and 0.78 eV, 2.0 eV (CoTPP). Angle-resolved photoemission performed at the valence band reveals that there are two well-separated contributes to the peak at higher BE located at about 1.7 eV and 2.2 eV (NiTPP/Ag) and 1.8 eV and 2.2 eV

(CoTPP/Ag). These BE*s* correspond to the maximum of intensity of each molecular feature in the μ-ARPES patterns. All the positions mentioned, for both NiTPP and CoTPP, are marked in figure 6.5a (black and blue dashed lines). The correspondent momentum maps, measured at the BEs indicated above, are shown in figure 6.5b (bottom and middle rows).

Within the MOT approach, the $|FT|^2 s$ were obtained from the MOs calculated starting from the Kohn-Sham eigenstates of a gas-phase NiTPP molecule. As mentioned in section 5.3.2, using the calculated adsorption geometry of the molecule on the surface, rather than the gas phase geometry, would result only in small differences in the frontier orbitals (up to LUMO+3 and down to HOMO-2) since the charge is mostly located on the macrocycle. Since the energy alignment is unknown *a priori*, we assumed that LUMO and LUMO+1 remain degenerate upon adsorption. In the gas-phase, also HOMO and HOMO-1 are close in energy ($\sim$ 100 meV) and for this reason we took into account also a possible overlap between the two in the $|FT|^2$s. Finally, the molecules might have a different azimuthal orientation within each domain that has to be considered as well. Starting from these assumptions, in figure 6.5b (top row) we show the simulated $|FT|^2$s which better resemble the experimental μ-ARPES. Based on the excellent agreement between experimental data and theoretical simulations, we identified the molecular features in the valence band spectrum. The conclusions drawn here are valid for both NiTPP and CoTPP. The peak closer to E_F is assigned to the degenerate LUMO and LUMO+1. The two components contributing to the second peak are, starting from the one at lower BE, HOMO and HOMO-1, respectively. In particular, HOMO-1 and HOMO are so close in energy that the former cannot be resolved independently from the latter. For this reason, in order to improve the agreement between measured and simulated patterns, we considered a 60% contribution of the HOMO orbital to the $|FT|^2$ HOMO-1.

The present data show that the gas-phase LUMO and LUMO+1 become occupied upon adsorption of NiTPP and CoTPP on silver, suggesting a charge transfer scenario between molecules and the metal substrate. The peak assigned to the ionization of the LUMO/LUMO+1, in figure 6.5a, was already observed, although shifted by $\sim$ 100 meV, towards E_F, for CoTPP molecules deposited on Ag(111) [16, 52, 7]. The energy shift is probably related to the different adsorption site of the TPP between (110) and (111) surface. To further support this statement, it was demonstrated that, in case of Ag(111), where the CoTPP lattice is not commensurate with the substrate, the BE position of the molecular states is influenced by the CoTPP-Ag distance [50]. At first, the peak in the CoTPP/Ag(111) valence band was attributed to the interaction between the Co d_{z^2} orbital with the Ag substrate [16]. However, Further STM studies proved that this orbital is also delocalized over the macrocycle and arises from the interaction between the Co and the N π states *via* the Co d_{xy} and d_{yz} states [50]. In their work, Auwärter and co-workers claim that this orbital is the HOMO of the CoTPP. Clearly, on Ag(110) the situation differs because our MOT measurements prove that the state at 0.78 eV arises from the occupation of the gas-phase degenerate LUMO/+1. Moreover, this orbital has almost no Co *d* character, at least in the gas-phase. Since the $|FT^2|s$ reproduce well the molecular orbitals in the μ-ARPES patterns, we assume that upon absorption

this remains true and no notable charge redistribution occurs. The molecule-substrate interaction is thus mediated by the orbital located on the macrocycle, which becomes occupied due to the charge transfer from the substrate.

The silver *sp*-bands, clearly visible in the μ-ARPES maps (see fig. 6.5), are used as a reference to determine the absolute rotation of the molecule with respect to the substrate high symmetry directions. This information, together with the size and orientation of the unit cell determined from the LEED data, allows us to construct the adsorption model sketched in figure 6.6 valid for both CoTPP and NiTPP. We found that one of the two N-M-N (M= Ni, Co) axes is rotated $\pm$ 38° with respect to the [110] direction, as indicated in fig. 6.6.

As already mentioned, MOT does not provide the molecular orientation with respect to the basis of the unit cell. For this reason we tentatively assign the -38° and +38° to A and B, respectively. This configuration favors the T-type interaction (see sec. 2.2.1) between the phenyl groups of neighboring porphyrins. However, without further topographic measurements or theoretical calculations we cannot directly prove this assignment. The latter is also mandatory in order to calculate the molecular adsorption conformation, in figure 6.6 NiTPP gas-phase one was used.

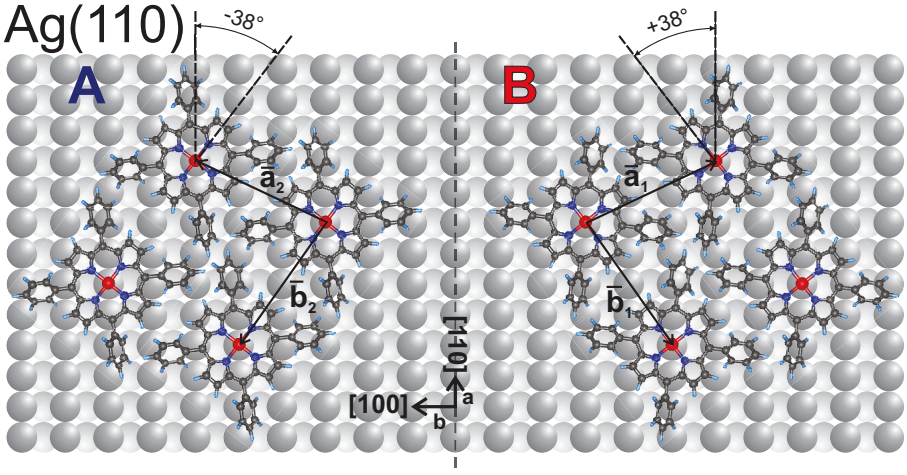

Figure 6.6: Proposed adsorption model valid for both CoTPP and NiTPP deposited on Ag(110). The two rotational domains, mirrored with respect to the [110] direction, are labeled with A and B, respectively. The azimuthal orientation of the molecules is specified in each domain. The adsorption geometry is the one the gas-phase NiTPP.

6.4 Conclusions

In this chapter we studied the energy level alignment of the NiTPP and CoTPP molecular orbitals upon adsorption on two different substrates: Cu(110) and Ag(110). In the former, the molecular electronic structure is similar to the one observed for NiTPP and CoTPP on Cu(100). Even though slightly shifted in BE*s* position, LUMO/LUMO+1 and LUMO+3 orbitals remain occupied. This shift can be explained by the molecular adsorption site: hollow for the Cu(100) surface (see chapter 5) and short-bridge for Cu(110) [48]. The situation drastically changes when CoTPP and NiTPP are deposited on Ag(110). LUMO+3 is no longer occupied but the molecule-metal interaction, although weakened, results in the filling up of the degenerate LUMO and LUMO+1. A similar feature, appearing upon the deposition of CoTPP on Ag(111) was already observed but it was attributed to the HOMO of the molecule. In conclusion, molecular orbital tomography allowed us to determine precisely the energy level alignment of the frontier orbitals upon absorption on Cu and Ag surfaces without demanding calculations of the full interface (molecule + metal). Also the azimuthal orientation can be precisely determined, making MOT a complementary technique to study molecular assembly on metal substrates.

Chapter 7

Functionalization of NiTPP/Cu(100) by NO adsorption

7.1 Introduction

The controlled functionalization of an organic layer offers a variety of different applications in the field of gas sensors [154] and novel catalysts [155]. In this context metalloporphyrins (MTPP) and phthalocyanines received particular attention. In case of MTPP, depending on the desired electronic, magnetic and reactivity properties, a different type of metal atom can be easily incorporated in the macrocycle [71]. Moreover, these properties can be further tuned by ligand coordination of small molecules (O_2 [156], CO [73], NH_3 [38] and NO [8]) to the incorporated metal ion. The advantage of using porphyrin or phthalocyanine films is that they are thermally very stable and they form well-ordered self-assembly on many noble metal surfaces as demonstrated in the previous chapters.

When deposited on ferromagnets, MTPPs may or may not magnetically couple with the substrate [65, 69]. This coupling can be turned "on/off" by a "chemical switch" [64] induced by external ligands, such as NO [8] or NH_3 [38]. It is generally accepted that these molecules bind in *trans*-position to the metal center, leading to the so-called *trans*-effect [52], which quenches or enhances the magnetic moment at the ion metal center [64]. However, this configuration is not the only possible ligand mechanism, in fact, recently, it was demonstrated that at low temperatures, two carbon monoxide molecules can bind on a single porphyrin in *cis*-carbonyl geometry [72]. As will be discussed in the present chapter, this bonding scheme may occur also upon NO co-adsorption on the nickel tetraphenyl porphyrin deposited on Cu(100). Here, we apply a comprehensive multi-technique approach including X-ray photoemission spectroscopy (XPS), near edge absorption fine structure (NEXAFS) and scanning tunneling microscopy (STM) to extend our knowledge on the absorption geometry of the $(NO)_n-$NiTPP/Cu(100) complex.

7.2 LEED and STM

NiTPP molecules were deposited on Cu(100) following the well-established procedure described in chapter 4. Close to the 1 ML regime, sharp diffraction spots were observed, indicating the existence of long-range order of the NiTPP film across the surface. The corresponding low energy electron diffraction (LEED) pattern is shown in figure 7.1a. The substrate symmetry leads to the formation of two rotational domains, mirrored with respect to the [100] direction and described by the integer matrices: (4,3/-3,4) and (3,4/-4,3) (for details see chapter 5.2). The simulated LEED spots are marked in fig. 7.1a. Figure 7.1b shows the LEED pattern of the NiTPP/Cu(100) exposed to 4000 L of NO at room temperature. Comparing figure 7.1a and 7.1b, we note only minor changes after NO exposure: a weakening of the diffraction spots and a slight increase in the background. Therefore, we conclude that the size and orientation of the NiTPP unit cell does not change upon exposure of the organic film to NO. On the contrary, the CoTTP molecules deposited on Ag(111) behavior differently upon NO exposure. There, CoTPP increases its unit cell by the 40% in order to accommodate NO molecules within the layer [157] and changes its azimuthal orientation respect to the substrate and the unit cell becomes oblique.

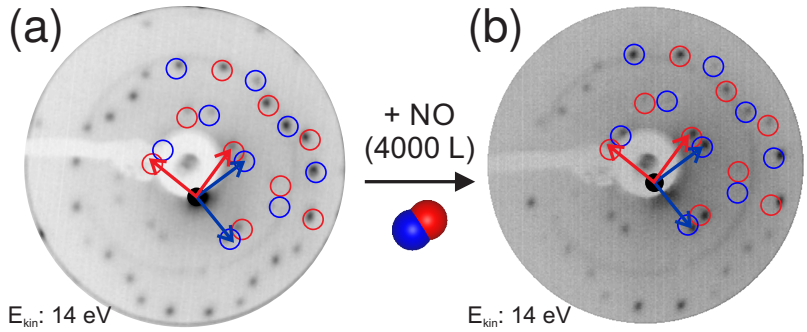

Figure 7.1: LEED pattern of Ni-TPP/Cu(100) before (a) and after (b) exposure to the NO (4000 L). The simulated structure is superimposed: blue and red spots correspond to A and B domains respectively. Both images were acquired at $E_{kin} = 14$ eV.

Another insight on the NO-NiTPP bonding mechanism is provided by high resolution STM measurements of the NiTPP/Cu(100) surface performed at different NO doses, from few hundreds to 2050 L. The molecular film was exposed to NO at RT in the experimental chamber, then it was transferred and cooled down to 4.3 K in the STM experimental chamber. The NiTPP coverage used in all the STM experiments was 0.5 ML. NO exposure up to 900 L does not change the appearance of the NiTPP film. On the bare copper surface, instead, small protrusions, which may be related to NO, N or O species, are visible already after 100 L. Major changes in the NiTPP film appearance start above NO dose of 900 L. The corresponding STM images taken at incremental NO doses are shown in figure 7.2. At 900 L, almost circular protrusions (circled in black) appear now at the center of the NiTPP replacing the dark holes, previously attributed to Ni atoms at the

center of the macrocycle (see sec. 5.2). We note also that the number of these protrusion increases with increasing NO dose. Therefore, we associate them to the nitric oxide bound to the Ni atoms of the porphyrin molecule. At dose of 2050 L, not all the Ni atoms have the NO attached.

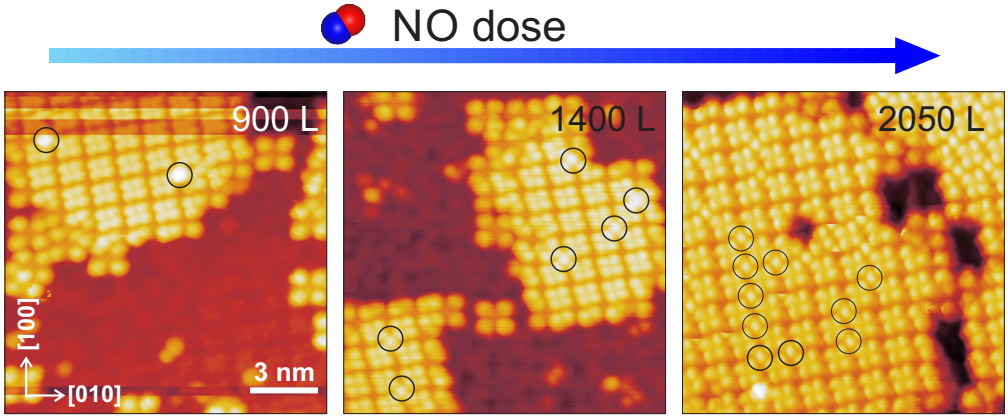

Figure 7.2: Series of STM images of the NiTPP/Cu(100) film taken at different NO exposures, from 900 to 2050 L. Almost circular protrusions appear at the center of NiTPP, their number increases at higher NO doses. Some of them are circled (black line). STM image parameters: V_b = -2.0 V, I_t = 0.1 nA, image size 14.4x14.4 nm^2. T = 4.3 K.

It is also worth mentioning that some of these protrusions are removed by the tip while it is scanning the surface. This can be noticed by comparing the forward and backward STM scans, where, after the transit of the tip, some of the features related to NO disappear.

The high resolution STM image of the NiTPP film exposed to 2050 L of NO is shown in figure 7.3. The protrusions identified above are pointed by black arrows. They have an almost round shape, slightly elongated in the vertical direction. Surprisingly, another feature, pointed by a white arrow, becomes now resolvable. It is made by four asymmetric lobes and it is also located at the porphyrin center. This adsorption configuration is less common than the other and it almost disappears for NO doses greater than 2050 L (data not shown). We therefore conclude that there are at least two different adsorbed NO species bound to the NiTPP.

We remind that, due to the strength of the molecule-substrate interaction (see chapter 5), the phenyl ligands are strongly tilted upwards, preventing the macrocycle to be resolved by the STM tip. To our knowledge, in the literature there are no STM studies on porphyrins exposed to nitric oxide in such a distorted conformation. The only studies available, which are useful for comparison, concern CoTPP films grown on Ag(111) [73] and Au(111) [158], subsequently exposed to nitric oxide. Also in those structures a round protrusion is observed in the center of the porphyrin upon NO exposure. It is associated to a tilted NO molecule bound to the metal ion of the TPP core. It has been demonstrated that this round shape arises from the fast (compared to the STM acquisition time) precession motion of a tilted NO molecule [158]. The same effect was observed also for a carbon monoxide molecule that binds to CoTPP in the *trans*-position. Instead,

the presence of two CO molecules bound to the TPP metal center, in *cis*-dicarbonyl coordination, "freezes" this motion [72].

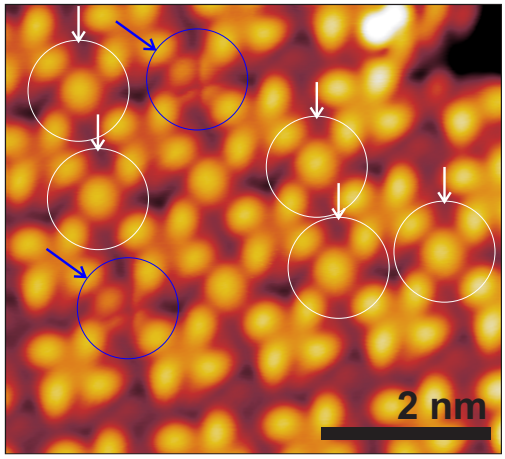

Figure 7.3: High resolution STM image of the NiTPP/Cu(100) film after NO exposure of 2050 L. Two kind of protrusions are now visible at the Ni atom position: one almost circular (pointed by the blue arrow) and the other composed by four asymmetric lobes (white arrow). STM image parameters: V_b = -2.0 V, I_t = 0.1 nA, image size 5.3x5.9 nm^2. T = 4.3 K.

However, only on these bases, we cannot unequivocally assign the two different features observed in figure 7.3 to the *trans*-nitrosyl or *cis*-dinitrosyl adsorption configurations. Further theoretical calculation and STM simulation will be needed to clarify this point.

No changes in the NiTPP azimuthal orientation are observed upon NO exposure and there are no evidences of the NO co-adsorption on copper within the porphyrin array, as reported instead for (NO)-CoTPP/Ag(111) system [157].

7.3 NEXAFS, XPS and UPS

The molecular conformation, upon exposure to NO, can be studied by following the changes which occur in the angle-dependent NEXAFS spectra. We focus our attention on two aspects: the absorption geometry of the two moieties of NiTPP, namely the phenyl ligands and the porphyrin macrocycle, and the charge state of adsorbed NO molecules. In figure 7.4 we compare the C and N K-edges, and Ni L_3-edge NEXAFS spectra of NiTPP/Cu(100), taken before (bottom) and after (top) exposure to NO, with *p* and *s* polarizations of the incoming synchrotron light.

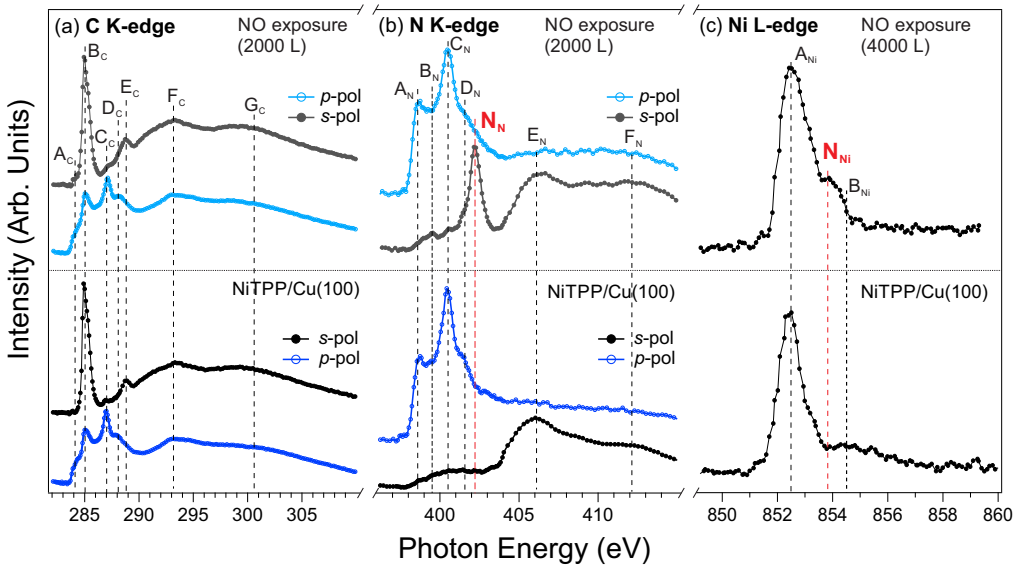

Figure 7.4: Angle-dependent NEXAFS spectra taken at the K-edges of carbon (a), nitrogen (b) and L-edge nickel (c) before (bottom) and after (top) NO exposure of NiTPP deposited on Cu(100). Main transition lines of the absorption edge are labeled for each element.

A detailed analysis of the NEXAFS spectra of the pristine NiTPP/Cu(100) interface is carried out in sections 5.2.2 and 5.3.3. Regarding the carbon K-edge (fig. 7.4a), $A_C \rightarrow E_C$ resonances are associated to transition of core level electrons into π^*, F_C and G_C, instead, into σ^*. While A_C (283.9 eV) is assigned to the macrocycle, B_C ($\sim$ 285 eV) mainly originates from the four phenyl ligands [37, 159]. The intensity dependence on the light polarization (*s*-pol *vs.* *p*-pol) indicates that, before dosing NO, the NiTPP macrocycle is oriented parallel to the Cu(100) surface. The phenyl groups, instead, are tilted with a steep angle respect to the surface ($\sim$70°). After the NiTPP film has been exposed to 2000 L of NO ($\sim$ 50 min at $5 \cdot 10^{-7}$ mbar), the residual A_C intensity in the *s*-pol spectrum suggests a puckering and/or tilting of the macrocycle moiety, as already observed for NO-MTPP/Ag(111) and NO-MTPP/Cu(111) complexes (M = Fe, Co) [52, 73]. Conversely, no significant changes are seen in the B_C polarization dependence before and after exposure to NO,

meaning that the adsorption configuration of the phenyl substituents remains almost unaffected.

In N K-edge NEXAFS spectra of the pristine NiTPP/Cu(100) (fig. 7.4b bottom) the features $A_N \rightarrow D_N$ correspond to the excitation of 1*s* electrons of the macrocycle nitrogen atoms to the π^* resonances, while the broad E_N and F_N are assigned to σ^* resonances. The π^*/σ^* ratio between spectra measured at two polarizations (*s* and *p*) supports the previously discussed flat adsorption geometry of the macrocycle ring of pristine NiTPP molecular arrays formed on the Cu(100) substrate.

The intensity variation of A_N ($1s \rightarrow$ LUMO) with respect to C_N ($1s \rightarrow$ LUMO+4/+8) [37], before and after NO adsorption, reflects the changes in the electronic structure in the NiTPP film after the formation of the $(NO)_n-$NiTPP complex. In particular, the A_N intensity is increasing upon NO adsorption on the NiTPP film. This trend suggests a partial quenching of the electron charge transfer into the NiTPP. This interpretation is further supported by analysis of the valence band photoemission spectra, which will be discussed below.

Upon the NO adsorption (fig. 7.4b top), B_N and C_N peaks appear also in the *s*-pol spectrum, further supporting a puckering/tilting of the NiTPP macrocycle. Moreover, a new resonance (N_N) is seen at 402.2 eV, which is in agreement to previous NEXAFS measurements on the NO molecule adsorbed on a porphyrin layer [132]. The energy position of this resonace is shifted to a higher photon energy by 2.5 eV comparing to the same transition in the adsorption spectrum of NO in the gas-phase (399.7 eV) [160]. This energy shift can be explained in terms of hybridization and charge transfer between the NiTPP and NO orbitals [161, 132]. The presence of a single feature (N_N) in the N K-edge spectrum, related to the nitric oxide, suggests that most of the NO molecules are in the same electronic state.

The Ni L_3-edge NEXAFS spectra of the pristine and NO exposed NiTPP/Cu(100) interfaces are shown in figure (fig. 7.4c). Upon NO adsorption on NiTPP, the main peak, A_{Ni} at 852.5 eV becomes broader and a new feature, N_{Ni}, appears at ∼853.8 eV. The evolution of the Ni absorption spectrum upon NO adsorption can be assigned to a transformation from the metallic state to an nonzero oxidation state. The Ni valency in the latter state can be determined qualitatively by comparing the plot in Fig.1.2c (top) to the published XAS spectra from reference Ni compounds. In particular, the prominent shoulder at high photon energy points to a 2+ valency of Ni [137]. This is further supported by the similarity of the spectrum displayed in Figure 1.2 to that of $NiBr_2$ with very similar peak and shoulder positions [162]. This will be further supported by XPS data discussed later.

X-ray photoelectron spectroscopy has been employed to study the physical and chemical properties of $(NO)_n-$NiTPP complex. In order to clarify the influence of the NO ligand on the electronic structure of the coordinated Ni ion, we first discuss the NO-induced changes in the Ni $2p_{3/2}$ core level spectrum. Figure 7.5a (bottom) shows the Ni $2p_{3/2}$ core level spectrum of the pristine NiTPP self-assembly on Cu(100). The main peak (I_{Ni}) at BE of 853.15 eV (FWHM ∼1 eV) is assigned to the core level of the central Ni atom inside the porphyrin. This position, as discussed in section 5.3.3 is typical for the Ni atom in a formal zero oxidation state and it is in agreement

with previously published studies [133, 38]. After NO exposure, a new feature (II_{Ni}) arises at BE = 854.85 eV (see figure 7.5a top). Increasing the NO dose, this component grows, while I_{Ni} decreases with a similar rate. The II_{Ni} energy position corroborates the oxidation process of the nickel atom upon the co-adsorption of the NO molecules. By properly fitting the Ni $2p_{3/2}$ core level, we were able to carry out a semi-quantitative analysis of the spectra upon NO dosage. Comparing the Ni $2p_{3/2}$ spectra after an exposure of the NiTPP/Cu(100) film to 2000 and 4000 L NO, we found that about 50% and 73% of the NiTPP molecules interacts with the NO. Unfortunately, from this data set we cannot determine the NO coordination site on the Ni atom, *i.e.* if it is in the *trans*-mononitrosyl or *cis*-dinitrosyl position forming a (NO)−NiTPP rather than $(NO)_2$−NiTPP complex.

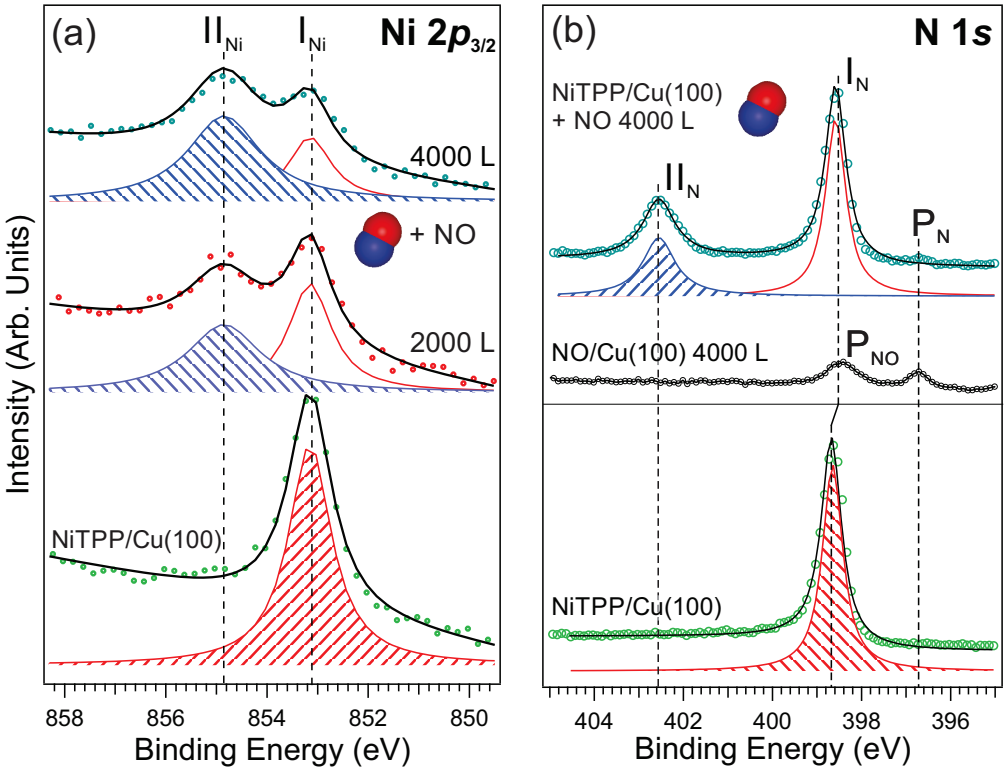

Figure 7.5: Ni $2p_{3/2}$ (a) and N 1*s* (b) core level photoemission spectra (experimental data and fits) of self-assembly NiTPP arrays on Cu(100) before and after adsorption of NO; N 1*s* region measured after the exposure of clean copper to 4000 L (black curve) also is shown on panel (b). Photon energies: Ni $2p_{3/2}$ $h\nu = 1000$ eV and N 1*s* $h\nu = 515$ eV.

In order to obtain a further insight on the NO coordination, we followed the changes in the N 1*s* core level of the NiTPP/Cu(100) film upon NO exposure. The corresponding XPS spectra are presented in the figure 7.5b. Before dosing NO, the N 1*s* spectrum shows a single sharp peak at

398.65 eV, marked I_N, which is assigned to the core level ionization of all four chemically equivalent nitrogen atoms of the nickel porphyrin (see also sec. 4.2). The BE of the peak is in good agreement with previously reported values for similar systems [107, 37]. Then, the molecular film was exposed to NO (4000 L) and a new maximum (II_N) appears at a BE of 402.55 eV (see fig. 7.5b top). At the same time I_N, shows a chemical shift of ∼70 meV to lower binding energies. We tentatively associate II_N to the nitrogen of the NO molecule which is bound to the Ni atom. Its BE differs by ∼2.65 eV from the one of NO chemisorbed on Ni(100) [163]. To further support this assignment, we also exposed the bare copper surface to NO under the same experimental condition. The measured spectrum is shown in figure 7.5b (black curve). Two components, P_{NO} and P_N peaked at BEs of 398.4 eV and 396.7 eV, respectively, contribute to the N 1*s* core level spectrum. P_{NO} is assigned to the NO molecule bound to the copper surface [164], while P_N is related to the atomic nitrogen resulting from the NO dissociation [165, 166]. The presence of nitrous oxide (N_2O) on the surfaces, which can be formed by the NO decomposition/recomposition, is excluded in the present case, because of the absence of the related peaks at 402 and 406 eV [165] (see fig. 7.5b). II_N was observed only for the NiTPP film exposed to NO and not for the bare copper, therefore this feature must be related to the NO-NiTPP interaction.

P_N, which is associated to the atomic nitrogen, has been measured also in the N 1*s* core level spectrum of NiTPP/Cu(100) exposed to NO. Its intensity changes as a function of the molecular coverage: depositing more NiTPP on Cu(100) leads to a decreasing of P_N, which almost disappears for $\geq$ 1 ML coverage. In other words, the organic film passivates the copper surface preventing the dissociative co-adsorption of NO molecules directly on copper. A residual contribution of P_N to the XPS signal can be seen also in figure 7.5b (top), suggesting NiTPP does not completely cover the entire surface.

We would like to note, that the NiTPP/Cu(100) upon NO adsorption shows a different behaviour respect to the CoTPP/Ag(111) interface exposed to NO [157]. Buchner *et al.* observed that, upon NO dosing, not only nitric oxide is bound to the Co ion of the porphyrin, but also the CoTPP unit cell expands in order to accommodate NO molecules within the organic layer. In the N 1*s* spectra three new components were reported at 399.3 eV, 400.6 eV and 402.4 eV. The former was associated to the NO interacting with CoTPP, the last two, instead, were assigned to NO adsorbed directly on the silver surface. The feature 402.4 eV in N 1*s* spectrum reported by Buchner *et al.* is close in energy to the II_N peak (see fig. 7.5b). However, the discussion of the N 1*s* core level spectra of NO adsorbed on the bare Cu or on the NiTPP film clearly excludes that II_N originates from the NO adsorbed directly on copper.

In order to discriminate between the two proposed NO adsorption mechanisms on the NiTPP, *i.e. trans*-nitrosyl or *cis*-dinitrosyl geometry, we determined the relative concentration of the different nitrogen species by fitting the N 1*s* core level spectra, using a Voigt lineshape. Knowing that four nitrogens contribute to I_N, the ratio between II_N and I_N peak areas can be used to estimate the amount of NO molecules interacting with the NiTPP. From the Ni 2*p* core level spectrum, we estimated that, after exposure to the 4000 L of NO, the 73% of the NiTPP molecules

are coordinated with NO. In this case, we would expect, for the mononitrosyl or cis-dinitrosyl geometry, the I_N/II_N ratio to be 5.5/1 or 2.5/1, respectively.

For the present data, we calculated an intensity ratio of about 2.6/1. We remind that this value is semi-quantitative estimation, because cross-section differences, scattering processes and the different geometry for the nitrogen in the porphyrin and in the NO molecule have not been considered. However, we can draw the conclusion that the mononitrosyl geometry alone cannot account for a so high concentration of NO adsorbed on the molecular film. We note also that the width of II_N (FWHM is 1.75 eV) may be due to both mononitrosyl or cis-dinitrosyl nitrogen species, which are contributing to the same peak.

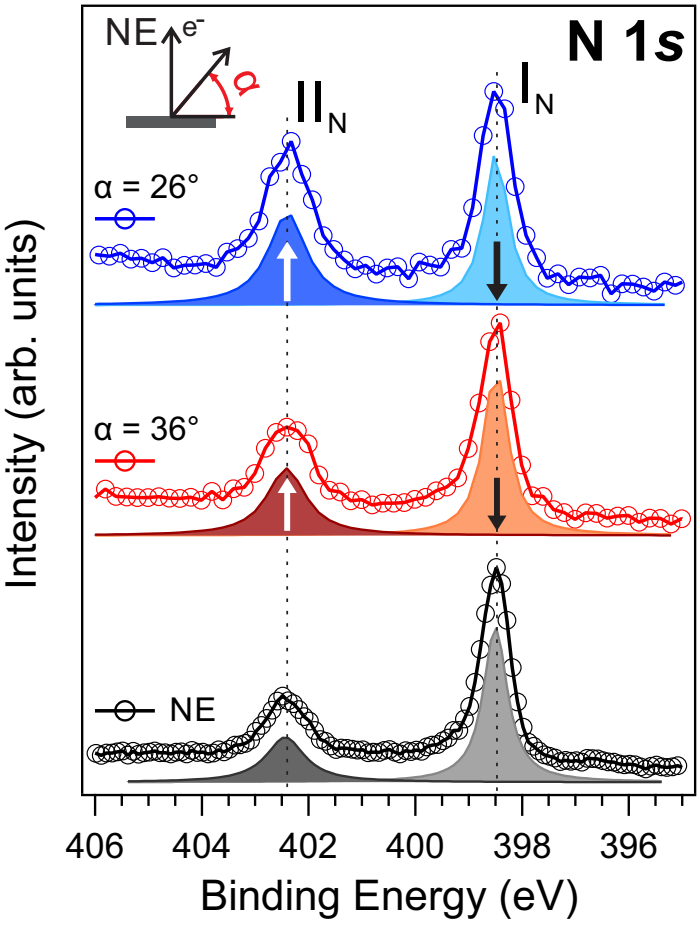

Figure 7.6: N 1*s* core level photoemission spectra (experimental data and fits) of self-assembly NiTPP arrays on Cu(100) after exposure to NO (4000 L). Spectra are taken different angles (α) between the analyzer and the sample, from 90° (NE) (bottom) to 26°(top), with respect to the surface plane. The corresponding α value is written near each spectrum. All spectra were acquired at $h\nu = 515$ eV. The geometry is sketched on the top left of the graph.

In order to elucidate the position of NO with respect to the nitrogens contained in the porphyrin macrocycle, we measured the N 1*s* core level of the NiTPP/Cu(100) film exposed to NO (4000 L) at different angles of photoemission. The resulting spectra are shown in figure 7.6. In normal emission (NE) geometry the I_N/II_N ratio is 2.6/1, while moving the analyzer off normal (at smaller α angles) it goes almost to 1/1. This measurement suggests that NO is placed higher than the porphyrin macrocycle with respect to the copper substrate. This excludes the adsorption of NO directly on the copper surface within the porphyrin network, further supporting the $(NO)_2-$NiTPP coordination mechanism.

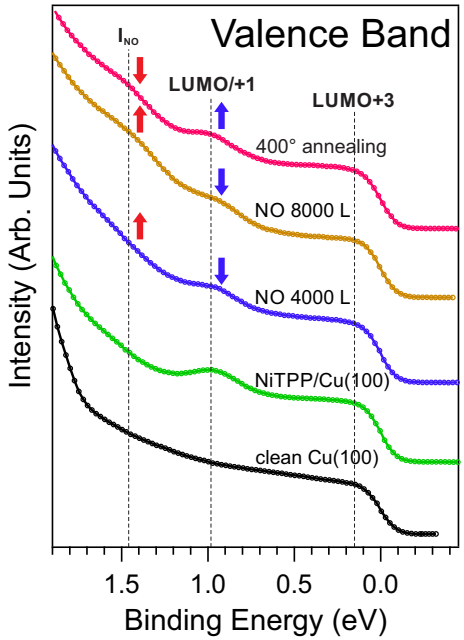

Figure 7.7: Angle-integrated valence band spectra of the clean copper surface (black curve), NiTTP/Cu(100) (green), NiTTP/Cu(100) film exposed to the 4000 L (blue) and 8000 L (yellow) of NO, post annealed surface up to 400° (violet). $h\nu = 27$ eV. LUMO/+1 and LUMO+3 and the feature at 1.45 eV induced by NO adsorption are marked in the figure. To facilitate the reader, arrows, pointing up(down)wards, indicate when the peak intensity is increasing (decreasing).

Figure 7.7 shows the valence band (VB) spectra for the clean copper surface and for the NiTPP/Cu(100) system before and after NO exposure of 4000 and 8000 L. The last curve is acquired after a post-annealing up to 400 °C of the NiTPP/Cu(100) surface, which have been previously exposed to 8000 L of NO. The bare copper and NiTPP/Cu(100) spectra are analyzed in detail in section 5.3.2. The two features at 0.15 and 0.98 eV, respectively, are assigned to the gas-phase LUMO/LUMO+1 and LUMO+3 molecular orbitals. As we have discussed before, they become partially populated because of a massive charge transfer taking place between copper and the NiTPP film, favored by the strong molecule-substrate interaction. Upon exposure to NO, a

third feature, I_{NO}, arises at 1.45 eV. Increasing the NO dose, its intensity increases as well, while LUMO/+1 and LUMO+3 peaks decrease, as one can see in figure 7.7. A post-annealing of the sample up to 400 °C, partially reverts, but I_{NO} does not completely disappear.

A similar behaviour was already observed for CoTPP/Ag(111) exposed to NO [52]: upon NO exposure a new peak at BE = 2.4 eV arises in the valence band, while the peak closest to the Fermi level, attributed to the Co-Ag interaction, is suppressed. We therefore attribute the I_{NO} peak to the NO molecules attached to the NiTPP. The decreasing of LUMO/+1 and LUMO+3 peaks suggests that the when NO binds to the NiTPP, the surface–molecule interaction is reduced because of the *trans*-effect [52, 7]. A post annealing of the sample at high temperatures stimulates the desorption of the NO molecules attached to the NiTPP, partially restoring the charge transfer between the porphyrin and the substrate.

7.4 Conclusions

In this chapter we studied the interaction between nitric oxide and a NiTPP film on the Cu(100) surface by means of state-of-the-art spectro-microscopic techniques, such as XPS, NEXAFS and STM. Against the common belief, we suggest the partial presence of a *cis*-dinitrosyl ligation mechanism between the NO molecules and the porphyrin layer, leading to the formation of $(NO)_2-$NiTPP complex already at room temperature.

Our findings are supported by both photoemission and STM experiments. In the N 1*s* core level, a new nitrogen species (II_N) appears upon exposure of NiTPP/Cu(100) to NO. The II_N intensity increases while increasing the NO dose. Surprisingly, from the area below II_N peak we estimate roughly two NO molecules per porphyrin. STM and XPS measurements excluded the co-adsorption of NO on the bare copper surface within the NiTPP layer, as happening, instead, for (NO)-CoTPP/Ag(111) [157]. The NO binds directly to the Ni atom at the porphyrin center, as suggested by Ni 2*p* core level analysis. This interpretation is corroborated by the NEXAFS spectra taken at the Ni L_3-edge. Nickel in NiTPP changes its oxidation state from zero to 2+: the net effect of NO adsorption is the weakening of the NiTPP-Cu interaction. Further insights on the electronic structure are given by the valence spectra taken before/after NO dose: the electron charge transfer from the copper surface to the porphyrin LUMOs, is reduced and a new peak, attributed to the NO-NiTPP interaction, appears. The system cannot be completely restored back to its initial state by stimulating the NO desorption with an annealing at 400 °C. The high resolution STM images confirm the photoemission data and report two different NO adsorption configurations of NO-NiTPP complexes upon NO dose.

Outlook

The organic semiconductors have a key role in the fast growing field of spintronics, where active manipulation and control of the electronic spin degres of freedom are of interest [62]. These systems are often investigated with element specific spectroscopic methods which probe the magnetic coupling between the organic and ferromagnetic films, such as X-ray magnetic circular dichroism. For example, Wende *et al.* showed that iron porphyrins deposited on ferromagnetic (FM) substrates (Ni and Co) ferromagnetically order already at room temperature [65]. Later on, similar results were also obtained for other metal porphyrin molecules and their derivatives [17, 64]. In most cases, an indirect magnetic exchange coupling mechanism, *via* the four nitrogen atoms of the porphyrin macrocycle, is responsible for this magnetic alignment [65].

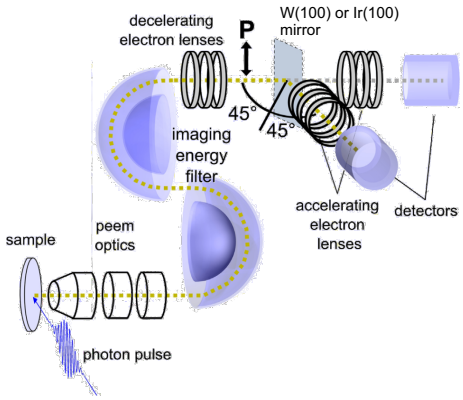

Figure 7.8: Experimental setup of the imaging spin filter installed at the PEEM microscope. Photoemitted electrons are decelerated and accelerated by electrostatic lenses before and after scattering at the W(100) mirror. Images are then collected at the detector in a 90° geometry. The quantization axis (**P**) is normal to the scattering plane. Reproduced from [167].

While XMCD probes the spin state of the transition metal within the molecule, it is not directly sensitive to the spin polarized charge distribution in the molecular orbitals (MOs) localized over the other light atoms, such as C, N and O.

On the other hand, molecular orbital tomography can access the full spatial charge distribution of the molecule. For this reason, providing MOT with spin sensitivity would be a breakthrough in order to directly measure the MO spin polarization. This can be achieved with a highly stable spin detector. Recently, the development of a novel 2D spin-filter made possible to perform spin resolved measurements (μ-ARPES and real space imaging) in a NanoESCA-based-design photoemission electron microscope [167, 168, 169].

This spin-filter is based on the spin-dependent specular electron reflectivity of a high Z single crystal with the large spin-orbit coupling and, so far, two scattering targets have been successfully tested for this purpose, namely the W(100) [167] and Ir(100) single crystals [169]. It is inserted

into the electron optical path immediately after the second HSA (see figure 7.8), where electrons which are entering in the spin-optics are decelerated from the pass energy to the scattering energy (E_{scatt}), in the [15,90] eV range. The incident angle of the electron beam on the target is 45°, with the spin quantization axis (**P**) normal to the scattering plane. The image information (either real or reciprocal space) is preserved upon the 90° specular reflection and projected onto a dedicated 2D detector.

The E_{scatt} dependence inherent to the spin polarized low energy electron reflectivity at the W(100) or Ir(100) crystals [170] is exploited to measure the spin polarization of the incoming photoelectron beam by acquiring two images at different E_{scatt}. This procedure can be applied to obtain quantitative information on the degree of spin polarization from both real [168] and reciprocal (μ-ARPES) [169] space PEEM images.

The described spin-filter set-up, equipped with a W(100) scattering target, has been recently installed at the NanoESCA beamline and it has been used for band structure studies of ultrathin ferromagnetic metal films, such as epitaxially-grown fcc cobalt on Cu(100) and FeNi alloy film on W(110). Spin-resolved μ-ARPES experiments on organic films have not been carried out yet.

In order to perform such measurements on a suitable organic substrate, the stability of the scattering target has to be improved. In fact, the W(100) surface is well-known to be reactive, often needing to be cleaned in order to preserve its spin-sensitivity. An upgrade of the spin filter has been planned: the tungsten target will be replaced with an iridium single crystal passivated by 1 ML of gold, which make the surface inert and able to last under UHV conditions for larger periods without being refreshed [169].

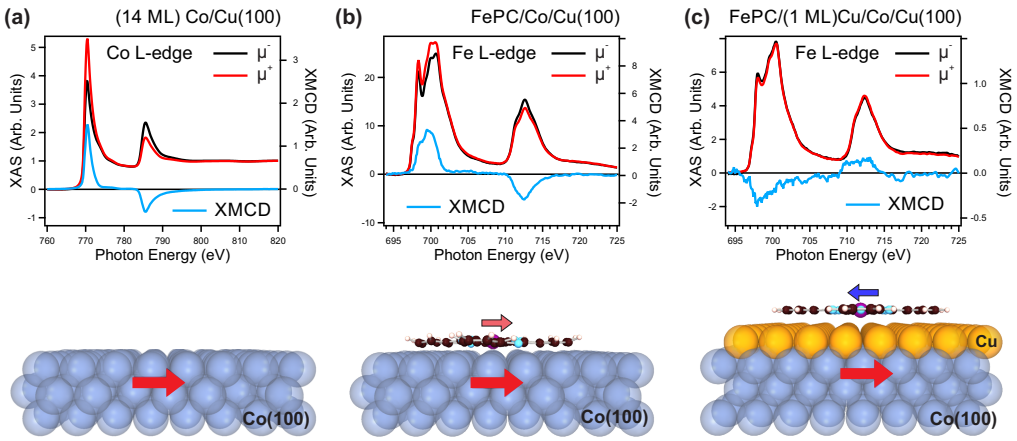

Figure 7.9: (a) XAS spectra of the bare Co/Cu(100) film acquired at the Co L-edge with circular polarized synchrotron light at the two opposite helicities (μ^+ and μ^-). The obtained dichroic signal, $(\mu^+ - \mu^-)/(\mu^+ + \mu^-)$, is plotted in the same graph (light blue curve). (b) (c) XAS spectra of FePC film deposited directly on Co/Cu(100) and (1 ML)Cu/Co/Cu(100) substrates, respectively. Spectra are acquired at the Fe L-edge for both μ^+ and μ^-. The resulting XMCD signals (light blue curve) are displayed on the respective graphs. During all the measurements the sample was taken at 80 K.

So far, we performed preliminary studies on two model systems which may become potential candidates for the first tests on spin-resolved molecular orbital tomography: a manganese-tetracyanoquinodimethane (TCNQ) magnetic network [171] and porphyrin or phthalocyanine film coupled to a FM substrate *via* a copper layer.

FePC was investigated on the (x ML)Cu/Co/Cu(100) substrate (x = 0-10 ML) and the magnetic coupling of the molecule/FM interface was studied by means of X-ray magnetic circular dichroism. A ferromagnetic coupling between FePC molecules (fig. 7.9b) and the underlying Co (fig. 7.9a) substrate is clearly established when molecules are directly deposited on the FM substrate. Interestingly the coupling is reversed for FePC/(1 ML)/Cu/Co/Cu(100) (see fig. 7.9c). On this perspective, spin-resolved MOT can provide a direct way to measure the spin polarized charge distribution in the molecular orbitals at the interface.

Conclusions

Porphyrins raised the attention of the scientific community because of their remarkable physical and chemical properties, which can be exploited to built organic-based device suitable for large-scale industrial applications. On this perspective, it becomes of fundamental importance to develop reliable models able to predict the device performances, especially those related to the charge-injection at the organic-metal interface, where chemical reactions, hybridization and charge transfer may take place.

In order to properly take into account these phenomena, advanced experimental techniques and sophisticated computational methods must be used. In this thesis, we combined multiple surface-science characterization tools with *ab-initio* density functional theory calculations to develop a consistent picture of the adsorption behavior and electronic structure of selected organic/metal interfaces.

The first model system chosen was the nickel tetraphenyl porphyrin molecule deposited on the copper (100) single crystal surface. In particular, the changes in the energy alignments of the molecular orbitals near the Fermi level, which occur upon adsorption on the metal substrate, has been studied by means of molecular orbital tomography. MOT confirmed the pronounced charge rearrangements leading to the occupation of the gas-phase LUMO/LUMO+1 and LUMO+3 molecular orbitals, which was suggested by hybrid functional DFT calculations. Moreover, from MOT results it was possible to accurately determine the azimuthal orientation of the molecule with respect to the high symmetry directions of the surface. This information cannot be retrieved from high-resolution STM images of the molecular layer because the macrocycle features are not accessible from the STM tip due to the NiTPP highly distorted adsorption geometry.

The present analysis was extended to the cobalt tetraphenyl porphyrin adsorbed on the same surface. MOT shows that replacing the Ni with the Co ion at the macrocycle center does not drastically change the resulting electronic properties. The molecule-substrate interaction is partially weakened when CoTPP and NiTPP are deposited on Ag(110). The absence of the LUMO+3 signature in μ-ARPES proves that this orbital is no longer occupied, but the charge transfer is not completely quenched since the momentum patterns related to the degenerate LUMO and LUMO+1 are still visible. LUMO/LUMO+1 give rise to a well-defined feature in the valence band spectrum, which was already observed in the literature for CoTPP deposited on Ag(111), but it was erroneously attributed to the molecular HOMO in a previous work. Notably,

MOT reveals the presence of two molecular orbitals, which contribute to the same valence band feature and cannot be resolved individually by angle-integrated methods.

Finally, the NiTPP/Cu(100) system was functionalized by exposure to nitric oxide. For the first time, the data suggest a *cis*-dinitrosyl ligation mechanism between the NO molecules and the porphyrin layer, leading to the formation of $(NO)_2-$NiTPP complex already at room temperature. This finding is supported by both XAS, XPS and STM experiments The net effect of NO adsorption on the electronic structure is the weakening of the NiTPP-Cu interaction. The charge transfer between the substrate and the organic film is reduced and a new peak, related to the NO-NiTPP complex, appears in the valence band. NO cannot be completely desorbed upon annealing of the NiTPP film up to 400 °C.

Overall, this thesis demonstrates the importance of combining different experimental techniques and computational methods in order to provide a consistent and robust description of the organic-metal interfaces.

Abbreviations

AES Auger Electron Spectroscopy

ARPES Angle Resolved Photoelectron Spectroscopy

BE Binding Energy

BF Bright-field

CNL Charge Neutrality Level

CoTPP Cobalt Tetraphenyl Porphyrin

DF Dark-field

DFT Density Functional Theory

DOS Density of States

EA Electron Affinity

FT Fourier Transform

FWHM Full-width at Half-maximum

GGA General Gradient Approximation

HOMO Highest Occupied Molecular Orbital

HSA Hemispherical Sector Analyzer

IDIS Induced Density of Interface States

IE Ionization Energy

KE Kinetic Energy

LEED Low Energy Electron Diffraction

LEEM Low Energy Electron Microscopy

LUMO Lowest Unoccupied Molecular Orbital

ML Monolayer

MO Molecular Orbital

MOT Molecular Orbital Tomography

MTPP Metal Tetraphenyl Porphyrin

NEXAFS Near Edge X-ray Absorption Fine Structure

NiTPP Nickel Tetraphenyl Porphyrin

PDOS Projected Density of States

PEEM Photoemission Electron Microscopy

PES Photoemission Electron Spectroscopy

RT Room temperature

SPELEEM Spectroscopic Photoemission and Low Energy Electron Microscope

STE Surface Trans Effect

STM Scanning Tunnelling Microscopy

SV Start Voltage

UHV Ultra High Vacuum

UPS Ultraviolet Photoelectron Spectroscopy

VB Valence Band

VL Vacuum Level

WKF Work Function

XAS X-ray Absorption Spectroscopy

XMCD X-ray Magnetic Circular Dichroism

XPD X-ray Photo-electron Diffraction

XPEEM X-ray PhotoEmission Electron Microscopy

XPS X-ray PhotoElectron Spectroscopy

Curriculum Vitae

Personal Data

Name	Giovanni Zamborlini
Address	Via Pellico 40,
	Fossalta di Portogruaro (VE), 30025, Italy
Email	g.zamborlini@fz-juelich.de
Date of Birth	27^{th} March 1989
Place of Birth	San Vito al Tagliamento (PN), Italy
Nationality	Italian

Education

02/2014-05/2017	Ph.D. work at Forschungszentrum Jülich (PGI-6)
	Advisor: Prof. Dr. Claus M. Schneider
09/2011-10/2013	Master Degree in Physics, University of Trieste
	Thesis: "Spectro-microscopic characterization
	of the Graphene/Ir(100) interface irradiated with Ar ions."
	Advisor: Prof. Giovanni Comelli
09/2012-02/2013	Erasmus Exchange student at Copenhagen University
09/2008-07/2011	Bachelor Degree in Physics, University of Trieste
	Thesis: "Metalation of Tetraphenylporphyrins
	by means of surface ad-atoms on Ni(111) and Fe(110)."
	Advisor: Prof. Alberto Morgante
2003-2008	Maturità Scientifica (Highschool diploma)

Publications and conference contributions

Publications

B. Casarin, A. Cian, Z. Feng, E. Monachino, F. Randi, G. Zamborlini, M . Zonno, E. Miniussi, P. Lacovig, S. Lizzit and A. Baraldi.
The thinnest carpet on the smallest staircase: the growth of graphene on Rh(533).
Journal of Physical Chemistry C, **118**, 6242 (2014).

A. Locatelli, G. Zamborlini and T. O. Menteş.
Growth of single and multi-layer graphene on Ir(100).
Carbon, **74**, 237 (2014).

T. O. Menteş, G. Zamborlini, A. Sala and A. Locatelli.
Cathode lens spectromicroscopy: methodology and applications.
Beilstein Journal of Nanotechnology, **5**, 1873–1886 (2014).

G. Zamborlini, M. Imam, L. L. Patera, T. O. Menteş, N. Stojić, C. Africh, A. Sala, N. Binggeli, G. Comelli and A. Locatelli.
Nanobubbles at GPa Pressure under Graphene.
Nano Letters, **15**, 6162-6169 (2015).

V. Feyer, M. Graus, P. Nigge, G. Zamborlini, R. G. Acres, A. Schöll, F. Reinert and C. M. Schneider
The geometric and electronic structure of TCNQ and TCNQ+Mn on Ag(001) and Cu(001) surfaces.
Journal of Electron Spectroscopy and Related Phenomena, 204, 125-131, (2015).

A. Sala, G. Zamborlini, T. O. Menteş and A. Locatelli.
Fabrication of 2D Heterojunction in Graphene via Low Energy N_2^+ Irradiation.
Small, 11, 5927–5931 (2015).

C. Africh, C. Cepek, L. L. Patera, G. Zamborlini, P. Genoni, T. O. Menteş, A. Sala, A. Locatelli and G. Comelli.
Switchable graphene-substrate coupling through formation/dissolution of an intercalated Ni-carbide layer.
Scientific Reports, 6, 19734 (2016).

L. di Mario, S. Turchini, G. Zamborlini, V. Feyer, L. Tian, C. M. Schneider, S. Rubini and F. Martelli.
Schottky barrier measurements on individual GaAs nanowires by X-ray photoemission microscopy.
Applied Surface Science, 386, 72-77 (2016).

G. Zamborlini, D. Lüftner, Z. Feng, B. Kollmann, P. Puschnig, C. Dri, M. Panighel, G. di Santo, A. Goldoni, G. Comelli, M. Jugovac, V. Feyer and C. M. Schneider.
Unexpected multi-orbital charge transfer at highly oriented organic/metal interfaces.
Accepted for publication, Nature Communications (2017).

M. Gehlmann, I. Aguilera, G. Bihlmayer, S. Nemšák, P. Nagler, P. Gospodarić, G. Zamborlini, M. Eschbach, V. Feyer, F. Kronast, E. Młyńczak, T. Korn, L. Plucinski, C. Schüller, Stefan Blügel and C. M. Schneider.
Direct observation of the band gap transition in atomically thin ReS_2.
Under review: Nano Letters (2017).

Talks

G. Zamborlini, V. Feyer, M. Graus, P. Nigge, R. G. Acres, A. Schöll, F. Reinert and C. M. Schneider.
The geometric and electronic structure of TCNQ and TCNQ+Mn on Ag(001) surface.
DPG, Berlin (DE), 18.03.2015.

G. Zamborlini, V. Feyer, P. Puschnig, D. Lüftner, B. Kollmann, C. Dri, Z. Feng, P. Umari, M. Marsili and C. M. Schneider.
A multi-technique approach in studies of NiTPP self-assembly on the Cu(100) surface.
Surface Science Symposium, St. Christoph am Arlberg (ÖS), 26.02.2016.

G. Zamborlini, V. Feyer, M. Jugovac, T.O. Menteş, P. Puschnig, D. Lüftner, C. Dri, Z. Feng and C. M. Schneider.
STM, LEEM and μ-ARPES studies of Ni-TPP self-assembly on Cu(100).
LEEM/PEEM 10, Monterey (USA), 14.09.2016.

Poster contributions

G. Zamborlini, V. Feyer, M. Graus, P. Nigge, R. G. Acres, A. Schöll, F. Reinert and C. M. Schneider.
The adsorption of TCNQ on the Ag(100) and Cu(100) surfaces: photoelectron momentum microscope mapping.
LEEM/PEEM 9, Berlin (DE), 15.09.2014.

G. Zamborlini, V. Feyer, M. Jugovac, C. Tusche, P. Puschnig, D. Lüftner, B. Kollmann, C. Dri, Z. Feng and C. M. Schneider.
Molecular Orbital Tomography @NanoESCA beamline.
PLESI 2016, Dresden (DE), 25.04.2016.

Erklärung

Hiermit erkläre ich, dass ich die vorliegende Arbeit selbstständig und ohne fremde Hilfe verfasst habe. Ferner habe ich außer den angegebenen Quellen keine anderen Hilfsmittel benutzt. Die dem Sinn oder Wortlaut nach entnommenen Textpassagen oder Abbildungen habe ich in jedem Einzelfall kenntlich gemacht. Dieser Dissertation geht weder ein erfolgloser Promotionsversuch voraus, noch wurde sie in einem weiteren Promotionsverfahren eingereicht. Abgesehen von den angegebenen Publikationen sind die Ergebnisse dieser Dissertation unveröffentlicht.

Diese Dissertation, die den Doktorgrad "Dr. rer. nat." anstrebt, wurde von Prof. Dr. C. M. Schneider betreut.

Jülich, 07/06/2017

Giovanni Zamborlini

Acknowledgments

This work would not have been possible without the assistance and contribution of many people. *In primis*, I want to thank my doctoral thesis advisor Prof. Claus M. Schneider, for giving me the opportunity to pursue PhD in his department. I thank him for the constant support, helpful discussions and guidance.

I would like to express my sincere gratitude to my supervisor Dr. Vitaliy Feyer, for the support he gave me during these three years and for all the things he taught me. I will always be indebted to him. I am also grateful to my colleague Matteo Jugovac for all the help he gave me during the experiments, for the good time we had together and mostly for being a trusted friend.

I cannot forget to mention Dr. Daniel Lüftner and Prof. Peter Puschnig for their invaluable theoretical support. Without them the results shown in this work could not been accomplished. I would like to thank also Dr. Zhijing Feng, Dr. Carlo Dri and Prof. Giovanni Comelli, for performing the STM measurements and for all the effort they spent drafting the manuscript. A special thanks go to Dr. T. Onur Menteş, for proofreading of this thesis and helpful discussions on the LEEM part and to Dr. Andrea Locatelli, Dr. Alessandro Sala and Dr. Francesca Genuzio, for being the best synchrotron neighbors one could have.

I want to express my gratitude to all my colleagues from Peter Grünberg Institut-6, especially to Pika, Christoph, Markus, Mathias, Ewa, Tristan and Christian, for creating a warm and friendly atmosphere at work. Last but not least I want to thank my parents, Anna Maria and Lorenzo, my brother Francesco, all my friends and my girlfriend Caterina, for their support during these years.

Finiti i ringraziamenti ufficiali e liberatomi dal peso di dover usare una lingua non mia, vorrei ringraziare nuovamente tutte quelle persone che in questi anni mi sono state vicine. Il mio ringraziamento più sentito va a Vitaliy, per tutto il tempo che abbiamo trascorso assieme alla beamline, per tutte le discussione, inutili e non, che abbiamo avuto e per quello che in questi anni mi ha trasmesso. Lo stimo sia come scienziato e soprattutto come persona, lavorare con lui è stato un onore ed un piacere e mi auguro che le nostre carriere non si discosteranno troppo. Gli sarò sempre riconoscente.

Il secondo della lista è Matteo. In questi anni è stato un collega meraviglioso che un grandissimo amico. Non è solo una delle persone più generose che conosca, ma anche una delle più disponibili. Abbiamo condiviso un sacco di cose sia dentro che fuori all'ambiente di lavoro e abbiamo costruito un rapporto basato sulla fiducia e il rispetto che spero vivamente possa durare anche in futuro.

Un grazie sentito va ai miei amici e colleghi Andrea, Onur, Francesca e Alessandro. Pur non dandolo a vedere, ho imparato e imparo un sacco di cose da voi. Tutti assieme siamo riusciti a creare un clima disteso e gioviale in un ambiente di lavoro che a volte sa complicarti la vita. Considero sia un enorme privilegio aver la possibilità di lavorare con persone alle quali vuoi bene e stimi.

Mi sento in dovere di ringraziare anche Lisa e Giuseppe, amici di lunga data, per esserci stati nei momenti di difficili, quando chi ti è amico davvero non si gira dall'altra parte facendo finta di nulla. Ne abbiamo passate tante assieme, abbiamo visto l'era punk, quella metallara, quella dark, quella paninara, quella dei finti ricchi, quella dei finti poveri, eppure siamo qui, invariati. Niente ci ha cambiato. Anche se la vita, per un motivo o per l'altro, a volte ci allontana, credo che i rapporti che veramente contano resistano al logorio.

Non voglio dimenticare Giulio, grandissimo amico e confidente. Durante questi anni abbiamo condiviso gioie e dolori, e molto spesso, li abbiamo entrambi annegati nel vino. È una delle persone con le quali ho sempre avuto e avrò un rapporto vero. Mi ricordero' sempre di quella volta che vicino a Roma, a Little Big Horn, capelli corti generale ci parlò all'università dei fratelli tutte blu che seppellirono le asce. Non fumammo con lui non era venuto in pace. Abbiamo imparato che al Dio degli inglesi non bisogna credere mai.

Non posso non esprimere gratitudine verso la mia famiglia: Anna Maria, Lorenzo e Francesco. Mi hanno permesso di intraprendere questa strada, mi hanno sostenuto e se sono arrivato fino a qui gran parte è merito loro. L'altra parte del merito va a Caterina, la mia compagna. Quelli passati assieme sono stati anni meravigliosi anche se non privi di difficoltà, non vedo l'ora di vivere assieme quelli che verranno. Per tutto quello che mi hai dato, per la calma che hai sempre saputo trasmettermi e per l'equilibrio che hai portato nella mia vita non finirò mai di ringraziarti. Quando mi chiederai "E adesso?" ti risponderò "È tutto ciò che avremo".

Dedico questa tesi ad Anna, Flavia e Dante.

Bibliography

[1] Yang, F., Shtein, M. & Forrest, S. Controlled growth of a molecular bulk heterojunction photovoltaic cell. *Nature Materials* **4**, 37–41 (2005). URL http://www.nature.com/nmat/journal/v4/n1/full/nmat1285.html.

[2] D'Andrade, B., Brooks, J., Adamovich, V., Thompson, M. & Forrest, S. White light emission using triplet excimers in electrophosphorescent organic light-emitting devices. *Advanced Materials* **14**, 1032–1036 (2002). URL http://dx.doi.org/10.1002/1521-4095(20020805)14:15<1032::AID-ADMA1032>3.0.CO;2-6.

[3] Adachi, C., Baldo, M. A., Thompson, M. E. & Forrest, S. R. Nearly 100% internal phosphorescence efficiency in an organic light-emitting device. *Journal of Applied Physics* **90**, 5048–5051 (2001). URL http://aip.scitation.org/doi/abs/10.1063/1.1409582.

[4] Sekitani, T. *et al.* A large-area wireless power-transmission sheet using printed organic transistors and plastic MEMS switches. *Nature Materials* **6**, 413–417 (2007). URL http://www.nature.com/nmat/journal/v6/n6/abs/nmat1903.html.

[5] Fahlman, M. *et al.* Experimental and theoretical studies of the electronic structure of poly(p-phenylenevinylene) and some ring-substituted derivatives. *Macromolecules* **28**, 1959–1965 (1995). URL http://dx.doi.org/10.1021/ma00110a033.

[6] Fahlman, M., Gebler, D. D., Piskun, N., Swager, T. M. & Epstein, A. J. Experimental and theoretical study of ring substituent induced effects on the structural and optical properties of poly(p-pyridylvinylene- phenylenevinelyne)s. *The Journal of Chemical Physics* **109**, 2031–2037 (1998). URL http://aip.scitation.org/doi/abs/10.1063/1.476717.

[7] Flechtner, K., Kretschmann, A., Steinrück, H.-P. & Gottfried, J. M. NO-Induced Reversible Switching of the Electronic Interaction between a Porphyrin-Coordinated Cobalt Ion and a Silver Surface. *Journal of the American Chemical Society* **129**, 12110–12111 (2007). URL http://dx.doi.org/10.1021/ja0756725. PMID: 17877358.

[8] Wäckerlin, C. *et al.* Controlling spins in adsorbed molecules by a chemical switch. *Nature Communications* **1** (2010). URL http://dx.doi.org/10.1038/ncomms1057.

[9] Droghetti, A. *et al.* Dynamic spin filtering at the Co/Alq_3 interface mediated by weakly coupled second layer molecules. *Nature Communications* **7** (2016). URL http://www.nature.com/articles/ncomms12668.

[10] Stadtmüller, B. *et al.* Unexpected interplay of bonding height and energy level alignment at heteromolecular hybrid interfaces. *Nature Communications* **5**, 1–7 (2014). URL http://www.nature.com/articles/ncomms4685.

[11] Deibel, C., Strobel, T. & Dyakonov, V. Role of the charge transfer state in organic donor–acceptor solar cells. *Advanced Materials* **22**, 4097–4111 (2010). URL http://dx.doi.org/10.1002/adma.201000376.

[12] Crispin, X. *et al.* Characterization of the interface dipole at organic/ metal interfaces. *Journal of the American Chemical Society* **124**, 8131–8141 (2002). URL http://dx.doi.org/10.1021/ja025673r.

[13] Ashcroft, N. W. & Mermin, N. D. *Solid State Physics* (Saunder College Publishing, 1976).

[14] Bischoff, F. *et al.* How surface bonding and repulsive interactions cause phase transformations: Ordering of a prototype macrocyclic compound on ag(111). *ACS Nano* **7**, 3139–3149 (2013). URL http://dx.doi.org/10.1021/nn305487c. PMID: 23521075.

[15] Basagni, A. *et al.* Stereoselective photopolymerization of tetraphenylporphyrin derivatives on Ag(110) at the sub-monolayer level. *Chemistry – A European Journal* **20**, 14296–14304 (2014). URL http://dx.doi.org/10.1002/chem.201403208.

[16] Lukasczyk, T. *et al.* Interaction of cobalt(II) tetraarylporphyrins with a Ag(111) surface studied with photoelectron spectroscopy. *The Journal of Physical Chemistry C* **111**, 3090–3098 (2007). URL http://dx.doi.org/10.1021/jp0652345.

[17] Chylarecka, D. *et al.* Indirect magnetic coupling of manganese porphyrin to a ferromagnetic cobalt substrate. *The Journal of Physical Chemistry C* **115**, 1295–1301 (2011). URL http://dx.doi.org/10.1021/jp106822s.

[18] Giovanelli, L. *et al.* Interpretation of valence band photoemission spectra at organic-metal interfaces. *Phys. Rev. B* **87**, 035413 (2013). URL http://link.aps.org/doi/10.1103/PhysRevB.87.035413.

[19] Körzdörfer, T., Kümmel, S., Marom, N. & Kronik, L. When to trust photoelectron spectra from kohn-sham eigenvalues: The case of organic semiconductors. *Phys. Rev. B* **79**, 201205(R) (2009).

[20] Puschnig, P. *et al.* Reconstruction of molecular orbital densities from photoemission data. *Science* **326**, 702–706 (2009). URL http://science.sciencemag.org/content/326/5953/702.

[21] Ziroff, J., Forster, F., Schöll, A., Puschnig, P. & Reinert, F. Hybridization of organic molecular orbitals with substrate states at interfaces: Ptcda on silver. *Physical Review Letters* **104**, 233004 (2010). URL http://link.aps.org/doi/10.1103/PhysRevLett.104.233004.

[22] Willenbockel, M. *et al.* The interplay between interface structure, energy level alignment and chemical bonding strength at organic-metal interfaces. *Phys. Chem. Chem. Phys.* **17**, 1530–1548 (2015).

[23] Puschnig, P. *et al.* Orbital tomography: Deconvoluting photoemission spectra of organic molecules. *Phys. Rev. B* **84**, 235427 (2011). URL http://link.aps.org/doi/10.1103/PhysRevB.84.235427.

[24] Dauth, M. *et al.* Perpendicular emission, dichroism, and energy dependence in angle-resolved photoemission: The importance of the final state. *Physical Review Letters* **117**, 183001 (2016). URL http://link.aps.org/doi/10.1103/PhysRevLett.117.183001.

[25] Braun, S., Salaneck, W. R. & Fahlman, M. Energy-level alignment at organic/metal and organic/organic interfaces. *Advanced Materials* **21**, 1450–1472 (2009). URL http://dx.doi.org/10.1002/adma.200802893.

[26] Ishii, H., Sugiyama, K., Ito, E. & Seki, K. Energy level alignment and interfacial electronic structures at organic/metal and organic/organic interfaces. *Advanced Materials* **11**, 605–625 (1999). URL http://dx.doi.org/10.1002/(SICI)1521-4095(199906)11:8<605::AID-ADMA605>3.0.CO;2-Q.

[27] Pope, M. & Swenberg, C. E. *Electronic Processes in Organic Crystals and Polymers* (Oxford University Press, 1999).

[28] Hwang, J., Wan, A. & Kahn, A. Energetics of metal–organic interfaces: New experiments and assessment of the field. *Materials Science and Engineering R* **64**, 1–31 (2009). URL http://www.sciencedirect.com/science/article/pii/S0927796X08001228.

[29] Ishii, H. & Seki, K. Energy level alignment at organic/metal interfaces studied by uv photoemission: breakdown of traditional assumption of a common vacuum level at the interface. *IEEE Transactions on Electron Devices* **44**, 1295–1301 (1997).

[30] Hirose, Y. *et al.* Chemistry and electronic properties of metal-organic semiconductor interfaces: Al, ti, in, sn, ag, and au on ptcda. *Phys. Rev. B* **54**, 13748–13758 (1996). URL http://link.aps.org/doi/10.1103/PhysRevB.54.13748.

[31] Vazquez, H., Dappe, Y. J., Ortega, J. & Flores, F. Energy level alignment at metal/organic semiconductor interfaces: "pillow" effect, induced density of interface states, and charge neutrality level. *The Journal of Chemical Physics* **126**, 144703 (2007). URL http://dx.doi.org/10.1063/1.2717165.

[32] Hill, I. G., Rajagopal, A., Kahn, A. & Hu, Y. Molecular level alignment at organic semiconductor-metal interfaces. *Applied Physics Letters* **73**, 662–664 (1998). URL http://dx.doi.org/10.1063/1.121940.

[33] Webb, L. E. & Fleischer, E. B. Crystal structure of porphine. *The Journal of Chemical Physics* **43**, 3100–3111 (1965). URL http://dx.doi.org/10.1063/1.1697283.

[34] Rosa, A., Ricciardi, G. & Baerends, E. J. Synergism of porphyrin-core saddling and twisting of meso-aryl substituents. *The Journal of Physical Chemistry A* **110**, 5180–5190 (2006). URL http://dx.doi.org/10.1021/jp060931i.

[35] Brand, H. & Arnold, J. Recent developments in the chemistry of early transition metal porphyrin compounds. *Coordination Chemistry Reviews* **140**, 137 – 168 (1995). URL http://www.sciencedirect.com/science/article/pii/001085459401119V.

[36] Goldoni, A. *et al.* Room Temperature Metalation of 2H-TPP Monolayer on Iron and Nickel Surfaces by Picking up Substrate Metal Atoms. *ACS Nano* **6**, 10800–10807 (2012). URL http://dx.doi.org/10.1021/nn304134q.

[37] Diller, K. *et al.* Self-metalation of 2h-tetraphenylporphyrin on cu(111): An x-ray spectroscopy study. *The Journal of Chemical Physics* **136**, 014705 (2012). URL http://dx.doi.org/10.1063/1.3674165.

[38] Wäckerlin, C. *et al.* Ammonia coordination introducing a magnetic moment in an on-surface low-spin porphyrin. *Angewandte Chemie International Edition* **52**, 4568–4571 (2013). URL http://dx.doi.org/10.1002/anie.201208028.

[39] Karim, N. & Kamarudin, S. An overview on non-platinum cathode catalysts for direct methanol fuel cell. *Applied Energy* **103**, 212 – 220 (2013). URL //www.sciencedirect.com/science/article/pii/S0306261912006721.

[40] Mochida, I., Suetsugu, K., Fujitsu, H. & Takeshita, K. Enhanced catalytic activity of cobalt tetraphenylporphyrin on titanium dioxide by evacuation at elevated temperatures for intensifying the complex-support interaction. *The Journal of Physical Chemistry* **87**, 1524–1529 (1983). URL http://dx.doi.org/10.1021/j100232a015.

[41] Ishihara, S. *et al.* Porphyrin-based sensor nanoarchitectonics in diverse physical detection modes. *Phys. Chem. Chem. Phys.* **16**, 9713–9746 (2014). URL http://dx.doi.org/10.1039/C3CP55431G.

[42] Martinez-Diaz, M. V., de la Torre, G. & Torres, T. Lighting porphyrins and phthalocyanines for molecular photovoltaics. *Chemical Communications.* **46**, 7090–7108 (2010). URL http://dx.doi.org/10.1039/C0CC02213F.

[43] Wolfle, T., Gorling, A. & Hieringer, W. Conformational flexibility of metalloporphyrins studied by density-functional calculations. *Physical Chemistry Chemical Physics* **10**, 5739–5742 (2008). URL http://dx.doi.org/10.1039/B800566B.

[44] Brede, J. *et al.* Dynamics of molecular self-ordering in tetraphenyl porphyrin monolayers on metallic substrates. *Nanotechnology* **20**, 275602 (2009). URL http://stacks.iop.org/0957-4484/20/i=27/a=275602.

[45] Buchner, F. *et al.* Substrate-mediated phase separation of two porphyrin derivatives on cu(111). *Chemistry – A European Journal* **17**, 10226–10229 (2011). URL http://dx.doi.org/10.1002/chem.201100462.

[46] Rojas, G. *et al.* Surface state engineering of molecule-molecule interactions. *Phys. Chem. Chem. Phys.* **14**, 4971–4976 (2012). URL http://dx.doi.org/10.1039/C2CP40254H.

[47] Weber-Bargioni, A. *et al.* Visualizing the frontier orbitals of a conformationally adapted metalloporphyrin. *ChemPhysChem* **9**, 89–94 (2008). URL http://dx.doi.org/10.1002/cphc.200700600.

[48] Donovan, P., Robin, A., Dyer, M. S., Persson, M. & Raval, R. Unexpected Deformations Induced by Surface Interaction and Chiral Self-Assembly of Co(II)-Tetraphenylporphyrin (Co-TPP) Adsorbed on Cu(110): A Combined STM and Periodic DFT Study. *Chemistry – A European Journal* **16**, 11641–11652 (2010). URL http://dx.doi.org/10.1002/chem.201001776.

[49] Buchner, F. *et al.* Ordering aspects and intramolecular conformation of tetraphenylporphyrins on ag(111). *Phys. Chem. Chem. Phys.* **12**, 13082–13090 (2010). URL http://dx.doi.org/10.1039/C004551A.

[50] Auwärter, W. *et al.* Site-specific electronic and geometric interface structure of co-tetraphenylporphyrin layers on ag(111). *Physical Review B* **81**, 245403 (2010). URL http://link.aps.org/doi/10.1103/PhysRevB.81.245403.

[51] Sedona, F. *et al.* Fullerene/porphyrin multicomponent nanostructures on ag(110): From supramolecular self-assembly to extended copolymers. *ACS Nano* **4**, 5147–5154 (2010). URL http://dx.doi.org/10.1021/nn101161a.

[52] Hieringer, W. *et al.* The surface trans effect: Influence of axial ligands on the surface chemical bonds of adsorbed metalloporphyrins. *Journal of the American Chemical Society* **133**, 6206–6222 (2011). URL http://dx.doi.org/10.1021/ja1093502.

[53] Scudiero, L., Hipps, K. W. & Barlow, D. E. A self-organized two-dimensional bimolecular structure. *The Journal of Physical Chemistry B* **107**, 2903–2909 (2003). URL http://dx.doi.org/10.1021/jp026875c.

[54] Scudiero, L., Barlow, D. E., Mazur, U. & Hipps, K. W. Scanning tunneling microscopy, orbital-mediated tunneling spectroscopy, and ultraviolet photoelectron spectroscopy of metal(ii) tetraphenylporphyrins deposited from vapor. *Journal of the American Chemical Society* **123**, 4073–4080 (2001). URL http://dx.doi.org/10.1021/ja0100726.

[55] Liao, M.-S. & Scheiner, S. Electronic structure and bonding in metal porphyrins, metal=fe, co, ni, cu, zn. *The Journal of Chemical Physics* **117**, 205–219 (2002).

[56] Dyer, M. *et al.* Understanding the interaction of the porphyrin macrocycle to reactive metal substrates: Structure, bonding, and adatom capture. *ACS Nano* **5**, 1831–1838 (2011).

[57] Peisert, H., Uihlein, J., Petraki, F. & Chassé, T. Charge transfer between transition metal phthalocyanines and metal substrates: The role of the transition metal. *Journal of Electron Spectroscopy and Related Phenomena* **204, Part A**, 49 – 60 (2015). URL http://www.sciencedirect.com/science/article/pii/S0368204815000171. Organic Electronics.

[58] Feyer, V. *et al.* Adsorption structure of glycyl-glycine on cu(110). *The Journal of Physical Chemistry C* **114**, 10922–10931 (2010). URL http://dx.doi.org/10.1021/jp102922g.

[59] Borghetti, P. *et al.* Adsorption geometry, conformation, and electronic structure of 2H-octaethylporphyrin on Ag(111) and Fe metalation in ultra high vacuum. *The Journal of Chemical Physics* **138** (2013). URL http://scitation.aip.org/content/aip/journal/jcp/138/14/10.1063/1.4798934.

[60] Diller, K. *et al.* Investigating the molecule-substrate interaction of prototypic tetrapyrrole compounds: Adsorption and self-metalation of porphine on cu(111). *The Journal of Chemical Physics* **138**, 154710 (2013). URL http://dx.doi.org/10.1063/1.4800771.

[61] Bai, Y. *et al.* Interfacial coordination interactions studied on cobalt octaethylporphyrin and cobalt tetraphenylporphyrin monolayers on au(111). *Phys. Chem. Chem. Phys.* **12**, 4336–4344 (2010). URL http://dx.doi.org/10.1039/B924974P.

[62] Rocha, A. *et al.* Towards molecular spintronics. *Nature Materials* **4**, 335–339 (2005). URL http://www.nature.com/nmat/journal/v4/n4/full/nmat1349.html.

[63] Lach, S. *et al.* Metal–organic hybrid interface states of a ferromagnet/organic semiconductor hybrid junction as basis for engineering spin injection in organic spintronics. *Advanced Functional Materials* **22**, 989–997 (2012). URL http://dx.doi.org/10.1002/adfm.201102297.

[64] Ballav, N., Wäckerlin, C., Siewert, D., Oppeneer, P. M. & Jung, T. A. Emergence of on-surface magnetochemistry. *The Journal of Physical Chemistry Letters* **4**, 2303–2311 (2013). URL http://dx.doi.org/10.1021/jz400984k.

[65] Wende, H. *et al.* Substrate-induced magnetic ordering and switching of iron porphyrin molecules. *Nature Materials* **6**, 516–520 (2007). URL http://www.nature.com/nmat/journal/v6/n7/full/nmat1932.html.

[66] Komeda, T. Spins of adsorbed molecules investigated by the detection of kondo resonance. *Surface Science* **630**, 343–355 (2014). URL http://www.sciencedirect.com/science/article/pii/S0039602814002040.

[67] Scudiero, L. & Hipps, K. W. Controlled manipulation of self-organized Ni(ii)-octaethylporphyrin molecules deposited from solution on HOPG with a scanning tunneling microscope. *The Journal of Physical Chemistry C* **111**, 17516–17520 (2007). URL http://dx.doi.org/10.1021/jp075175a.

[68] Bernien, M. *et al.* Fe-porphyrin monolayers on ferromagnetic substrates: Electronic structure and magnetic coupling strength. *Physical Review B* **76**, 214406 (2007). URL http://link.aps.org/doi/10.1103/PhysRevB.76.214406.

[69] Bernien, M. *et al.* Tailoring the nature of magnetic coupling of fe-porphyrin molecules to ferromagnetic substrates. *Physical Review Letters* **102**, 047202 (2009). URL http://link.aps.org/doi/10.1103/PhysRevLett.102.047202.

[70] Hermanns, C. F. *et al.* Magnetic coupling of porphyrin molecules through graphene. *Advanced Materials* **25**, 3473–3477 (2013). URL http://dx.doi.org/10.1002/adma.201205275.

[71] Gottfried, J. M. Surface chemistry of porphyrins and phthalocyanines. *Surface Science Reports* **70**, 259 – 379 (2015). URL http://www.sciencedirect.com/science/article/pii/S0167572915000114.

[72] Seufert, K. *et al.* Cis-dicarbonyl binding at cobalt and iron porphyrins with saddle-shape conformation. *Nature Chemistry* **3**, 114–119 (2011). URL http://www.nature.com/nchem/journal/v3/n2/full/nchem.956.html.

[73] Seufert, K., Auwärter, W. & Barth, J. V. Discriminative response of surface-confined metalloporphyrin molecules to carbon and nitrogen monoxide. *Journal of the American Chemical Society* **132**, 18141–18146 (2010). URL http://dx.doi.org/10.1021/ja1054884.

[74] Hüfner, S. *Photoelectron Spectroscopy* (Springer-Verlag, 2003).

[75] Eberhardt, W. & Himpsel, F. J. Dipole selection rules for optical transitions in the fcc and bcc lattices. *Phys. Rev. B* **21**, 5572–5576 (1980). URL http://link.aps.org/doi/10.1103/PhysRevB.21.5572.

[76] Patt, M. C. *Bulk ans surface sensitivity energy-filtered photoemission microscopy using synchrotron radiation for the study of resistive switching memories*. PhD dissertation, Universität Duisburg-Essen (2016). URL http://juser.fz-juelich.de/record/807741.

[77] Berglund, C. N. & Spicer, W. E. Photoemission studies of copper and silver: Theory. *Physical Review* **136**, A1030–A1044 (1964). URL http://link.aps.org/doi/10.1103/PhysRev.136.A1030.

[78] Damascelli, A. Probing the electronic structure of complex systems by arpes. *Physica Scripta* **2004**, 61 (2004). URL http://stacks.iop.org/1402-4896/2004/i=T109/a=005.

[79] Seah, M. P. & Dench, W. A. Quantitative electron spectroscopy of surfaces: A standard data base for electron inelastic mean free paths in solids. *Surface and Interface Analysis* **1**, 2–11 (1979). URL http://dx.doi.org/10.1002/sia.740010103.

[80] Pendry, J. Theory of photoemission. *Surface Science* **57**, 679 – 705 (1976). URL http://www.sciencedirect.com/science/article/pii/0039602876903551.

[81] Schattke, W. Photoemission within and beyond the one-step model. *Progress in Surface Science* **54**, 211 – 227 (1997). URL http://www.sciencedirect.com/science/article/pii/S0079681697000051.

[82] Fornasi, P. Introduction to x-ray absorption spectroscopy. In *Synchrotron Radiation*, chap. 6 (Springer-Verlag, 2015).

[83] Koningsberger, D. C. & Prins, R. *X-Ray Absorption: Principles, Applications, Techniques of EXAFS, SEXAFS and XANES* (Wiley, 1987).

[84] Hahner, G. Near edge x-ray absorption fine structure spectroscopy as a tool to probe electronic and structural properties of thin organic films and liquids. *Chem. Soc. Rev.* **35**, 1244–1255 (2006). URL http://dx.doi.org/10.1039/B509853J.

[85] Stöhr, J. *NEXAFS Spectroscopy* (Springer, 1992).

[86] Teo, B. K. *EXAFS: Basic Principles and Data Analysis* (Springer, 1986).

[87] Stöhr, J. & Outka, D. A. Determination of molecular orientations on surfaces from the angular dependence of near-edge x-ray-absorption fine-structure spectra. *Physical Review B* **36**, 7891–7905 (1987). URL http://link.aps.org/doi/10.1103/PhysRevB.36.7891.

[88] Locatelli, A. & Mentes, T. O. Chemical and magnetic imaging with x-ray photoemission electron microscopy. In *Synchrotron Radiation*, chap. 8 (Springer-Verlag, 2015).

[89] Bauer, E. Cathode lens electron microscopy: past and future. *Journal of Physics: Condensed Matter* **21**, 314001 (2009). URL http://stacks.iop.org/0953-8984/21/i=31/a=314001.

[90] Locatelli, A. & Bauer, E. Recent advances in chemical and magnetic imaging of surfaces and interfaces by xpeem. *Journal of Physics: Condensed Matter* **20** (2008). URL http://stacks.iop.org/0953-8984/20/i=9/a=093002.

[91] Günther, S., Kaulich, B., Gregoratti, L. & Kiskinova, M. Photoelectron microscopy and applications in surface and materials science. *Progress in Surface Science* **70**, 187 – 260 (2002). URL http://www.sciencedirect.com/science/article/pii/S0079681602000072.

[92] Escher, M. *et al.* Nanoesca: a novel energy filter for imaging x-ray photoemission spectroscopy. *Journal of Physics: Condensed Matter* **17**, S1329 (2005). URL http://stacks.iop.org/0953-8984/17/i=16/a=004.

[93] Bauer, E. Photoelectron Microscopy. *Journal of Physics: Condensed Matter* **13**, 11391 (2001). URL http://stacks.iop.org/0953-8984/13/i=49/a=316.

[94] Hawkes, P. W. & Spence, J. C. (eds.) *Science of Microscopy* (Springer, 2007).

[95] Bauer, E. *Surface Microscopy with Low Energy Electrons* (Springer-Verlag, 2014).

[96] Schmidt, T. *et al.* SPELEEM: combining LEEM and spectroscopic imaging. *Surface Review and Letters* **5**, 1287–1296 (1998).

[97] Bauer, E. LEEM basics. *Surface Review and Letters* **5**, 1275–1286 (1998).

[98] Ueno, N. & Kera, S. Electron spectroscopy of functional organic thin films: Deep insights into valence electronic structure in relation to charge transport property. *Progress in Surface Science* **83**, 490 – 557 (2008). URL http://www.sciencedirect.com/science/article/pii/S0079681608000567.

[99] Auwärter, W., Écija, D., Klappenberger, F. & Barth, J. Porphyrins at interfaces. *Nature Chemistry* **7**, 105–120 (2015). URL http://www.nature.com/nchem/journal/v7/n2/full/nchem.2159.html.

[100] Lüftner, D. *et al.* Imaging the wave functions of adsorbed molecules. *Proceedings of the National Academy of Sciences* **111**, 605–610 (2014). URL http://www.pnas.org/content/111/2/605.abstract.

[101] Weiß, S. *et al.* Exploring three-dimensional orbital imaging with energy-dependent photoemission tomography. *Nature Communications* **6** (2015). URL http://www.nature.com/articles/ncomms9287.

[102] Puschnig, P., Koller, G., Draxl, C. & Ramsey, M. G. The structure of molecular orbitals investigated by angle-resolved photoemission. In *Small Organic Molecules on Surfaces*, chap. 1 (Springer Berlin Heidelberg, 2013).

[103] Wiesendanger, R. & Güntherodt, H.-J. *Scanning Tunneling Microscopy I*, vol. 20 of *Surface Science* (Springer-Verlag, 1992).

[104] Chen, C. *Introduction to scanning tunneling microscopy* (Oxford university press, 1993).

[105] Bai, C. *Scanning Tunneling Microscopy and its Application*, vol. 32 of *Surface Science* (Springer, 1995).

[106] Nečas, D. & Klapetek, P. Gwyddion: an open-source software for spm data analysis. *Central European Journal of Physics* **10**, 181–188 (2012). URL http://dx.doi.org/10.2478/s11534-011-0096-2.

[107] Di Santo, G. *et al.* Conformational Adaptation and Electronic Structure of 2H-Tetraphenylporphyrin on Ag(111) during Fe Metalation. *The Journal of Physical Chemistry C* **115**, 4155–4162 (2011). URL http://dx.doi.org/10.1021/jp111151n.

[108] Newbury, D. C., Ishii, I. & Hitchcock, A. P. Inner shell electron-energy loss spectroscopy of some heterocyclic molecules. *Canadian Journal of Chemistry* **64**, 1145–1155 (1986). URL http://dx.doi.org/10.1139/v86-900.

[109] Cudia, C. C. *et al.* Electronic structure and molecular orientation of a Zn-tetra-phenyl porphyrin multilayer on Si(111). *Surface Science* **600**, 4013 – 4017 (2006). URL http://www.sciencedirect.com/science/article/pii/S0039602806004584. Berlin, Germany: 4–9 September 2005Proceedings of the 23th European Conference on Surface Science.

[110] Zamborlini, G. *et al.* Multi-orbital charge transfer at highly oriented organic/metal interfaces. *Nature Communications* (2017). Accepted for publication.

[111] Di Santo, G. *et al.* Supramolecular engineering through temperature-induced chemical modification of 2h-tetraphenylporphyrin on ag(111): Flat phenyl conformation and possible dehydrogenation reactions. *Chemistry – A European Journal* **17**, 14354–14359 (2011). URL http://dx.doi.org/10.1002/chem.201102268.

[112] Kresse, G. & Hafner, J. Ab initio molecule dynamics for liquid metals. *Phys. Rev. B* **47**, 558 (1993).

[113] Kresse, G. & Joubert, D. From ultrasoft pseudopotentials to the projector augmented-wave method. *Phys. Rev. B* **59**, 1758 (1999).

[114] Neugebauer, J. & Scheffler, M. Adsorbate-substarte and adsorbate-adsorbate interactions of Na and Ka adlayers on Al(111). *Phys. Rev. B* **46**, 16067 (1992).

[115] Perdew, J. P., Burke, K. & Ernzerhof, M. Generalized Gradient Approximation Made Simple. *Phys. Rev. Lett.* **77**, 3865 (1996).

[116] Heyd, J., Scuseria, G. E. & Ernzerhof, M. Erratum: "hybrid functionals based on a screened coulomb potential" [j. chem. phys. 118, 8207 (2003)]. *J. Chem. Phys.* **124**, 219906 (2006).

[117] Monkhorst, H. J. & Pack, J. D. Special points for Brillouin-zone integrations. *Phys. Rev. B* **13**, 5188 (1976).

[118] Blöchl, P. E. Projector augmented-wave method. *Phys. Rev. B* **50**, 17953 (1994).

[119] Tkatchenko, A. & Scheffler, M. Accurate molecular van der waals interactions from ground-state electron density and free-atom reference data. *Phys. Rev. Lett.* **102**, 073005 (2009).

[120] Ruiz, V. G., Liu, W., Zojer, E., Scheffler, M. & Tkatchenko, A. Density-functional theory with screened van der waals interactions for the modeling of hybrid inorganic-organic systems. *Phys. Rev. Lett.* **108**, 146103 (2012).

[121] Wagner, M., Puschnig, P., Berkebile, S., Netzer, F. P. & Ramsey, M. G. Alternating chirality in the monolayer H2TPP on Cu(110)-(2x1)O. *Phys. Chem. Chem. Phys.* **15**, 4691–4698 (2013).

[122] Krasnikov, S. A. *et al.* An x-ray absorption and photoemission study of the electronic structure of ni porphyrins and ni n-confused porphyrin. *Journal of Physics: Condensed Matter* **20**, 235207 (2008). URL http://stacks.iop.org/0953-8984/20/i=23/a=235207.

[123] Reichert, J. *et al.* l-Tyrosine on Ag(111): Universality of the Amino Acid 2D Zwitterionic Bonding Scheme. *ACS Nano* **4**, 1218–1226 (2010). URL http://dx.doi.org/10.1021/nn901669p. PMID: 20092357.

[124] Witte, G., Lukas, S., Bagus, P. S. & Wöll, C. Vacuum level alignment at organic/metal junctions: "Cushion' ' effect and the interface dipole. *Appl. Phys. Lett.* **87**, 263502 (2005).

[125] Romaner, L., Nabok, D., Puschnig, P., Zojer, E. & Ambrosch-Draxl, C. Theoretical study of PTCDA adsorbed on the coinage metal surfaces, Ag(111), Au(111) and Cu(111). *New J. Phys.* **11**, 053010 (2009).

[126] Winkelmann, A. *et al.* Analysis of the electronic structure of copper via two-dimensional photoelectron momentum distribution patterns. *New Journal of Physics* **14** (2012).

[127] Kümmel, S. & Kronik, L. Orbital-dependent density functionals: Theory and applications. *Rev. Mod. Phys.* **80**, 3–60 (2008).

[128] Kronik, L., Stein, T., Refaely-Abramson, S. & Baer, R. Excitation gaps of finite-sized systems from optimally tuned range-separated hybrid functionals. *J. Chem. Theory Comput.* **8**, 1515–1531 (2012).

[129] Lüftner, D. *et al.* Experimental and theoretical electronic structure of quinacridone. *Phys. Rev. B* **90**, 075204 (2014).

[130] Graus, M. *et al.* Electron-vibration coupling in molecular materials: Assignment of vibronic modes from photoelectron momentum mapping. *Phys. Rev. Lett.* **116**, 147601 (2016). URL http://link.aps.org/doi/10.1103/PhysRevLett.116.147601.

[131] Valiev, M. *et al.* Nwchem: A comprehensive and scalable open-source solution for large scale molecular simulations. *Computer Physics Communications* **181**, 1477 – 1489 (2010).

[132] Okajima, T., Yamamoto, Y., Ouchi, Y. & Seki, K. NEXAFS spectra of metallotetraphenylporphyrins with adsorbed nitrogen monoxide. *Journal of Electron Spectroscopy and Related Phenomena* **114–116**, 849 – 854 (2001). URL http://www.sciencedirect.com/science/article/pii/S0368204800002681. Proceeding of the Eight International Conference on Electronic Spectroscopy and Structure,.

[133] Fatayer, S. *et al.* Self-assembly of NiTPP on Cu(111): a transition from disordered 1D wires to 2D chiral domains. *Phys. Chem. Chem. Phys.* **17**, 18344–18352 (2015). URL http://dx.doi.org/10.1039/C5CP01288K.

[134] Marcus, P. & Hinnen, C. XPS study of the early stages of deposition of Ni, Cu and Pt on HOPG. *Surface Science* **392**, 134 – 142 (1997). URL http://www.sciencedirect.com/science/article/pii/S0039602897005372.

[135] Chen, M. *et al.* Direct Synthesis of Nickel(II) Tetraphenylporphyrin and Its Interaction with a Au(111) Surface: A Comprehensive Study. *The Journal of Physical Chemistry C* **114**, 9908–9916 (2010). URL http://dx.doi.org/10.1021/jp102031m.

[136] Gunnarsson, O. & Schönhammer, K. CO on Cu(100)-Explanation of the Three-Peak Structure in the X-Ray-Photoemission-Spectroscopy Core Spectrum. *Physical Review Letters* **41**, 1608–1612 (1978). URL https://link.aps.org/doi/10.1103/PhysRevLett.41.1608.

[137] de Groot, F. M. F., Fuggle, J. C., Thole, B. T. & Sawatzky, G. A. 2p x-ray absorption of 3d transition-metal compounds: An atomic multiplet description including the crystal field. *Physical Review B* **42**, 5459–5468 (1990). URL https://link.aps.org/doi/10.1103/PhysRevB.42.5459.

[138] Doyle, C. M. *et al.* Ni-Cu ion exchange observed for Ni(II)-porphyrins on Cu(111). *Chem. Commun.* **50**, 3447–3449 (2014). URL http://dx.doi.org/10.1039/C3CC48913B.

[139] Shen, K. *et al.* On-surface manipulation of atom substitution between cobalt phthalocyanine and the Cu(111) substrate. *RSC Adv.* **7**, 13827–13835 (2017). URL http://dx.doi.org/10.1039/C7RA00636E.

[140] Isaacson, M. Limits of detection sensitivity due to electron beam radiation damage. *Ultramicroscopy* **28**, 320 – 323 (1989). URL http://www.sciencedirect.com/science/article/pii/0304399189903173.

[141] Uyeda, N., Kobayashi, T., Suito, E., Harada, Y. & Watanabe, M. Molecular image resolution in electron microscopy. *Journal of Applied Physics* **43**, 5181–5189 (1972). URL http://dx.doi.org/10.1063/1.1661094.

[142] Vollnhals, F., Wintrich, P., Walz, M.-M., Steinrück, H.-P. & Marbach, H. Electron beam induced surface activation of ultrathin porphyrin layers on ag(111). *Langmuir* **29**, 12290–12297 (2013). URL http://dx.doi.org/10.1021/la4028095. PMID: 24004187.

[143] Thorman, R. M., Kumar T. P., R., Fairbrother, D. H. & Ingólfsson, O. The role of low-energy electrons in focused electron beam induced deposition: four case studies of representative precursors. *Beilstein Journal of Nanotechnology* **6**, 1904–1926 (2015).

[144] Isaacson, M., Johnson, D. & Crewe, A. V. Electron beam excitation and damage of biological molecules; its implications for specimen damage in electron microscopy. *Radiation Research* **55**, 205–224 (1973). URL http://www.jstor.org/stable/3573678.

[145] Janow, R. & Tzoar, N. Kinetic theory description of electron stimulated desorption. *Surface Science* **69**, 253 – 272 (1977). URL http://www.sciencedirect.com/science/article/pii/0039602877901728.

[146] Clark, W. R. K., Chapman, J. N. & Ferrier, R. P. The structure of α'-copper phthalocyanine and its susceptibility to radiation damage. *Nature* **277**, 368–370 (1979).

[147] Clark, W., Chapman, J., MacLeod, A. & Ferrier, R. Radiation damage mechanisms in copper phthalocyanine and its chlorinated derivatives. *Ultramicroscopy* **5**, 195 – 208 (1980). URL http://www.sciencedirect.com/science/article/pii/0304399180900248.

[148] Kurata, H., Isoda, S. & Kobayashi, T. Eels study of radiation damage in chlorinated cu-phthalocyanine and poly geo-phthalocyanine. *Ultramicroscopy* **41**, 33 – 40 (1992). URL http://www.sciencedirect.com/science/article/pii/030439919290092X.

[149] Massey, S. & Sanche, L. Low-energy electron mechanisms inducing damage in organic molecules and polymers. In *Radiation Synthesis of Materials and Compounds*, chap. 16 (CRC Press, 2013). URL http://dx.doi.org/10.1201/b14531-19.

[150] Cai, Z., Dextraze, M.-E., Cloutier, P., Hunting, D. & Sanche, L. Induction of strand breaks by low-energy electrons (8–68ev) in a self-assembled monolayer of oligonucleotides: Effective cross sections and attenuation lengths. *The Journal of Chemical Physics* **124**, 024705 (2006). URL http://dx.doi.org/10.1063/1.2141505.

[151] Whitesides, G. M. & Grzybowski, B. Self-assembly at all scales. *Science* **295**, 2418–2421 (2002). URL http://science.sciencemag.org/content/295/5564/2418.

[152] Theobald, J., Oxtoby, N., Phillips, M., Champness, N. & Beton, P. Controlling molecular deposition and layer structure with supramolecular surface assemblies. *Nature* **424**, 1029–1031 (2003). URL http://www.nature.com/nature/journal/v424/n6952/full/nature01915.html.

[153] Smykalla, L. *et al.* Interplay of hydrogen bonding and molecule–substrate interaction in self-assembled adlayer structures of a hydroxyphenyl-substituted porphyrin. *Surface Science* **628**, 132 – 140 (2014). URL http://www.sciencedirect.com/science/article/pii/S0039602814001587.

[154] Kong, J., Chapline, M. G. & Dai, H. Functionalized carbon nanotubes for molecular hydrogen sensors. *Advanced Materials* **13**, 1384–1386 (2001). URL http://dx.doi.org/10.1002/1521-4095(200109)13:18<1384::AID-ADMA1384>3.0.CO;2-8.

[155] Jiang, X., Gou, F., Chen, F. & Jing, H. Cycloaddition of epoxides and CO_2 catalyzed by bisimidazole-functionalized porphyrin cobalt(III) complexes. *Green Chem.* **18**, 3567–3576 (2016). URL http://dx.doi.org/10.1039/C6GC00370B.

[156] Sedona, F. *et al.* Tuning the catalytic activity of Ag(110)-supported fe phthalocyanine in the oxygen reduction reaction. *Nature Materials* **11**, 970–977 (2012). URL http://www.nature.com/nmat/journal/v11/n11/full/nmat3453.html.

[157] Buchner, F. *et al.* NO-induced reorganization of porphyrin arrays. *ACS Nano* **3**, 1789–1794 (2009). URL http://dx.doi.org/10.1021/nn900399u.

[158] Kim, H. *et al.* Visualizing tilted binding and precession of diatomic NO adsorbed to Co-porphyrin on Au(111) using scanning tunneling microscopy. *Chemical Science* **5**, 2224–2229 (2014). URL http://dx.doi.org/10.1039/C3SC52004H.

[159] Schmidt, N., Fink, R. & Hieringer, W. Assignment of near-edge x-ray absorption fine structure spectra of metalloporphyrins by means of time-dependent density-functional calculations. *The Journal of Chemical Physics* **133**, 054703 (2010). URL http://dx.doi.org/10.1063/1.3435349.

[160] Saito, N. & Suzuki, I. H. Anisotropic dissociation of NO in K-shell excited states. *Physical Review A* **43**, 3662–3667 (1991). URL https://link.aps.org/doi/10.1103/PhysRevA.43.3662.

[161] Stöhr, J., Baberschke, K., Jaeger, R., Treichler, R. & Brennan, S. Orientation of Chemisorbed Molecules from Surface-Absorption Fine-Structure Measurements: CO and NO on Ni(100). *Physical Review Letters* **47**, 381–384 (1981). URL https://link.aps.org/doi/10.1103/PhysRevLett.47.381.

[162] van der Laan, G., Zaanen, J., Sawatzky, G. A., Karnatak, R. & Esteva, J.-M. Comparison of x-ray absorption with x-ray photoemission of nickel dihalides and nio. *Physical Review B* **33**, 4253–4263 (1986). URL https://link.aps.org/doi/10.1103/PhysRevB.33.4253.

[163] Stöhr, J. & Jaeger, R. Absorption-edge resonances, core-hole screening, and orientation of chemisorbed molecules: CO, NO, and N_2 on Ni(100). *Physical Review B* **26**, 4111–4131 (1982). URL https://link.aps.org/doi/10.1103/PhysRevB.26.4111.

[164] Chen, B. *et al.* XPS and TPD study of NO interaction with Cu(111): Role of different oxygen species. *Chinese Journal of Catalysis* **34**, 964 – 972 (2013). URL http://www.sciencedirect.com/science/article/pii/S1872206712605853.

[165] Matloob, M. H. & Roberts, M. W. Electron spectroscopic study of nitrogen species adsorbed on copper. *J. Chem. Soc., Faraday Trans. 1* **73**, 1393–1405 (1977). URL http://dx.doi.org/10.1039/F19777301393.

[166] Johnson, D. W., Matloob, M. H. & Roberts, M. W. Study of the interaction of nitric oxide with Cu(100) and Cu(111) surfaces using low energy electron diffraction and electron spectroscopy. *J. Chem. Soc., Faraday Trans. 1* **75**, 2143–2159 (1979). URL http://dx.doi.org/10.1039/F19797502143.

[167] Tusche, C. *et al.* Spin resolved photoelectron microscopy using a two-dimensional spin-polarizing electron mirror. *Applied Physics Letters* **99**, 032505 (2011). URL http://dx.doi.org/10.1063/1.3611648.

[168] Tusche, C. *et al.* Quantitative spin polarization analysis in photoelectron emission microscopy with an imaging spin filter. *Ultramicroscopy* **130**, 70–76 (2013). URL http://www.sciencedirect.com/science/article/pii/S0304399113000661.

[169] Tusche, C., Krasyuk, A. & Kirschner, J. Spin resolved bandstructure imaging with a high resolution momentum microscope. *Ultramicroscopy* **159, Part 3**, 520 – 529 (2015). URL http://www.sciencedirect.com/science/article/pii/S0304399115000698.

[170] Kirschner, J. & Feder, R. Spin Polarization in Double Diffraction of Low-Energy Electrons from W(001): Experiment and Theory. *Physical Review Letters* **42**, 1008–1011 (1979). URL https://link.aps.org/doi/10.1103/PhysRevLett.42.1008.

[171] Feyer, V. *et al.* The geometric and electronic structure of TCNQ and TCNQ+Mn on Ag(001) and Cu(001) surfaces. *Journal of Electron Spectroscopy and Related Phenomena* **204, Part A**, 125 – 131 (2015). URL http://www.sciencedirect.com/science/article/pii/S0368204815000420. Organic Electronics.

Band / Volume 41
Integration of Redox-Based Resistive Switching Memory Devices
F. Lentz (2014), i, 166 pp
ISBN: 978-3-95806-019-7

Band / Volume 42
Ladungstransportuntersuchungen an nanofunktionalen Bauelementen mit Diodencharakteristik basierend auf funktionalisierten Nanopartikeln
N. Babajani (2015), iv, 138, XLVII
ISBN: 978-3-95806-026-5

Band / Volume 43
Transport and Noise Properties of Nanostructure Transistors for Biosensor Applications
J. Li (2015), vii, 175 pp
ISBN: 978-3-95806-034-0

Band / Volume 44
Quantitative scanning tunneling spectroscopy of non-polar III-V compound semiconductor surfaces
M. Schnedler (2015), 122 pp
ISBN: 978-3-95806-075-3

Band / Volume 45
Model-based Algorithm Development with Focus on Biosignal Processing
Y. Yao (2015), x, 169 pp
ISBN: 978-3-95806-080-7

Band / Volume 46
Growth and characterization of crystalline rare-earth based thin oxide fims for the application as gate dielectric in nanotechnology
A. B. Schäfer (2015), xiii, 157 pp
ISBN: 978-3-95806-111-8

Band / Volume 47
TEM/STEM Investigations of Phase Change Materials for Non-volatile Memory Applications
M. Bornhöfft (2017), viii, 135 pp
ISBN: 978-3-95806-221-4

Band / Volume 48
Investigation of ternary nitride semiconductor alloys by scanning tunneling microscopy
V. Portz (2017), 140 pp
ISBN: 978-3-95806-232-0

Band / Volume 49
Redox processes and ionic transport in resistive switching binary metal oxides
K. Skaja (2017), VII, 203 pp
ISBN: 978-3-95806-236-8

Band / Volume 50
Investigation of switching mechanism in Ta_2O_5 -based ReRAM devices
K. Wonjoo (2017), iii, 138 pp
ISBN: 978-3-95806-261-0

Band / Volume 51
Development of ReRAM-based Devices for Logic- and Computation-in-Memory Applications
T. Breuer (2017), x, 179 pp
ISBN: 978-3-95806-270-2

Band / Volume 52
Resistive switching memory devices from atomic layer deposited binary and ternary oxide thin films
N. Aslam (2017), X, 172 pp
ISBN: 978-3-95806-274-0

Band / Volume 53
Operando X-ray photoemission electron microscopy (XPEEM) investigations of resistive switching metal-insulator-metal devices
C. J. Schmitz (2017), IX, 153 pp
ISBN: 978-3-95806-283-2

Band / Volume 54
Optimization of powder and ceramic processing, electrical characterization and defect chemistry in the system $Yb_xCa_{1-x}MnO_3$
M. Rahmani (2018), XIV, 164 pp
ISBN: 978-3-95806-323-5

Band / Volume 55
Organic-Metal Hybrid Interfaces at the Mesoscopic Scale
G. Zamborlini (2018), xi, 133 pp
ISBN: 978-3-95806-328-0

Information
Band / Volume 55
ISBN 978-3-95806-328-0

Mitglied der Helmholtz-Gemeinschaft

JÜLICH
Forschungszentrum